Numerically exact quantum dynamics of low-dimensional lattice systems

Benedikt Kloss

Submitted in partial fulfillment of the

requirements for the degree of

Doctor of Philosophy

under the Executive Committee

of the Graduate School of Arts and Sciences

COLUMBIA UNIVERSITY

2021

This page is intentionally left blank.

ABSTRACT

Numerically exact quantum dynamics of low-dimensional lattice systems

Benedikt Kloss

In this thesis I present contributions to the development, analysis and application of tensor network state methods for numerically exact quantum dynamics in one and two-dimensional lattice systems. The setting of numerically exact quantum dynamics is introduced in Chapter 2. This includes a discussion of exact diagonalization approaches and massively parallel implementations thereof as well as a brief introduction of tensor network states. In Chapter 3, I perform a detailed analysis of the performance of n-ary tree tensor network states for simulating the dynamics of two-dimensional lattices. This constitutes the first application of this class of tensor network to dynamics in two spatial dimensions, a long-standing challenge, and the method is found to perform on par with existing state-of-the art approaches. Chapter 4 showcases the efficacy of a novel tensor network format I developed, tailored to electron-phonon coupled problems in their single-electron sector, through an application to the Holstein model. The applicability of the approach to a broad range of parameters of the model allows to reveal the strong influence of the spread of the electron distribution on the initial state of the phonons at the site where the electron is introduced, for which a simple physical picture is offered. I depart from method development in Chapter 5 and analyse the prospects of using tensor network states evolved using the time-dependent variational principle as an approximate approach to determine asymptotic transport properties with a finite, moderate computational effort. The method is shown to not yield the correct asymptotics in a clean, non-integrable system and can thus not be expected to work

in generic systems, outside of finely tuned parameter regimes of certain models. Chapters 6 and 7 are concerned with studies of spin transport in long-range interacting systems using tensor network state methods. For the clean case, discussed in Chapter 6, we find that for sufficiently short-ranged interactions, the spreading of the bulk of the excitation is diffusive and thus dominated by the local part of the interaction, while the tail of the excitation decays with a powerlaw that is twice as large as the powerlaw of the interaction. Similarly, in the disordered case, analysed in Chapter 7, we find subdiffusive transport of spin and sub-linear growth of entanglement entropy. This behaviour is in agreement with the behaviour of systems with local interactions at intermediate disorder strength, but provides evidence against the phenomelogical Griffith picture of rare, strongly disordered insulating regions. We generalize the latter to long-ranged interactions and show that it predicts to diffusion, in contrast to the local case where it results in subdiffusive behaviour.

This page is intentionally left blank.

Contents

List of figures

List of tables

Acknowledgements

Thanks go to my PhD advisor David Reichman for being a great mentor and teacher, as well as my two main collaborators, Roel Tempelaar and Yevgeny Bar Lev. They all taught me a lot about physics, numerics, academia and research in general.

Thanks go to the current and former members of the Reichman group for the good atmosphere in the lab. It has been a pleasure to share the office with you. In particular, I'd like to thank Sambuddha Sanyal, John Sous and Lachlan Lindoy for our collaborations and enriching discussions.

Thanks go to my friends in New York and in Europe, and especially to Gary Howarth and Avalon Dismukes. I am grateful to have found such good friends in the Chemistry department, and the last 5 years at Columbia would have been a very different experience without them.

Thanks go to my partner, Emily Bartsch, for her love and support.

Thanks go to my parents and my sister for their love and support.

This page is intentionally left blank.

Chapter 1

Introduction

1.1 Motivation

Gaining insight into the non-equilibrium dynamics of quantum system is important for a variety of reasons. Many processes in nature or technology are inherently off-equilibrium and quantum, including light harvesting in photosynthetic complexes, solar energy conversion in photovoltaic cells and heat or electron conduction through molecular junctions [1–3]. Furthermore, driving a system out of equilibrium may allow to induce exotic physical behaviour and phases of matter which are difficult to realize in equilibrium[4]. Understanding the approach to equilibrium, or lack thereof, of an initially out-of-equilibrium quantum system is another question of both significant fundamental and technological relevance [5–7].

While perturbation theory and analytical approaches are successful in describing the essential physics of many interesting systems, certain parameter regimes and classes of models defy such approximate methods and require a numerically exact solution. Existing exact quantum dynamical methods suffer from severe limitations of the attainable system sizes, as

is the case for exact diagonalization techniques, or timescales, for example methods based on tensor network states. This is due to an exponential scaling of the computational effort with these parameters. Numerically exact approaches nonetheless offer crucial insights, and give access to time and lengthscales comparable to many current cold-atom simulator experiments [8]. Thus, in the absence of exact, non-exponentially scaling approaches, it is crucial to improve the scalability and efficiency of existing numerical techniques.

1.2 Thesis outline

The focus of this thesis lies in the development, analysis and application of tensor network state methods for quantum dynamics in low-dimensional lattice systems. We begin with an introduction to commonly used exact quantum dynamical methods in Chapter 2, discussing exact diagonalization and direct methods in the exact Hilbert space as well as tensor network states.

Chapter 3 assesses the performance of tree tensor network states, a specific format of tensor network states, for computing the dynamics of two-dimensional lattice systems, a longstanding challenge. Models with coupling of electronic degrees of freedom to lattice vibrations constitute another challenge due to the large local Hilbert space dimension, and we showcase a promising, novel tensor network state ansatz for such models in Chapter 4. Given the exponential scaling of tensor network state approaches with time, it is pertinent to ask whether extraction of asymptotic behaviour may be possible when employing tensor network states as an approximate method, weakening the requirement of numerical exactness. We address this question in Chapter 5 in the context of spin transport.

The last two chapters apply tensor network state dynamical methods to systems with

long-range interactions in one dimension, which require lengthscales beyond the reach of exact diagonalization techniques. Despite the limited accessible timescales, these simulations allow us to draw conclusions regarding the nature of transport in both clean, see Chapter 6, and weakly disordered, see Chapter 7, spin chains with long-range interactions.

Chapter 2

Numerically exact quantum dynamical methods

2.1 Exact diagonalization

The dynamics of a closed quantum system is described by the time-dependent Schroedinger equation

$$i\partial_t \Psi = \hat{H}\Psi = \sum_i E_i \psi_i. \tag{2.1}$$

Given the spectrum of the Hamiltonian, E_i and its eigenbasis $\{\psi_i\}$, it is thus straightforward to compute the time-evolved state for any time. For a generic system with a finite-dimensional Hilbert space, eigenvalues and eigenvectors can be obtained via the eigendecomposition of the Hamiltonian matrix. $\mathbf{H} = \mathbf{VEV}^\dagger$, where $\mathbf{E}$ is a diagonal matrix of the eigenvalues E_i and the i-th row vector of $\mathbf{V}$ is the i-th eigenvector. The eigendecomposition, or *exact diagonalization*, is a well-established matrix decomposition for which robust and performant numerical implementations exist [9]. However, the computational cost of this

decomposition scales cubically with the size of the matrix. Furthermore, the eigenbasis $\mathbf{V}$ is generally a dense matrix, requiring the storage of a number of elements that grows as the square of the matrix dimension. For a lattice system with a local d-dimensional Hilbert space and N sites, the total Hilbert space dimension is d^N, leading to an overall exponential complexity of exact diagonalization with the number of lattice sites. The maximum dimension of matrices that can routinely be diagonalized on a modern workstation computer or moderate compute cluster is ~ 100000, which translates to about 16 sites for a spin-1/2 system without making use of any symmetries of the Hamiltonian.

2.2 Direct methods in the exact Hilbert space

Besides the scaling of the computational effort and memory requirements, exact diagonalization suffers from a lack of scalability on current supercomputing resources. The latter are large networks of independent compute nodes, which introduce exchange of data, or *communication*, between nodes as an additional resource and potential bottleneck. Known algorithms for exact diagonalization require a lot of communication, and are thus not capable of fully making use of existing resources. However, in order to compute dynamics, it is not necessary to know the full spectrum and all eigenvectors of the system. Instead, we can use standard solvers for linear differential equations to integrate the time-dependent Schroedinger equation which require as input only the wavefunction and the map between wavefunction and its time-derivative. The time-derivative of the wavefunction can be computed by evaluating the action of the Hamiltonian on the wavefunction.

If we consider the Hamiltonian as a dense matrix, the resulting matrix-vector multiplication scales quadratically with the matrix dimension, but otherwise it shares the same

limitations as computing the full eigendecomposition. Fortunately, the vast majority of physical systems have a sparse Hamiltonian in a basis, which is convenient to construct and physically motivated. Sparse matrix-vector multiplication can scale as low as linearly with the matrix dimension in terms of computational effort and storage requirements for the Hamiltonian. Parallelizability is strongly dependent on the structure of the Hamiltonian, but it can generally be expected to behave similarly to a dense matrix-vector multiply in that respect, with a greatly reduced prefactor due to the larger number of zero matrix elements. Since most Hamiltonians can be written as a sum over products of operators with local support, an explicit, sparse or dense, matrix representation of the Hamiltonian can be circumvented alltogether. This allows for efficient, massively parallel evaluation of their action on the wavefunction with linear scaling in computational effort and storage, enabling the simulation of dynamic of systems more than twice as large as with full exact diagonalization, see for example Ref. 10 for a current state-of-the art calculation. For many systems, an equally performant alternative is to approximate the exact propagator for a short timestep by a Trotter decomposition of the matrix exponential, for example to first order $e^{-iH\Delta t} = e^{-iH_0\Delta t}e^{-iH_1\Delta t} + \mathcal{O}\left(\Delta t^2\right)$. Both $e^{-iH_0\Delta t}$ and $e^{-iH_1\Delta t}$ need to be chosen such that they can be evaluated efficiently, for example as products of operators with non-overlapping local support.

2.3 Tensor network state approaches

The exponential scaling of the size of Hilbert space imposes a limitation to the size of systems for which we can store the wavefunction within classical computing paradigms. On the other hand, it is possible to construct an ansatz for the wavefunction with a limited number of

parameters. Product states, for example, can be represented using dN coefficients. In order for a family of ansaetze to be successful in the numerically exact study of generic systems, it should satisfy a few properties. First, it should allow to describe states of interest with arbitrary accuracy using resources that scale subexponentially in the system size. Furthermore, the ansatz should offer a way to systematically improve the accuracy of the approximation by increasing the number of parameters. And finally, there need to be efficient algorithms available to, in our case, solve the time-dependent Schroedinger equation within the manifold of states expressible by the ansatz and to compute observables. Within the last two to three decades, *tensor network states* (TNS) have become a powerful and widely used class of wavefunction representations, fulfilling these requirements at least partially. They express the wavefunction as a network of low order tensors and their computational complexity is closely connected to the entanglement of the state. In the following, a brief introduction to tensor network states will be given, followed by a discussion of their application to lattice systems.

2.3.1 Tensor network states - concepts

The tensor product structure of the many-body Hilbert space of quantum lattice systems allows us to understand the wavefunction coefficients as a high-dimensional tensor. For a system with N sites and local Hilbert space dimension d, the d^N coefficients are arranged into a tensor of order n, where each mode has dimension d. Tensors here are understood simply as multi-dimensional arrays, with scalars, vectors and matrices being tensors of order 0, 1 and 2 respectively. Operations like matrix-matrix or matrix-vector multiplication are examples of tensor contractions, i.e. as takings sums over slices of tensors sharing a common index. Algebraically, in a matrix-matrix multiplication for instance, the left matrices' column indices
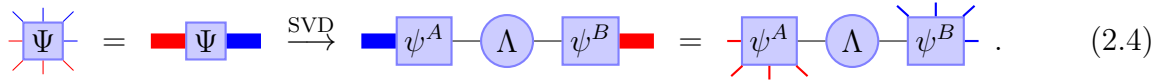
are shared with the right matrices' row-indices $\sum_j A_{ij} B_{jk} = C_{ik}$. It is helpful to introduce a diagrammatic representation of tensors and tensor contractions, where a shape represents a tensor and its modes are indicated by *leg*s. A tensor of order n has n legs, and if one or more legs of two tensors join this indicates a contraction along the participating modes, for example

$$T_{ijkl} = \quad k-\boxed{T}-l \; , \qquad i-\boxed{A}-\!\!\!\underset{j}{}\!\!\!-\boxed{B}-l = i-\boxed{C}-i \; . \tag{2.2}$$

A network of tensors is a collection of individual tensors, each of which shares one or more legs with another tensor. Consider for example the Schmidt decomposition of a state in the many-body Hilbert space given a bipartition of the lattice into partitions A and B, algebraically:

$$\Psi_{\sigma_1, \sigma_2, \ldots, \sigma_{N-1}\sigma_N} = \sum_{i=1}^r \phi^A_{(\sigma_{j\,j\in A}),i} \lambda_i \phi^B_{i,(\sigma_{j\,j\in B})} = \mathrm{SVD}(\Psi_{\sigma_{j\,j\in A}, \sigma_{j\,j\in B}}), \tag{2.3}$$

or diagramatically,

$$\tag{2.4}$$

Indices which are grouped together into a multi-index for the purpose of e.g. reshaping a tensor into matrix, are indicated by $(\ldots)$ in the index and thick legs in diagrams. Usually, the Schmidt decomposition is thought of in terms of generating orthonormal Schmidt vectors, and Schmidt coefficients, λ_i. It is synonymous with the singular value decomposition (SVD) of the coefficient-tensor reshaped into a matrix, with the row (respectively column) indices corresponding to a multi-index of the indices for sites in partition A (respectively B). In the

language of tensor networks, the SVD has introduced an auxiliary, non-physical, mode and decomposed the order N wavefunction tensor into two tensors of smaller order. They share the newly introduced, auxiliary index, which is also refered to as *bond*. The SVD can be applied repeatedly to the resulting tensors to reduce their order further, treating auxiliary indices in the same manner as physical indices. For concreteness, take a subdivision of partition A into two parts, A_1 and A_2, and compute the singular value decomposition of $\phi^A_{\sigma_{jj\in A},i}$ along the bipartition:

$$\phi^A_{\sigma_{jj\in A},i} = \phi^A_{\sigma_{jj\in A_1},\sigma_{jj\in A_2},i} = \phi^A_{\sigma_{jj\in A_1},(\sigma_{jj\in A_2},i)} = \sum_{k=1}^{r} \tilde{\phi}^{A_1}_{(\sigma_{jj\in A^1}),k} \tilde{\lambda}_k \tilde{\phi}^{A_2}_{k,(\sigma_{jj\in B},i)}$$

$$\boxed{\phi^A} - \bigcirc\Lambda - \boxed{\phi^B} \xrightarrow{\text{SVD}} \boxed{\psi^{A_1}} - \bigcirc\tilde{\Lambda} - \boxed{\psi^{A_2}} - \bigcirc\Lambda - \boxed{\psi^B} . \qquad (2.5)$$

It is straightforward to check that the singular values $\tilde{\lambda}_k$ obtained from this decomposition are identical to those obtained from the SVD of the full wavefunction given partitions A_1 and $A_2 \bigcup B$. Thus, the singular value decomposition, along other matrix decompositions, is useful to decompose tensors into networks of smaller order tensors.

2.3.2 Tensor network states and entanglement entropy

Writing a large order tensor in terms of networks of smaller order tensors does not necessarily give a reduction in the parameters necessary to represent the wavefunction. From the Schmidt decomposition, it is clear that a lossless compression is only achieved if the number of non-vanishing Schmidt coefficients r is significantly smaller than the Hilbert space dimension of the smaller of the two bipartitions. Keeping only the largest $\chi \leq r$ singular values in

the decomposition results in an error of $|\Psi - \Psi_\chi| = \sqrt{\sum_{i=q+1}^{r} \lambda_i^2}$. The number of singular values retained at each decomposition, i.e. the dimension of the shared indices of the tensor network is commonly refered to as *bond dimension*. If the bond dimension of a tensor network scales subexponentially with the system size, so does its storage requirements, and for loopless tensor network also the effort to manipulate the tensor network state. As long as an arbitrarily good approximation to the exact wavefunction can be obtained with a bond dimension that scales slower than exponential in the system size, we may say that the tensor network state offers an efficient representation of the wavefunction.

In order to gain insight into what kind of states are efficiently encoded as tensor network states, the von Neumann or entanglement entropy is a very useful quantity,

$$S^A = -tr\left(\rho^A ln\rho^A\right) = -\sum_i \lambda_i^2 ln\lambda_i^2 = S^B. \tag{2.6}$$

Here, A and B a bipartition of the lattice, and we denote the half-system entanglement entropy as S, where the bipartition corresponds to dividing the system into two equally sized halves, such that the entanglement entropy is minimized. For square lattices this is usually a cut along a straight line. A state is said to obey an area-law of entanglement entropy if S grows at most as fast as the size of the boundary of the bipartition. An important example of area-law states are ground states of one and two-dimensional gapped systems [11, 12]. States sampled randomly from the Haar-measure, on the other hand, are maximally entangled with probability approaching 1. Their entanglement entropy grows with the volume of the partition and one speaks of a volume-law state.

2.3.3 Tensor network states for one and two-dimensional lattices

In one spatial dimension, an area-law translates to a constant entanglement entropy with system size, which in turn implies that a constant bond dimension is sufficient to approximate the state with a tensor network with arbitrary precision [11]. For this reason, ground states of gapped one-dimensional systems can be represented most efficiently by matrix product states (MPS)[13], here an example for 5 sites

$$\boxed{A\,(1)} \!-\!\!-\!\! \boxed{A\,(2)} \!-\!\!-\!\! \boxed{A\,(3)} \!-\!\!-\!\! \boxed{A\,(4)} \!-\!\!-\!\! \boxed{A\,(5)} \qquad (2.7)$$
$$\quad\sigma_1 \qquad\quad \sigma_2 \qquad\quad \sigma_3 \qquad\quad \sigma_4 \qquad\quad \sigma_5$$

or more generally algebraically,

$$|\Psi[A]\rangle = \sum_{\{\sigma_n\}=1}^{d} A^{\sigma_1}(1) A^{\sigma_2}(2) \dots A^{\sigma_N}(L) \, |\sigma_1 \sigma_2 \dots \sigma_L\rangle . \qquad (2.8)$$

$A^{\sigma_i}(i)$ denotes matrix of dimension $\min\left(x, 2^i, 2^{N-i}\right) \times \min\left(x, 2^{i+1}, 2^{N-i-1}\right)$, and σ_i labels the state for the physical degree of freedom at site i. The coefficient for a many-body basis state $|\sigma_1 \sigma_2 \dots \sigma_L\rangle$ is thus encoded in a product of matrices, which explains the tensor network's name. A variety of algorithms based on MPS have been developed in the last decades, beginning with the density matrix renormalization group (DMRG) [14], an algorithm to variatonally determine the ground state of quantum system using MPS that pioneered the use of tensor networks in condensed matter physics.

In two spatial dimensions, the area-law implies a linearly growing entanglement entropy with the linear length of the lattice, which rules out an efficient representation by tensor networks without loops. However, a tensor network that mimics the lattice connectivity in two-dimensions, similar to MPS in one spatial dimension, was developped: Projector

Entangled Pair States (PEPS) [15]

(2.9)
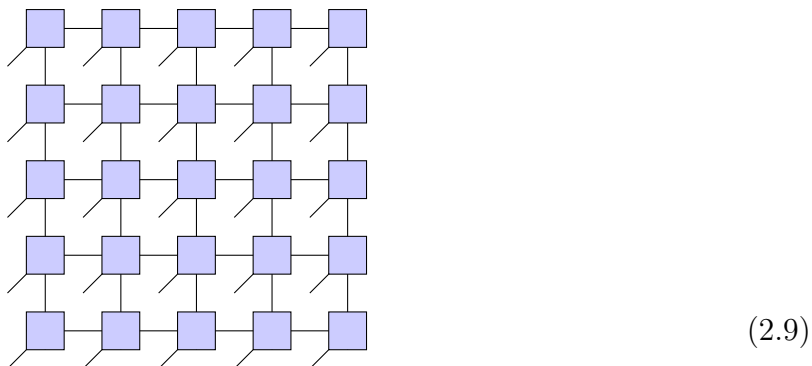
Due to the linear number of bonds connecting two halves of the system, PEPS can accomodate the growing entanglement entropy of ground states in two dimensions [16]. However, the presence of loops in the tensor network make its manipulation cumbersome and inefficient, although significant progress has been achieved in recent years [17, 18].

With non-equilibrium dynamics being the subject of this thesis, it is natural to ask whether time-evolved quantum states can be efficiently described by tensor networks. Again, an answer to this question is provided via the entanglement entropy: A generic system evolving from a weakly entangled non-equilibrium state shows a linear growth of entanglement entropy with time until saturation to a volume-law state [19]. This implies an exponential growth in the bond dimension of a loop-free tensor network, regardless of spatial dimensionality of the lattice, and thus an exponential computational effort with time. Algorithms to compute time-evolution of a quantum state with tensor networks include the Time Evolving Block decimation (TEBD) [20] and the Time-Dependent Variational Principle (TDVP) [21, 22], among others. In this thesis, both the results obtained and algorithmic contributions made, are based on the TDVP, primarily due to the ease with which non-local interactions are handled.

Chapter 3

Studying dynamics in two-dimensional quantum lattices using tree tensor network states

3.1   Introduction

The exact simulation of the non-equilibrium dynamics of interacting quantum lattice systems is generally an unsolved challenge, due to the exponential growth of the Hilbert space with the size of the system. Tensor network state (TNS) methods allow for a significant extension of accessible length scales by trading in the exponential cost in system size for an exponential cost in time. This becomes possible due to a reduction of the exact Hilbert space in terms of a structured product of low-order tensors, referred to as a tensor network. The set of the states expressible by a given tensor network spans only a small region in

Figure 3.1: Illustration of binary TTNS structure for a 4x4 lattice. The physical degrees of freedom are on the topmost layer and the top node is in the bottom-layer of the figure.

the full Hilbert space, but the coverage can be improved systematically by increasing the number of variational parameters, i.e. the bond dimension. For partitions of the lattice that lead to simply-linked tensor network parts, the logarithm of the bond-dimension gives an upper bound to the entanglement entropy. Since the entanglement of a generic system after a global quench grows linearly with time [19, 24, 25], the accessible timescales are limited. In one-dimensional systems, these timescales are often comparable to those attainable in experimental realizations [26], however going to higher spatial dimensions becomes extremely challenging due to a number of reasons.

While in one-dimensional systems, matrix product states (MPS) are known to efficiently represent area-law entangled states (which includes ground-states of gapped one-dimensional systems), this does not hold in two spatial dimensions [11, 13, 14]. The generalization of MPS to two-dimensional lattices is called Projector-Entangled Pair States (PEPS) [15], which provides an efficient representation of two-dimensional area-law entangled states [16], but PEPS are challenging to manipulate numerically [17] (see also Ref. [18] for a recent review). Approximations that are hard to control are typically used in PEPS algorithms in order to tame

the computational effort. Even with such approximations, the computational scaling is usually unfavorably steep. Nonetheless, PEPS-derived methods are state-of-the art numerical techniques for computing ground-states of two-dimensional systems [27]. Extensions of PEPS methods to the time-domain have been recently developed, however the accessible timescales are extremely limited [28–31]. An alternative approach is to use tensor network structures, which are more numerically tractable. One way to achieve this is to map the two-dimensional lattice into a one-dimensional chain and apply MPS methods, which are adjusted to handle the long-ranged interactions that arise from the mapping [32–37]. Ref. [35], for example, introduced an algorithm which expresses the propagator as a matrix product operator (MPO) acting on the states encoded as MPS. The application of this approach to two-dimensional lattices shares the very limited timescale of the more recent approaches based on PEPS, since the advantages in the computational scaling of simpler tensor networks are balancing out the disadvantages in non-optimal representation of entanglement by the tensor network structure for the problem at hand. A novel development is the use of artificial neural networks (ANN) to encode the wavefunction and its time-evolution [38]. They have been shown to perform competitively with state-of-the art TNS techniques in recent applications to two-dimensional systems [39, 40]. However, much remains to be learned about the possibilities and limitations of such methods.

It is important to explore computationally tractable tensor network structures other than MPS, since they may enable progress in the computation of the exact dynamics of interacting two-dimensional systems. For this purpose, in this work we propose to employ Tree Tensor Network States (TTNS), which encompass all loop-free tensor network states. While similarly to MPS, hierarchical, tree-like TTNS can only efficiently encode states with area-law entanglement in one dimensional systems they offer a more robust description of
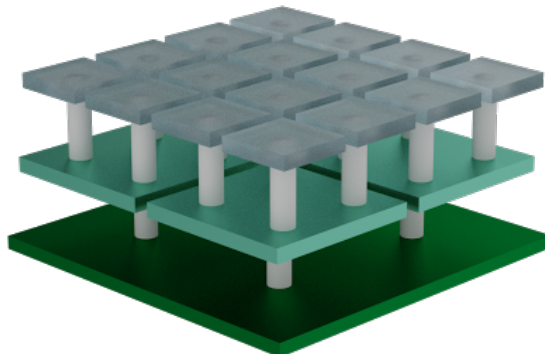
Figure 3.2: Same as Fig. 3.1 but for a quaternary TTNS.

ground states of *critical* one dimensional systems [41, 42], and therefore might provide more flexibility in encoding complex entanglement structures in two and higher dimensional systems. TTNS are used in the context of interacting lattice systems [43–48], but they feature more prominently in applications like electronic structure methods [49–51] or molecular quantum dynamics in the chemical physics literature. In this context they are called the Multi-Configuration Time-Dependent Hartree (MCTDH) method and its multi-layer generalization (ML-MCTDH) [52–54]. In ML-MCTDH, the time-dependent variational principle [55, 56] (TDVP) is applied to a TTNS as a variational ansatz for the wavefunction. Up to differences in the numerical integrations scheme, these methods are similar to the more recent applications of the TDVP tailored specifically to matrix product states [21, 22, 57–59].

The TDVP applied to TNS has been discussed as a method that may enable the accurate description of hydrodynamic transport in non-integrable systems when used with a moderate bond dimension [60], but was shown to not be a robust approximation for generic systems [61]. Several tensor network techniques have been designed to circumvent the entanglement growth on intermediate timescales with the goal of a reliable approximation to the long-time dynamics [62–68]. Despite promising results, the stability of such approximations for generic

systems, especially beyond one dimension, is not sufficiently established at this point. In this work, we thus consider the TDVP applied to TNS as a numerically exact technique, allowing to compute the dynamics of a system within a controllable accuracy up to some finite time, and generalize the algorithms of Refs. [22, 59, 69] to general TTNS. We note in passing that such algorithms have been used to find the ground state of a two-dimensional spin system [70] and to obtain the dynamics of a zero-dimensional model [71]. Recently, similar versions of this algorithm were reported in detail in Refs. [72, 73], which we became aware of during the preparation of this manuscript. While in our work we focus on two-dimensional systems, Ref. [72] showcases a promising application of a TTNS as an impurity-solver, which is an effectively zero-dimensional problem. On the other hand, Ref. [73] proves the algorithm's exactness property as well as a linear error-bound for the total time evolution in the time-step.

The purpose of this work is to investigate the performance of TTNS as a numerically exact method to study the dynamics of two-dimensional systems. In Sec. 7.2, we introduce the main concepts of TTNS along with the TDVP before presenting the algorithm and commenting on some caveats which are relevant to the applications of the TDVP. We benchmark the method on an exactly solvable, non-interacting two-dimensional system, and compare our approach to previously published results for two-dimensional interacting hardcore bosons in Sec. 7.4. Notably, we identify the reachable timescales and investigate convergence properties of the algorithm alongside with practical considerations regarding how to assess the accuracy of the results. We conclude by placing the results in the context of existing techniques and recent developments in Sec. 4.4.

3.2 Theory

Tensor network states represent a pure state, $|\Psi\rangle = \sum_{s_1 \dots s_N} \Psi_{s_1 \dots s_N} |s_1 \dots s_N\rangle$, of a lattice system as a product of tensors $\{T\}$. Each tensor T_i may have a number of indices corresponding to physical degrees of freedom and also auxiliary indices which do not correspond to physical degrees of freedom. Consider the Schmidt decomposition, corresponding to a bipartition of the lattice into a set of sites A and its complement B, $\Psi_{s_1 \dots s_N} = \sum_{i,j} \phi^A_{i\mathbf{s_A}} \lambda_{ij} \phi^B_{j\mathbf{s_B}}$ with $\lambda_{ij} = \delta_{ij} \lambda_i$. This expression can be also understood as a product of three tensors, where a single auxiliary index of each tensor is shared with the diagonal matrix of the Schmidt coefficients (or singular values) λ_i. In a general tensor network any auxiliary index will appear on two tensors, and summation over the common index implies contraction of the two tensors. Tensor networks can be represented diagrammatically, see Fig. 3.3a, where the nodes correspond to tensors and the links, dubbed *legs* in the following, indicate a shared index between the two tensors. Any tensor network for which the legs do not form closed loops is considered a *Tree Tensor Network (TTN)*, with matrix product states (MPS) serving as a prominent special case, which is mostly applicable for one-dimensional lattices. Here, we focus on more general TTNS with a simple hierarchical structure: *n-ary TTNS* in which every node has one *parent* node and n *child* nodes, except for those in the top and bottom layers. We group all physical degrees of freedom into the bottom layer such that all layers above the bottom layer contain only nodes with auxiliary legs (see Figs. 3.2, 3.3a) for illustration). Without restricting the generality, in this Section we will limit the discussion to binary TTNS. In such TTNS, a general node represents a third order tensor $\Lambda^{[l,i]}$, where l denotes the layer of the tree to which the node belongs, and i enumerates the nodes in that layer. Each such node has two child nodes. Due to the lack of loops in the tensor network, the physical degrees of freedom separate naturally into two groups from the perspective of a node $\Lambda^{[l,i]}$: those

reachable by only descending in the tree towards the bottom layer, i.e. those in the subtree of $\Lambda^{[l,i]}$, and their complement. We define the number of non-zero singular values of the Schmidt decomposition along this bipartition as the rank r of node $\Lambda^{[l,i]}$. For a state with volume law entanglement, the exact rank r will generally scale exponentially with the system size. Thus we introduce a cutoff in the number of kept singular values, namely the bond dimension of the tree χ. In the following, we consider a TTNS of rank χ, which implies that all its tensors $\Lambda^{[l,i]}$ have a rank of $\min\left(\chi, d^{N(l,i)}\right)$, where d denotes the local Hilbert space dimension and $N(l,i)$ is the number of sites in the subtree of $\Lambda^{[l,i]}$. The set of TTNS with a given rank χ constitutes a smooth manifold of states $\mathcal{M}_\chi$. The computational complexity for a binary TTNS is $\mathcal{O}\left(N \log N \chi^3\right)$ in memory and $\mathcal{O}\left(N \log N \chi^4\right)$ in computation where N is the number of physical degrees of freedom.

We next present a method for time-propagation on the manifold $\mathcal{M}_\chi$ of tree tensor networks with tree rank χ using a time-dependent variational principle (TDVP) [55, 56]. We start by introducing a few properties and manipulations of TTNS and then describe TDVP and its application to TTNS. We finally highlight important technical details in the use of the TDVP.

3.2.1 TTNS - Basics

A TTNS of a rank χ is unique up to unitary transformations. This can be seen by inserting a unit matrix between two linked nodes of the tree

$$\Lambda^{[l,i]}_{\alpha_1\alpha_2\alpha_3}\mathbb{I}_{\alpha_3\beta_1}\Lambda^{[l+1,j]}_{\beta_1\beta_2\beta_3} = \Lambda^{[l,i]}_{\alpha_1\alpha_2\alpha_3}U^*_{\alpha_3\gamma}U_{\gamma\beta_1}\Lambda^{[l+1,j]}_{\beta_1\beta_2\beta_3} = \tilde{\Lambda}^{[l,i]}_{\alpha_1\alpha_2\gamma}\tilde{\Lambda}^{[l+1,j]}_{\gamma\beta_2\beta_3}, \tag{3.1}$$
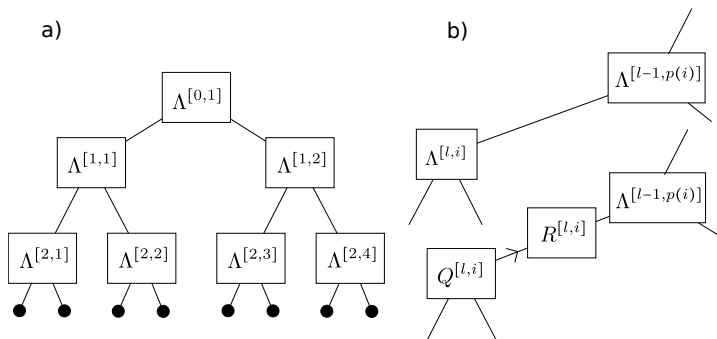
Figure 3.3: a) A binary TTNS for an 8-site system. The black dots correspond to physical sites and the square boxes with n legs represent n-th order tensors. b) Application of the QR decomposition to tensors in the TTNS. The upper and lower diagram represent the same TTNS. The arrow on the link indicates the direction along which the tensor is orthonormalized.

where repeated indices are summed over, $\mathbb{I}$ represents a $\chi \times \chi$ unit matrix and U^* indicates complex conjugation of the corresponding tensor. This property can be exploited to *isometrize* the tree around any of its nodes [47, 74], which is a generalization of the mixed canonical representation of MPS. To illustrate this concept, consider the *isometrization* about the top-node. In this perspective, every tensor in the tree, except the top-node, represents a truncated orthonormal basis in the space of the bases of child nodes, called *isometry* in the language of real-space or tensor RG. Through recursion, a structured, incomplete basis for the physical lattice sites is obtained. The coefficients for these basis functions are contained in the top node. Any general TTNS can be brought into this form using a sequence of QR decompositions. Practically, one applies QR factorization $\Lambda^{[l,i]}_{\alpha_1\alpha_2\alpha_3} = Q^{[l,i]}_{\beta\alpha_2\alpha_3} R^{[l,i]}_{\beta\alpha_1}$ with $Q^{[l,i]*}_{\beta\alpha_2\alpha_3} Q^{[l,i]}_{\gamma\alpha_2\alpha_3} = \delta_{\beta,\gamma}$, for each of the nodes proceeding layer by layer from bottom to top and absorbing the matrices R into the parent node after each factorization (see also Fig. 3.3b). Graphically, the direction along which the tensors are orthogonalized is indicated by an arrow on the linking leg. Isometrization around a specific node in the tree translates into arrows pointing in the direction of this node on any (direct) path between the node and a
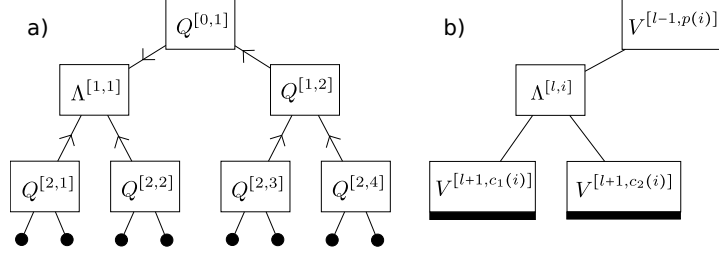
Figure 3.4: A TTNS isometrized about node [1,1], a), and its shorthand notation, b). The thick black bars on the environment tensors represent the set of physical sites belonging to each of the environment tensors. Note that orthogonality of the environment tensors in b) is not indicated by arrows on the legs, but implicit in their definition.

physical site, see Fig. 3.4b). We may rewrite the TTNS in the following manner:

$$\Psi[l,i]_{\mathbf{s}} = \Lambda^{[l,i]}_{\alpha_1\alpha_2\alpha_3} V^{[l-1,p(i)]}_{\alpha_1\mathbf{s}_1} V^{[l+1,c_1(i)]}_{\alpha_2\mathbf{s}_2} V^{[l+1,c_2(i)]}_{\alpha_3\mathbf{s}_3}. \tag{3.2}$$

Here, we take the TTNS to be isometrized about node $[l,i]$, indicated as $\Psi[l,i]$, and an environment tensor $V^{[l\pm1,p(i)/c_j(i)]}_{\alpha_j\mathbf{s}_j}$ is the contraction of all tensors between the legs of node $\Lambda^{[l,i]}$, labeled by α_j, and the physical sites $\mathbf{s}_j$, linked by paths from leg α_j that do not cross node $\Lambda^{[l,i]}$. $c_j(i)$ and $p(i)$ are placeholders for the child and parent of node $\Lambda^{[l,i]}$, respectively. We note in passing that similarly to MPS methods, such a contraction is never explicitly carried out, and we only use it for notational convenience. For future reference, we define projectors onto environment tensors of the lower and upper levels in the hierarchy: $\left(\Omega^{[l+1,c_{j-1}(i)]}\right)_{\mathbf{s}'_j\mathbf{s}_j} = V^{[l+1/c_{j-1}(i)]}_{\alpha_j\mathbf{s}'_j} V^{[l+1/c_{j-1}(i)]*}_{\alpha_j\mathbf{s}_j}$ and $\left(\Omega^{[l-1,p(i)]}\right)_{\mathbf{s}'_1\mathbf{s}_1} = V^{[l-1/p(i)]}_{\alpha_1\mathbf{s}'_1} V^{[l-1/p(i)]*}_{\alpha_1\mathbf{s}_1}$. A useful property of the environment tensors is their orthogonality, which allows for efficient calculation of certain physical quantities. For example, if the state is isometrized about node $[l,i]$, the norm of the state is given by $\langle\Psi[l,i]|\Psi[l,i]| =\rangle \Lambda^{[l,i]*}_{\alpha_1\alpha_2\alpha_3}\Lambda^{[l,i]}_{\alpha_1\alpha_2\alpha_3}$ since $V^{[l\pm1,p(i)/c_j(i)]*}_{\alpha_j\mathbf{s}_j} V^{[l\pm1,p(i)/c_j(i)]}_{\alpha'_j\mathbf{s}_j} = \delta_{\alpha'_j\alpha_j}$. To improve the readability of the presentation, in the following we will omit the indices specifying the elements of the tensors.

3.2.2 TDVP

The time-dependent variational principle generates classical dynamics in the space of varia-
tional parameters, α, described by the Lagrangian

$$\mathcal{L}[\alpha, \dot{\alpha}] = \langle \Psi[\alpha]| \, i\partial_t \, |\Psi[\alpha]\rangle - \langle \Psi[\alpha]| \, \hat{H} \, |\Psi[\alpha]\rangle . \tag{3.3}$$

The associated action is minimized along a path on a certain variational manifold, which in
our case is the manifold of TTNS with tree rank χ, $\mathcal{M}_\chi$. The principle of least-action yields
the following equation of motion,

$$i\partial_t \, |\Psi[\alpha]\rangle = P_T(\Psi[\alpha])\hat{H} \, |\Psi[\alpha]\rangle , \tag{3.4}$$

where $P_T(\Psi[\alpha])$ is the projector onto the tangent space of the manifold $\mathcal{M}_\chi$ at the point
$\Psi[\alpha]$. An expression for $P_T(\Psi[\alpha])$ was derived for general binary TTNS in Refs. [75, 76].
Here, we will use an additive splitting of $P_T(\Psi[\alpha])$, in an analogy to those presented for
TTNS with only two layers, i.e. Tucker tensors [69] and matrix product states [22, 59],
respectively. Note that the latter two TNS are subclasses of a general TTNS and that the
expressions for the projector, $P_T(\Psi[\alpha])$, is not restricted to binary TTNS and is valid for *any*
TTNS with straightforward modifications. In particular,

$$P_T(\Psi[\alpha]) = P_0 + \sum_{[l,i]} P_+^{[l,i]} - P_-^{[l,i]} \tag{3.5}$$

with

$$P_0 \;\; = \;\; \Omega^{[1,1]}\Omega^{[1,2]} \tag{3.6}$$

$$P_+^{[l,i]} = \Omega^{[l+1,c_1(i)]}\Omega^{[l+1,c_2(i)]}\Omega^{[l-1,p(i)]} \tag{3.7}$$

$$P_-^{[l,i]} = \Omega^{[l,i]}\Omega^{[l-1,p(i)]}. \tag{3.8}$$

Inserting this splitting into (3.4) leads to a set of projected Schrödinger equations for the tensors $\Lambda^{[l,i]}$ and matrices $R^{[l,i]}$. For example under the action of $P_+^{[l,i]}$ (see also 3.5):

$$i\partial_t \Psi[\alpha] = i\dot{\Lambda}^{[l,i]}(V^{[l-1,p(i)]}V^{[l+1,c_1(i)]}V^{[l+1,c_2(i)]}) + i\Lambda^{[l,i]}\partial_t(V^{[l-1,p(i)]}V^{[l+1,c_1(i)]}V^{[l+1,c_2(i)]})$$
$$= (V^{[l-1,p(i)]}V^{[l+1,c_1(i)]}V^{[l+1,c_2(i)]})H_{eff}^{[l,i]}\Lambda^{[l,i]}, \quad (3.9)$$

with the effective Hamiltonian environment

$$H_{eff}^{[l,i]} = (V^{[l-1,p(i)]}V^{[l+1,c_1(i)]}V^{[l+1,c_2(i)]})^*\hat{H}(V^{[l-1,p(i)]}V^{[l+1,c_1(i)]}V^{[l+1,c_2(i)]}). \quad (3.10)$$

We choose a convenient gauge in which the time-derivative of any tensor of the TTNS representation is orthogonal to itself. This must be done to avoid over-completeness of the basis of the tangent space. In this gauge the time derivative simplifies to

$$i\dot{\Lambda}^{[l,i]} = H_{eff}^{[l,i]}\Lambda^{[l,i]}, \tag{3.11}$$

which is obtained by contracting Eq. (3.9) with $(V^{[l-1,p(i)]}V^{[l+1,c_1(i)]}V^{[l+1,c_2(i)]})^*$. Similarly, we obtain for $R^{[l,i]}$, which results from the action of $P_-^{[l,i]}$,

$$i\dot{R}^{[l,i]} = \tilde{H}_{eff}^{[l,i]}R^{[l,i]}. \tag{3.12}$$
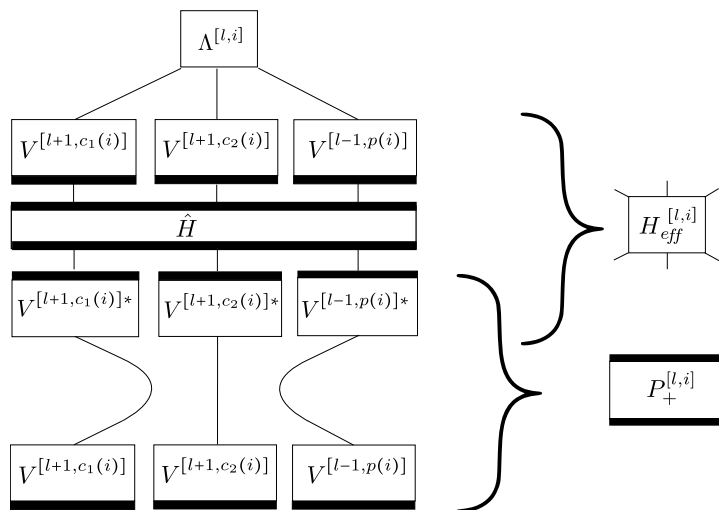
Figure 3.5: Graphical representation of the last line of Eq. (3.9), with identification of the effective Hamiltonian environment, $H_{eff}^{[l,i]}$, of Eq. (3.5) as well as part of the tangent space projector, $P_+^{[l,i]}$, of Eq. (3.7). In contrast to Fig. 3.4, the environment tensors have been brought on the same level regardless of layer for better readability.

with the effective Hamiltonian environment

$$\tilde{H}_{eff}^{[l,i]} = (V^{[l-1,p(i)]}V^{[l,i]})^* \hat{H}(V^{[l-1,p(i)]}V^{[l,i]}) \tag{3.13}$$

Time-evolution is obtained by integrating the linear differential equations Eqs. (3.11) and (3.12) using the projector splitting integrator. Evaluating the action of the Hamiltonian environments in Eqs. (3.10) and (3.13) generally requires a compressed representation of the Hamiltonian, for example as a matrix product operator (MPO) or tree tensor network operator (TTNO), in which case the environments are recursively contractible with the TTN. Alternatively one can express the Hamiltonian as a sum of rank-1 terms, in which case evaluating Eqs. (3.11) and (3.12) simplifies to a sum over matrix multiplications applied to the tensor for which the time-derivative is calculated. The number of Hamiltonian terms to be evaluated for a given site can be reduced by combining terms in the rank-1 decomposition

of the Hamiltonian during the recursive contraction.

3.2.3   Splitting integrator

Formally, the splitting integrator is obtained using a Trotter splitting applied to the additive decomposition of the tangent-space-projected evolution operator. Practically, it consists of a forward walk on the tree, propagation of the top-level tensor $\Lambda^{[0,1]}$ for a full time step, and a backward walk on the tree. A pseudo-code is given in algorithms 3.1-3.3. During the walks on the tree, isometrization of the TTNS is always maintained about the currently visited node and the effective Hamiltonian matrices are updated when going from one node to another along the direction of the step. The forward walk (backward walk) starts from the top-level node and proceeds from the current node to the adjacent node in a clockwise direction (in a counter-clockwise direction) closest to the previous/incoming node and propagation for half a time step is performed only while ascending (descending). A walk on the tree is finished once the top-node is reached after visiting all physical sites, i.e. after each tensor (and the associated matrix R) is propagated save those of the top node.

3.2.4   Remarks

The algorithm introduced above is a generalization of a previously published projector-splitting integrator for TTNS with a single-layer [69, 77]. Ref. [73] describes an algorithm for a general TTNS, which is identical to the above algorithm with a single (either forward or backward) walk per time-step. The main differences between the algorithm of Ref. [72] and the one presented here are in the definition of the walk on the tree and in the absence of a top-node, including it's separate propagation routine.

While the TDVP applied to MPS has been demonstrated to be capable of simulating

---

Algorithm 3.1 Forward walk

Input: $\Psi[l, i]$, current node $[l, i]$, next node $[l - 1, p(i)]$
Output: $\Psi[l - 1, p(i)]$
  1: **if** in forward loop **then**:
  2:     $\Lambda^{[l,i]}(t_{1/2}) \leftarrow \text{propagate}(\Lambda^{[l,i]}(t_0), h/2)$
  3:     compute QR fact. $\Lambda^{[l,i]}(t_{1/2}) = Q^{[l,i]}(t_{1/2})R^{[l,i]}(t_{1/2})$
  4:     $\Lambda^{[l,i]}(t_{1/2}) \leftarrow Q^{[l,i]}(t_{1/2})$
  5:     $R^{[l,i]}(t_0) \leftarrow \text{propagate}(R^{[l,i]}(t_{1/2}), -h/2)$
  6:     $\Lambda^{[l-1,p(i)]}(t_0) \leftarrow\leftarrow Q^{[l-1,p(i)]}(t_0)R^{[l,i]}(t_0)$
  7: **else**
  8:     compute QR fact. $\Lambda^{[l,i]}(t_1) = Q^{[l,i]}(t_1)R^{[l,i]}(t_1)$
  9:     $\Lambda^{[l,i]}(t_1) \leftarrow Q^{[l,i]}(t_1)$
10:     $\Lambda^{[l-1,p(i)]}(t_1) \leftarrow Q^{[l-1,p(i)]}(t_1)R^{[l,i]}(t_1)$
11: **end if**

Algorithm 3.2 Backward walk

Input: $\Psi[l, i]$, current node $[l, i]$, next node $[l + 1, c_j(i)]$
Output: $\Psi[l + 1, c_j(i)]$
  1: **if** in backward loop **then**:
  2:     compute QR fact. $\Lambda^{[l,i]}(t_1) = Q^{[l,i]}(t_1)R^{[l,i]}(t_1)$
  3:     $\Lambda^{[l,i]}(t_1) \leftarrow Q^{[l,i]}(t_1)$
  4:     $R^{[l,i]}(t_{1/2}) \leftarrow \text{propagate}(R^{[l,i]}(t_1), -h/2)$
  5:     $\Lambda^{[l+1,c_j(i)]}(t_{1/2}) \leftarrow Q^{[l+1,c_j(i)]}(t_{1/2})R^{[l,i]}(t_{1/2})$
  6:     $\Lambda^{[l+1,c_j(i)]}(t_1) \leftarrow \text{propagate}(\Lambda^{[l+1,c_j(i)]}(t_{1/2}), h/2)$
  7: **else**
  8:     compute QR fact. $\Lambda^{[l,i]}(t_0) = Q^{[l,i]}(t_0)R^{[l,i]}(t_0)$
  9:     $\Lambda^{[l,i]}(t_0) \leftarrow Q^{[l,i]}(t_0)$
10:     $\Lambda^{[l+1,c_j(i)]}(t_0) \leftarrow Q^{[l+1,c_j(i)]}(t_0)R^{[l,i]}(t_0)$
11: **end if**

Algorithm 3.3 Propagation of top-node's tensor

Input: $\Psi[0, 1](t_0)$
Output: $\Psi[0, 1](t_1)$
  1: $\Lambda^{[0,1]}(t_1) \leftarrow \text{propagate}(\Lambda^{[0,1]}(t_0), h)$

---

dynamics in two-dimensional systems [36], a detailed analysis and comparison with other tensor network structures is absent in the literature. In particular, the numerical stability of the TDVP cannot be taken for granted [78], especially when interactions between sites are long-ranged and not smoothly decaying, as discussed in the following.

The application of TDVP formally requires the TTNS corresponding to the initial condition to possess a full tree rank of $\mathbf{r}$. However, many physical initial conditions of interest can be represented with a low rank TTNS or even as a product state. If the initial condition is not contained in the manifold of TTNS with tree rank of $\mathbf{r}$ due to rank deficiency, the TDVP doesn't provide a prescription for how to choose and evolve the redundant parameters, which will gain weight in the wavefunction representation at later times. Stability and exactness of the dynamics under such circumstances is then dependent on details of the implementation and the model. For the projector splitting integrator, the initial rank-deficiency translates into non-uniqueness of the matrix decompositions employed in the change of isometrization. While the algorithm is not guaranteed to be exact in this case, numerical experiments and prior applications of the algorithm in one-dimensional systems indicate that it is generally reliable even for product state initial conditions. As a check, one may choose to regularize the initial condition by the addition of weak noise, and test for invariance of the resulting dynamics at short times. The initial evolution of redundant variational parameters depends on arbitrary choices such as their initialization, the choice of regularization (if applied), as well as the details of the linear algebra routines used. Thus, different initializations of the same physical state may not converge to the same solution [79, 80]. Several approaches have been developed to address this problem. In one-dimensional systems with nearest-neighbour interactions, the commonly used two-site version of the TDVP algorithm of Ref. [22] is free of this issue, although this comes at the cost of breaking unitarity of the evolution when the

results cease to be close to the exact solution. For generic interactions and arbitrary TTNS, a scheme to optimally initialize redundant parameters was introduced [80]. However, this scheme requires the evaluation of an effective Hamiltonian matrices for $\hat{H}^2$ and its compatibility with the integration scheme employed here is an open question. Recently, another approach based on a global basis expansion for MPS has been presented, and should also be applicable to general TTNS [78].

Practically, we observe that the dependence of our results on non-optimal initializations of redundant parameters systematically decreases with increasing bond-dimension, which is also expected from the derivation of the optimization scheme mentioned above. The dependence on initialization becomes noticeable only when the wavefunction markedly departs from the exact result, which provides an additional handle to access the convergence of the method.

3.3 Results

We first benchmark the method developed in this work by comparison with exact results obtained for non-interacting fermions on a 2D lattice. In the second stage we propagate a 2D system of hard-core bosons with nearest neighbor interactions and compare our results to propagation using MPS [35]. The mapping of physical sites to the respective tensor network structure is illustrated in Figs. 3.1 and 3.2. All calculations employ a regularization of the initial product state, which consists of addition of white noise sampled uniformly from the interval $[-10^{-20}, 10^{-20}]$ and subsequent renormalization of the TTNS.

3.3.1 Non-interacting fermions

We compute the dynamics of non-interacting fermions on a 2D lattice with on-site disorder

$$\hat{H} = J \sum_{<i,j>} \left(\hat{c}_i^\dagger \hat{c}_j + \hat{c}_j^\dagger \hat{c}_i \right) + \sum_i h_i \left(\hat{c}_i^\dagger \hat{c}_i - \frac{1}{2} \right), \tag{3.14}$$

where the index $\boldsymbol{i} = (x, y)$ indicates the position of the fermion on the lattice, $\langle . \rangle$ is a sum over nearest-neighbours, h_i is drawn from a uniform distribution $[-W, W]$ and $J = 1$. All simulations use an identical initial state which is a random product state at half-filling, and use a time step $dt = 0.01$. The tensor network state calculations employ the Jordan-Wigner transformation of (3.14)

$$\hat{H} \quad = \quad \sum_{<j,k>,j<k} \hat{S}_j^+ \left(\prod_{j \leq l < k} 2\hat{S}_l^z \right) \hat{S}_k^- \;+\; \hat{S}_j^- \left(\prod_{j < l \leq k} 2\hat{S}_l^z \right) \hat{S}_k^+ \;+\; W \sum_i h_i \hat{S}_i^z. \tag{3.15}$$

Different paths along which the sites are enumerated can be chosen, and this choice potentially influences the performance of the TNS algorithm. Here, we choose the path such that the Jordan-Wigner strings span a minimal distance on the graph of the tree tensor network structure. While solving the non-interacting problem in the fermionic representation is trivial, the presence of Jordan-Wigner strings renders its solution with tensor network states just as difficult as that of an interacting problem. We compute the dynamics of this mode both for a clean system ($W = 0$) and for one realization of a moderately strong quenched disorder ($W = 10$). Two-dimensional non-interacting fermions show Anderson localization at any finite disorder strength. While the localization length may exceed the lattice dimensions chosen, disorder nonetheless slows the growth of entanglement and should allow access to longer timescales. Indeed, we observe good agreement for the density profiles, $\hat{n}_{x,y} = \hat{c}_{x,y}^\dagger \hat{c}_{x,y}$

with $x, y \in [1, L]$, along a horizontal cut of the lattice between the exact result and data from both binary and quaternary TNS only up to times $t \leq 1$ for the clean system, while longer times are accessible in the disordered case (see Fig. 3.6). If the time-step is chosen sufficiently small, errors associated to the linearization of Eq. (3.4) are negligible compared to inaccuracies related to the finite bond dimensions at all but the earliest times (see lower panel of Fig. 3.6). To get a more complete picture of the growth of errors with time as well as their dependence on TNS structure and bond dimension, in Fig. 3.7 we show the average error in the expectation value of the local density as a function of time. Both TNS structures show systematic improvement with increasing bond dimension, and the error grows more mildly at intermediate times in the disordered case. In both cases, smaller deviations from exact results are achievable for binary TTNS than for quaternary TTNS at the employed bond dimensions. We find that a convergence criterion of an average error in the local density of about 2% agrees well with the qualitative analysis of Fig. 3.6 and gives a good estimate of the times up to which the TNS results are reliable.

3.3.2 Hard-Core Bosons (XXZ model in 2D)

We consider the dynamics of hard-core bosons on a 2D lattice ,

$$\hat{H} = -J \sum_{<i,j>} \left(\hat{b}_i^\dagger \hat{b}_j + \hat{b}_j^\dagger \hat{b}_i \right) + V \sum_{<i,j>} \hat{b}_i^\dagger \hat{b}_i \hat{b}_j^\dagger \hat{b}_j$$

with nearest-neighbor interactions and we set $V = J = 1$. We choose an initial condition with a central square sublattice occupied and all other lattice sites empty. This system and initial condition have been studied previously in Ref. [35] using MPS, where results up to $tJ = 2.0$ were presented for a square lattice of linear length $L = 14$. To establish the
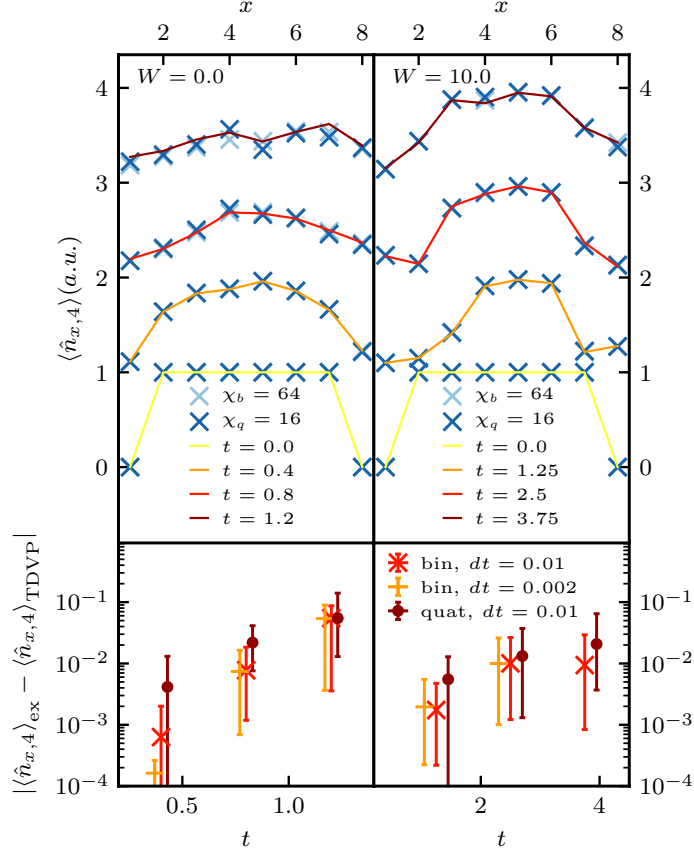
Figure 3.6: Density profiles of a central, horizontal cut in the fourth row for a random product state configuration of non-interacting fermions on a 8x8 lattice. *Upper panels*: Profiles for $W = 0$ (left) and $W = 10$ (right). Later times are spaced upwards by 1 for readability. TDVP results for binary tensor network with $\chi_b = 64$ (light blue crosses) and quaternary tensor network with $\chi_b = 16$ (dark blue crosses), both with $dt = 0.01$, shown on top of exact results (solid lines). *Lower panels*: The caps of the error bars represent the maximal and minimal deviation of the profiles in the above panels from the exact result for different bond-dimensions, tensor network structures and time-steps.
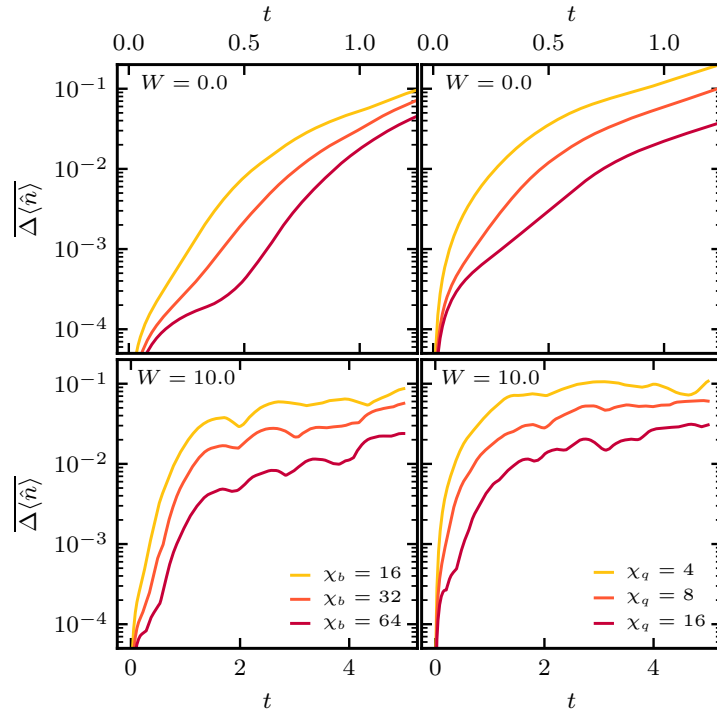
Figure 3.7: Average deviation from exact $\langle \hat{n}(t) \rangle$ expectation value per site for non-interacting fermions on a clean (top panels) and a disordered (bottom panels, $W = 10$) 8x8 lattice with open boundary conditions. Left panels are binary TTNS and right panels are quaternary TTNS. The time step used is $dt = 0.01$.

numerical exactness of the algorithm for this non-integrable model, we compare the results for the local bosonic density $\hat{n}_{x,y} = \hat{b}_{x,y}^{\dagger}\hat{b}_{x,y}$ with $x, y \in [1, L]$, for both binary and quaternary tensor networks with exact diagonalization for a square lattice of linear length $L = 4$, with the central 4 lattice sites occupied (see Fig. 3.9). Deviations from the exact result become noticeable only for times $t \approx 2$.

Having established the validity of the algorithm, we investigate the dynamics of an initial product state of a filled, central 4x4 sublattice in a square lattice of a linear length $L = 16$, see Fig. 3.8. In the upper panel of Fig. 3.10, we focus on the bosonic density for the site in the fourth row and fourth column of the lattice. In contrast to the non-interacting model and the small two-dimensional lattice discussed above, no exact results are available for this interacting system and $L = 16$. Therefore, the convergence of the results is assessed by comparing the deviation of the local density between different bond dimensions. All examined bond dimensions agree well up to times $t \sim 1.0$. For later times we see agreement for all but the lowest bond dimensions in both quaternary and binary TNS. However, *quantitative* agreement (within a deviation of 0.001) up to $t = 1.5$ only holds between the binary TNS results with $\chi_b = 128$, $\chi_b = 64$ and the MPS results of Ref. [35] at $\chi = 400$ and $\chi = 500$. Since the accuracy of n-ary TTNS can show site-dependence [70], we also report the average density deviation with respect to the best available calculation in the respective TNS structures in Fig. 3.10. The averaged density supports the observations made for a diagonal site both quantitatively and qualitatively. Particularly, an average deviation of 0.001 is reached at $t = 1.5$ for binary TNS, while quaternary TNS saturate the threshold at $t = 1.2$. The MPS results of Ref. [35] are converged to within this accuracy up to $t = 1.3$, while the deviation between the reference results of both binary TNS and MPS reach the threshold at $t = 1.4$.

Furthermore, since the Hamiltonian and the initial condition are isotropic, distance from the exact solution can also be assessed by the anisotropy,

$$A(t) = \frac{1}{\sum_{x,y=1}^{L} n_{x,y}(t)} \sum_{x,y=1}^{L} |\hat{n}_{x,y}(t) - \hat{n}_{y,x}(t)| ,$$

of the bosonic density, also reported in Fig. 3.10. We note however, that while the isotropy of the numerical solution is required, it is not a sufficient condition for the solution to be numerically exact. For both quaternary and binary TTNS, small anisotropies ($< 0.3\%$) are obtained up to their respective convergence times. In Ref. [35], an anisotropy of 4% was reported at $t = 2.0$ using MPS, a threshold which neither binary nor quaternary TTNS saturate at the longest simulated times. Generally, the quaternary TTNS has less anisotropic error since the partitioning of the lattice through the tree structure is isotropic, although the result is less tightly converged than the binary TTNS. Thus, anisotropy is only a useful indicator of convergence when comparing TTNS of the same structure. Given the small deviations in both anisotropy and local densities, we consider our results to be numerically exact up $t = 1.5$ for binary TTNS with $\chi_b = 128$, and up to $t = 1.2$ for quaternary TTNS with $\chi_q = 16$. The performance of the TDVP applied to binary TTNS is thus comparable with the results of Ref. [35], providing the gain of better isotropy of the solution. Note that the bond dimension used for MPS calculations do not correspond to the current state-of-the-art, and larger bond dimension may be feasible for binary TNS when using symmetries of the Hamiltonian. Due to the lack of an exact solution to compare to, the convergence criterion employed is significantly tighter than in the case of free fermions to ensure quantitatively accurate results.
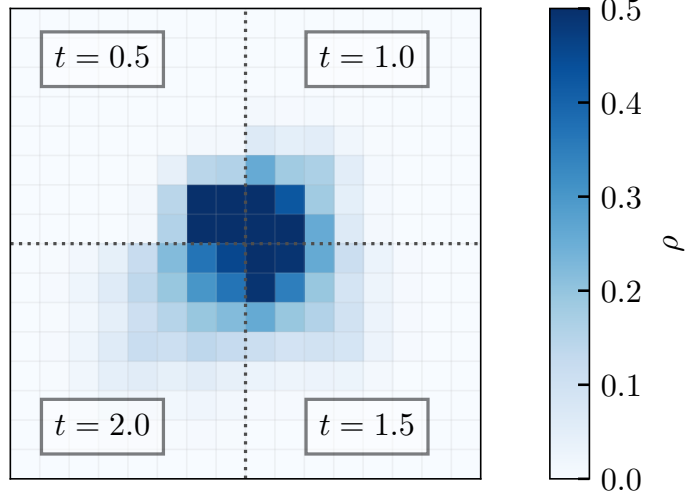
Figure 3.8:   Spreading of hard-core boson density $\langle \hat{n}_{x,y} \rangle$, initially occupying the central 4-by-4 sublattice of a square lattice with $L = 16$. Time step used is $dt = 0.01$, and the scale is restricted to a maximum of $n_i = 0.5$ for clarity.
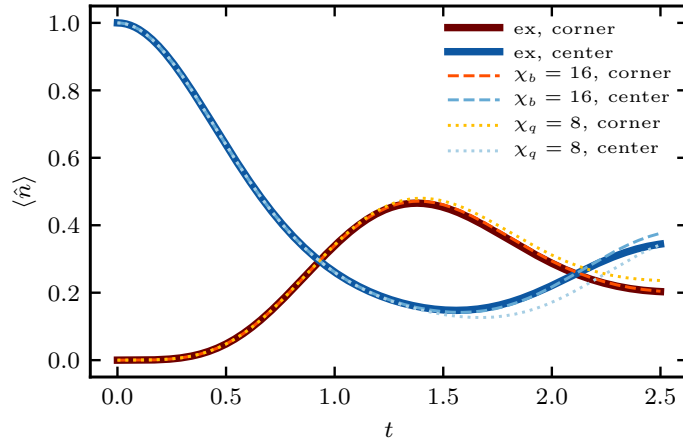
Figure 3.9: Bosonic site density as a function of time for a 4x4 lattice with the central 2x2 sites filled at $t = 0$. Two special sites are shown (corner and central). Exact results (solid lines) and TNS results for binary (dashed lines) and quaternary (dotted lines) TNS. Time step used for both panels is $dt = 0.01$.
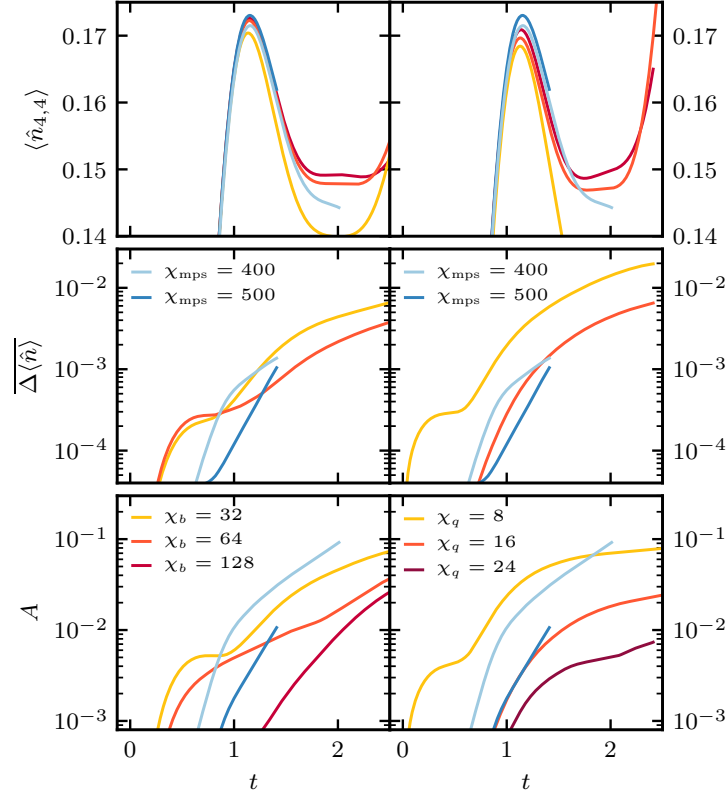
Figure 3.10: Measures of convergence for hard-core bosons in 16x16 lattice for binary (left panels) and quaternary (right panels) TTNS as well as MPS [35] (all panels, blue shades). *Upper panels*: Bosonic density for the 4th left and 4th topmost site. *Middle panels*: Average deviation of the local bosonic density with respect to best available result within the respective TNS structure, for binary TTNS and MPS (left panel) as well as quaternary TTNS and MPS (right panel). For $\chi_{\mathrm{mps}} = 500$, the deviation is reported with respect to $\chi_b = 128$. . *Bottom panels*: Anisotropy (see text) of bosonic density. The time step used is $dt = 0.01$.

3.4 Discussion

In this work we have assessed the performance of TTNS for simulating the dynamics of two-dimensional many-body lattice systems. We introduced an algorithm based on the time-dependent variational principle for arbitrary TTNS and benchmarked it on systems of non-interacting fermions and interacting hard-core bosons in two dimensions, comparing the performance to previously published results using matrix product states. During the preparation of the manuscript we became aware of a recent complementary work introducing a similar versions of the algorithm, which were applied in rather different settings (as an impurity solver [72], and in a more formal derivation of the algorithm [73]).

Currently, no efficient technique exists for exactly simulating the non-equilibrium dynamics of interacting, two-dimensional quantum systems. Despite recent progress, the timescales accessible by tensor network techniques for such systems are generally extremely short. We have found tree tensor networks to perform at least as well as matrix product state techniques, with binary TTNS generally providing a more robust performance than their quaternary counterparts. The issue of analyzing the convergence, and thus ensuring the numerical exactness of the computed result, was discussed. We believe the availability of an alternative to matrix product states in the form of more general TTNS is important and can offer additional insight in situations when slow convergence is observed.

Our analysis has been mostly qualitative and a promising future avenue is the exploration of the entanglement structure of out-of-equilibrium states in 2D lattices . This will aid in the identification of optimal tensor network structures in order to best exploit the increased flexibility of TTNS, which already has proven to be important in applications for zero-dimensional systems, such as impurity models and also for molecular quantum dynamics [71, 72, 81–83]. The dynamics of one-dimensional systems quenched to a critical point

is another application where such an increased flexibility may be of advantage. For critical systems in equilibrium, the multi-scale entanglement renormalization (MERA) [84, 85] ansatz provides an efficient tensor network structure, which bears resemblance with the n-ary tree structures employed here. However, since a time-evolution approach for MERA is missing, it is interesting to compare the performance of MPS and n-ary TTNS for critical systems out-of-equilibrium. We leave such an investigation to a future work.

Chapter 4

Multi-set Matrix Product State Calculations Reveal Mobile Franck-Condon Excitations Under Strong Holstein-type Coupling

4.1   Introduction

Holstein-type vibronic coupling, the coupling of local vibrations to the transition energies of electrons, holes, and excitons, is at the core of myriad important dynamical phenomena in the physical sciences. In addition to its importance in many inorganic systems, of particular current interest is its manifestation in organic molecular materials [87], with implications for

photosynthetic energy transfer [88–90] and singlet exciton fission [91–95], among many other applications. At the same time, the Holstein model continues to pose a considerable challenge for theory, encompassing a rich parameter space involving energy scales that include the electronic interaction strength (J), the vibrational energy (ω_0), the vibrational reorganization energy ($g^2\omega_0$), and the temperature. While certain limits of this space are amenable to perturbative approaches [96–100], no (semi)analytical treatment is available in the regime where J, ω_0, and $g^2\omega_0$ are comparable. This regime, where strong mixing between vibrational and electronic coordinates occurs, is representative of many organic materials, and has been the target of various numerically-exact techniques that have emerged over the recent years. Such techniques are based on either an elimination of vibrational coordinates (by means of a system-bath decomposition) [101–104] or an explicit but truncated representation of the entire vibronic system [105, 106]. However, both approaches rapidly become prohibitively expensive with increasing number of electronic and vibrational degrees of freedom. This scaling issue drastically worsens with increasing vibrational reorganization energies, as system-bath decompositions become difficult to converge and explicit descriptions demand the inclusion of an ever increasing set of bosonic states representing the vibrational coordinates. As a result of this lack of viable methodologies, much remains to be learned about how charges and excitons dynamically interact with strongly-coupled vibrations.

In this Letter, we employ the remarkable computational benefits offered by tensor network states to explore the nonequilibrium excitation dynamics resulting from the single-mode Holstein model in its electronic single-particle sector, covering the full range of the vibronic coupling strength, g, and including the strong-mixing regime. We pay special attention to initial conditions corresponding to different local excitations of the uncoupled Hamiltonian. For initial excitations that are vibrationally relaxed in the (shifted) excited state vibrational

potential, we find the mobility to decline with increasing g, as expected for Holstein polarons. However, for Franck-Condon (sudden) excitations, we find the g-dependence to be markedly weakened for a surprisingly long time period after initialization. Concomitantly, we find the quasi-ballistic transport found in the weak coupling limit to be replaced by a pulsed transfer mechanism. An analysis of transient vibrational overlap factors shows that this mechanism is driven by a vibrational oscillation of the Franck-Condon excitation, which protects the excited state from self-localizing while allowing periodic resonances during which effective excitation transfer occurs. This mechanism allows the excitation to attain a substantial root mean square displacement (RMSD) in coupling regimes where vibrationally-relaxed excitations are essentially immobile.

Tensor network states, in particular in their matrix product state (MPS) form, have gradually attained popularity as an efficient and accurate framework for describing large interacting quantum systems [13, 14]. Ground states of gapped one-dimensional systems are known to be efficiently representable by MPSs [11, 107]. Similarly, MPSs have gained considerable traction in the application to nonequilibrium dynamics, although considerable challenges remain due to the exponential scaling of their computational cost with time for general, ergodic systems [24]. Furthermore, while ample applications can be found in strongly-correlated many-body physics, MPSs have remained relatively underrepresented in single-particle electronic problems and in particular those concerning the single-mode Holstein model, even though examples targeting the ground state of its Hamiltonian have appeared as early as two decades ago [108]. Exceptions can be found for zero-dimensional models with few electronic states coupled to a potentially large number of modes, the dynamics of which have been treated by related tensor network state techniques since the 1990s [71, 81, 109, 110]. The last few years have seen the appearance of a few notable works showing promising re-

sults for MPS-based calculations of the Holstein model [111–113], yet the utility of tensor network states to this class of problems has remained largely unexplored. In this Letter, by demonstrating that MPSs allow access to unprecedented time and length scales for the single-particle Holstein model in the strong-mixing regime, we showcase their potential for studying a host of polaronic phenomena.

4.2 Theory

For a lattice consisting of N sites, the Holstein Hamiltonian in its electronic single-particle sector can be expressed in terms of J, g, and ω_0 as

$$\hat{H} = \omega_0 \sum_{\alpha=1}^{N} \hat{b}_\alpha^\dagger \hat{b}_\alpha + g\omega_0 \sum_{\alpha=1}^{N} (\hat{b}_\alpha^\dagger + \hat{b}_\alpha) \, |\alpha\rangle\langle\alpha| + J \sum_{<\alpha,\beta>}^{N} |\alpha\rangle\langle\beta| \,, \tag{4.1}$$

where $\hat{b}_\alpha^{(\dagger)}$ is the annihilation (creation) operator for a local mode coupled to an electronic excitation $|\alpha\rangle = \hat{c}_\alpha^\dagger |0\rangle$ at site α, with $\hat{c}_\alpha^\dagger$ as the electronic creation operator and $|0\rangle$ as the electronic vacuum. The last summation is limited to nearest-neighboring sites, α and β. Note that this Hamiltonian includes local coupling of each electronic site to a single, dispersionless Einstein oscillator. More general coupling schemes would pose no difficulty for the applied methodology, but are beyond the scope of the present study.

Tensor network states employ the principle that the wavefunction coefficients of a state in a Hilbert space for N sites can be thought of as a tensor of order N. Decomposing this tensor into a product of smaller tensors, and truncating these tensor products, replaces the exponential scaling with N by a low polynomial (usually linear) scaling. In case of MPSs,

such a decomposition takes the form

$$|\Psi\rangle = \sum_{\{\sigma_i\}} A_1^{\sigma_1} A_2^{\sigma_2} \ldots A_N^{\sigma_N} |\sigma_1 \sigma_2 \ldots \sigma_N\rangle, \tag{4.2}$$

where the indices σ_i label the physical basis states, and the A-tensors satisfy $A_i^{\sigma_i} \in \mathbb{C}^{\chi_{i-1} \times \chi_i}$. Here, the "bond dimension" χ_i controls the truncation applied to the internal (virtual) indices. The degree of entanglement between bipartitions of the system that can be accounted for by a tensor network is determined by its bond dimensions as well as its connectivity. Nonequilibrium dynamics generally leads to a (stretched) exponential increase of the bond dimension necessary to describe the state accurately with time, with the exception of localized systems [114, 115]. Thus, it is crucial to select a tensor network ansatz that captures the entanglement build-up efficiently in order to simulate physically-relevant time scales.

For the Holstein model, an obvious choice for the tensor network ansatz is to consider the Hamiltonian as a chain of spinless noninteracting fermions, each of which is coupled to its respective vibrational mode. After performing a Jordan-Wigner transformation on the fermions, this problem can straightforwardly be treated as an MPS. However, the reachable timescale under this ansatz is limited due to the relatively fast growth of entanglement entropy. An alternative approach considers the single-particle Holstein model as an N-level impurity, the levels of which correspond to the electronic single-particle states, where each level is coupled to its respective mode. Within the realm of MPSs, this impurity model is treated as an effectively one-dimensional problem. However, the resulting connectivity introduces long-range interactions between the vibrational coordinates and the impurity site, again leading to a rapid growth of entanglement.

Our tensor network ansatz is closely related to the N-level impurity approach, but instead

of solving the entire system as a single MPS, we express its wavefunction in terms of a set of products of electronic states and associated vibrational wavefunctions,

$$|\Psi\rangle = \sum_{\alpha=1}^{N} |\Psi^{\alpha}\rangle |\alpha\rangle. \tag{4.3}$$

The vibrational wavefunctions, $|\Psi^{\alpha}\rangle$, are then each expanded independently as an MPS with a bond dimension χ', analogous to Eq. 4.2, the norm of which corresponds to the electronic population at site α. The indices σ_i label the vibrational states using the bosonic occupation number basis associated with the (unshifted) ground state harmonic potential, which are truncated beyond a maximum number of quanta, $\nu_{\max}$. Note that such a *multi-set* approach was first introduced [109, 116] for multi-configuration time-dependent Hartree methods [52, 53], a related tensor network state technique, and was very recently employed in an MPS setting close in spirit to the one applied here [113]. Our multi-set MPS at a given bond dimension χ' can be converted to a standard MPS for the Jordan-Wigner transformed Holstein model mentioned above. The resulting bond dimension χ is tightly lower-bounded by χ' and loosely upper-bounded by $N\chi'$. As such, the favorable bond dimension of the multi-set MPS renders it a promising tensor network for obtaining both ground states and nonequilibrium time evolution, the latter being explored in this Letter. Despite introducing a quadratic scaling with the system size, we find the multi-set MPS approach to achieve remarkably long length and time scales.

To obtain the time evolution of $|\Psi\rangle$, we use the time-dependent variational principle [55, 56], which allows the (time-local) optimal approximate solution of the time-dependent Schrödinger equation to be computed, given a variational ansatz (such as the multi-set MPS

as employed in this work) [21, 22]. It amounts to solving the projected Schrödinger equation,

$$i|\dot{\Psi}\rangle = \hat{\mathcal{P}}_{\mathcal{M}}[|\Psi\rangle]\hat{H}|\Psi\rangle, \tag{4.4}$$

where $\hat{\mathcal{P}}_{\mathcal{M}}[|\Psi\rangle]$ is the projector onto the tangent space of the variational manifold $\mathcal{M}$ attached to $|\Psi\rangle \in \mathcal{M}$. The resulting dynamics is numerically exact up to times for which the variational ansatz fails to capture the produced entanglement accurately, and can be systematically converged to longer times by increasing the bond dimension. All presented data is obtained with a timestep of $dt = 0.1$ and is tightly ($< 1\%$ deviation in the RMSD) converged with respect to boundary effects as well as all numerical parameters (see Table 4.1 and Section 4.7). Applying less stringent convergence criteria is tempting; however, there is numerical evidence that loose convergence of asymptotic properties can yield qualitatively incorrect results [61].

	1D								2D	
g	0.5	1.0	1.5	2.0	2.5	3.0	3.5	4.0	0.5	2.0
$\nu_{\max}$	8	16	16	64	64	64	128	128	8	64
χ'	16	16	16	16	32	32	32	32	16	32
N	301	75	75	51	25	25	25	25	15×15	11×11
dt				0.1					0.1	

Table 4.1: Numerical parameters for the different applied coupling strengths, g, in one and two spatial dimensions: local bosonic Hilbert space dimension, $\nu_{\max}$, bond dimension, χ', number of lattice sites, N, and timestep, dt.

Not being limited to ground state or band-edge excited states, we are free to differentiate between the following two vibrational initial conditions for a local (in real space) electronic excitation. The first condition is that of an excitation vibrationally relaxed in the (electronically) excited state potential (referred to as "relaxed"), whereas the second corresponds to an excitation created upon a vertical transition starting from the zero-vibrational (electronic)
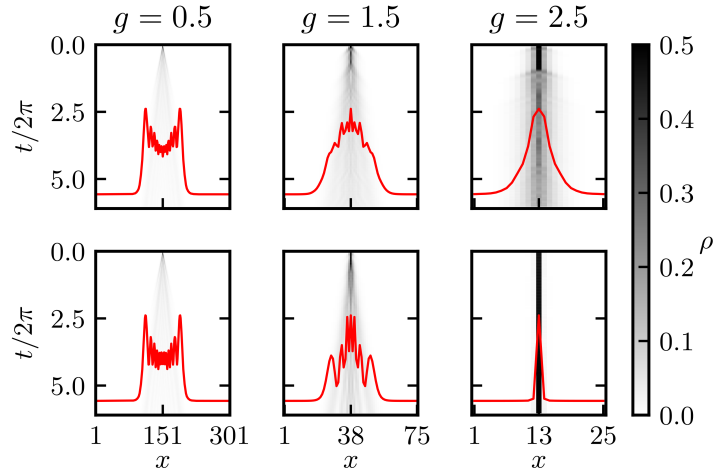
Figure 4.1:   Excitation density ρ as a function of time (vertical) and site (horizontal) for Franck-Condon (upper panels) and relaxed (lower panels) excitations. Red curves show the excitation density profile at $t/2\pi = 6$.

ground state level (known as a Franck-Condon excitation). These two cases can be regarded as the two extremes spanning the scope of commonly used nonequilibrium initial conditions. The Franck-Condon excitation is representative of an impulsive optical excitation of a vibronic system involving a vibration whose energy is large compared to the thermal quantum, which is satisfied by most functionally-relevant Holstein modes studied in the literature. The relaxed excitation, on the other hand, is a pragmatic initial condition for models involving a "shifted" basis for describing (electronically) excited state vibrations [117], and can be regarded as a proxy for optical pumping into the lowest-energy vibronic $(0-0)$ transition. For the dynamics of electronic excitations localized in momentum space, we refer the reader to Ref. 118.

4.3 Results

In Fig. 7.1 we present excitation dynamics for a linear chain with open boundaries, following an initial excitation located at the chain center, under the two aforementioned vibrational preparations. Shown as heatmaps are the calculated chain populations as a function of time (in units of inverse energy, with $\hbar = 1$) resulting from the Holstein model with $\omega_0 = J = 1$ and for varying values of g. The dynamics for $g = 0.5$ is near-identical for both initial vibrational conditions, which is consistent with the notion that these conditions become equivalent in the limit of $g \to 0$, and is dominated by a ballistic component characteristic of a vibronically-uncoupled excitation. The excitation mobility can be seen to decrease with increasing g, indicative of the formation of a polaron with increasing effective mass, including a rapid decline of the mobility of a relaxed excitation in the regime of strong coupling, as a result of self-localization. However, in marked contrast to the relaxed excitation, the Franck-Condon excitation is seen to retain a substantial mobility even under strong coupling. This trend is shown more systematically in Fig. 7.2, which depicts the transient RMSD for values of g ranging from 0 to 4. For $g = 2.5$, the Franck-Condon excitation spread rapidly reaches ∼6 sites, whereas the relaxed excitation remains essentially stalled on a single site.

An alternative means of demonstrating the contrasting dynamics emerging from relaxed and Franck-Condon excitations is by plotting the RMSD at a fixed time for varying g. This is shown in Fig. 4.3 for $t/2\pi = 6$. Here, the delocalization of the relaxed excitation shows a pronounced drop with g exceeding unity, which is almost entirely absent for the Franck-Condon excitation. Interestingly, within this coupling range we see the emergence of a beating pattern for the Franck-Condon excitation dynamics in Fig. 7.2, with 2π-periodic enhancements in the RMSD becoming more abrupt with increasing g. This indicates that their dynamics stems from a mechanism that is radically different from that of relaxed
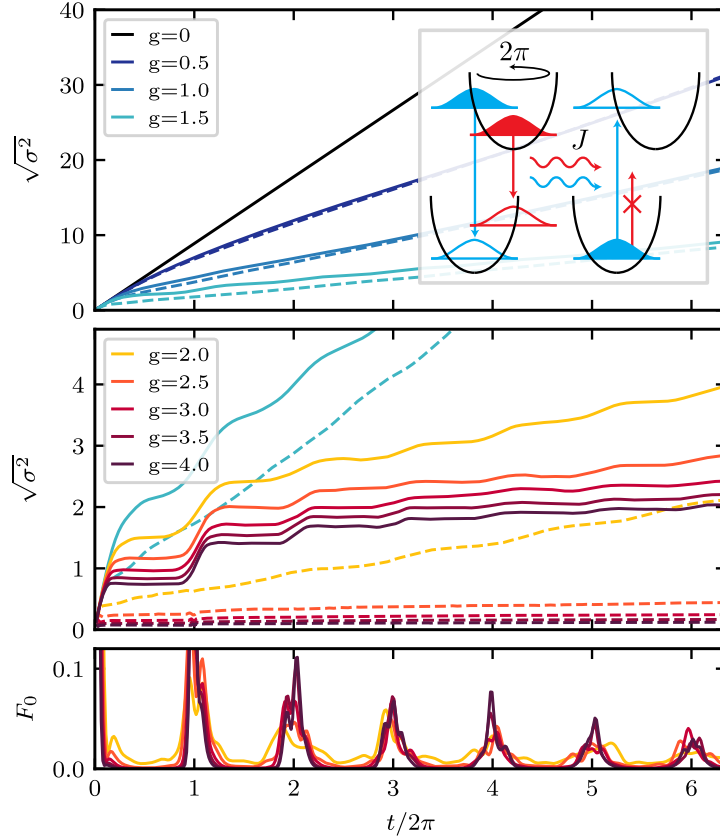
Figure 4.2:   Upper panels: RMSD against time for Franck-Condon (solid lines) and relaxed
(dashed lines) excitations. The inset shows a schematic of the vibrationally-induced transfer
mechanism for Franck-Condon excitations. Data for $g = 1.5$ is reproduced in both panels for
comparison. Lower panel: Overlap F_0 between the vibrational wavepacket in the electron-
ically excited potential and that of the zero-vibrational state in the ground state potential
for the central site.
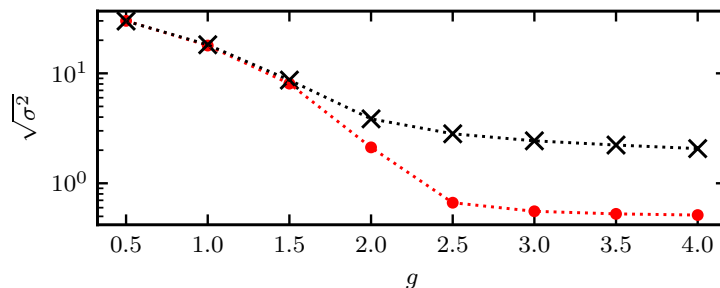
Figure 4.3: RMSD at time $t/2\pi = 6$ as a function of the vibronic coupling strength for Franck-Condon (black crosses) and relaxed (red dots) excitations.

excitations in the strong coupling limit. In order to understand the nature of this mechanism it is insightful to consider the transient overlap of the vibrational wavefunction inside the electronically excited potential with that of the zero-vibrational state in the ground state potential. Shown together with the RMSDs in Fig. 7.2, this overlap exhibits a beating pattern roughly in sync with that seen for excitation transport, such that regions of large vibrational overlap coincide with abrupt enhancements in the RMSD.

The physical picture of the dynamics of strongly-coupled Franck-Condon excitations emerging from our results is shown schematically in the inset of Fig. 7.2. Upon initial excitation, the vibrational wavepacket oscillates in and out of the Franck-Condon region, as indicated by the beatings apparent in the calculated vibrational overlap. When inside this region, excitation transfer to neighboring sites is effective due to a resonance between the (inverted) Franck-Condon transition at the donor site and that at the neighboring site. Moving out of this region, however, the transition energy at the donor site will rapidly decrease, leaving the vibrationally-relaxed neighboring site without an energy-matching transition with significant vibrational overlap. Importantly, the sustained motion of the strongly-coupled vibration protects the electronic excitation from self-localizing while periodic resonant transfers occur.
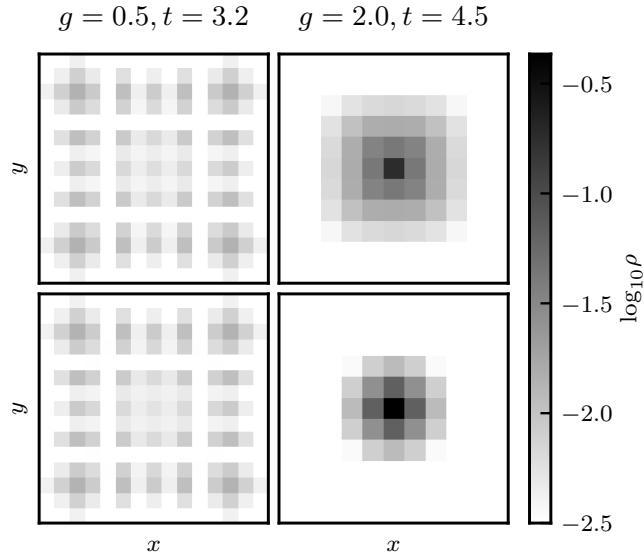
Figure 4.4: Excitation density ρ for two-dimensional lattices at weak ($g = 0.5$, 15×15 sites, left panel) and strong coupling ($g = 2.0$, 11×11 sites, right panel). Upper (lower) panels show Franck-Condon (relaxed) excations. Log scale is used for clarity.

Next, we briefly discuss the manifestation of the dynamics in two dimensions. Higher-dimensional tensor network structures are computationally demanding, while mapping higher-dimensional problems to a one-dimensional tensor network induces long-range connectivity, resulting in complicated entanglement structures. This renders the application of tensor network states in two dimensions and above a challenging endeavor, particularly so for dynamical problems involving strongly-correlated electronic systems for which the time scales reached in state-of-the-art calculations have been limited [35]. Interestingly, for the two-dimensional Holstein model mapped to a chain in a row-by-row manner (from left to right and from bottom to top), again with $\omega_0 = J = 1$, we are able to reach time scales ($t/J \sim \pi$) comparable to earlier efforts with modest computational resources. Although a detailed investigation of the performance of our method in higher dimensions is beyond the scope of the present Letter, we speculate that the principle that entanglement is introduced in-

directly (by coupling between different sets) aids in obtaining a favorable computational performance even in two dimensions. In Fig. 4.4, we show the excitation densities for select reorganization energies and excitation conditions, given a square lattice with open boundary conditions and an excitation initiated at the center. For weak coupling, both the relaxed and Franck-Condon excitation are equally spread-out, exhibiting a well-resolved two-dimensional interference pattern. Consistent with the one-dimensional case, with increasing g we find the spread of the Franck-Condon excitation to be significantly more pronounced than that of the relaxed excitation.

4.4 Discussion

We have shown that mixing of electronic coordinates with strongly-coupled vibrational modes results in Franck-Condon excitations whose initial dynamics is markedly different from that known for vibrationally-relaxed excitations. Sustained vibrational motion is found to generate periodic resonances between neighboring electronic sites, during which effective energy transfer occurs, allowing a Franck-Condon excitation to spread over substantial distances in parameter regimes where relaxed excitations are essentially self-trapped on a single site. Of course, over much longer time scales one expects that this mechanism no longer governs the dynamics, and behavior akin to that of the relaxed initial condition takes over. In addition to providing fundamental insights into strongly-coupled vibronic systems, these results have implications for the nonequilibrium behavior of materials upon vertical transitions from a vibrationally-relaxed (ground state) initial condition, in particular when the functionally-relevant dimensions of the material are in the range of the mean square displacements found in our calculations. In many practical cases excitation conditions are near-vertical, resulting

from impulsive perturbations of the electronic degrees of freedom, and our findings reveal that the subsequent ultra-fast dynamics can not be understood based on vibrationally-relaxed steady-state principles. In unraveling this remarkable photophysical behavior, we have accessed a notoriously difficult region of the single-particle Holstein model, employing the computational benefits offered by a multi-set matrix product state approach. As such, this work highlights the potential of this tensor network state method in addressing problems involving charged and excitonic polarons. The flexibility of this approach also allows to make progress in more complex situations, such as long-range electronic hopping or higher dimensionality, for which encouraging results have been presented in this work. Lastly, given that ground states of gapped, one-dimensional systems follow the area law of entanglement entropy, we expect this approach to also perform well for finding ground and low-lying excited states within the one-dimensional single-particle Holstein model.

4.5 Explicit form of the projector onto tangent space

We obtain dynamics within the variational manifold of sets of matrix-product states (MPSs) with a given bond dimension via the time-dependent variational principle, which amounts to solving the tangent-space projected Schrödinger equation

$$i|\dot{\Psi}\rangle = \hat{\mathcal{P}}_{\mathcal{M}}[|\Psi\rangle]\hat{H}\,|\Psi\rangle\,. \tag{4.5}$$

For completeness we will give the explicit, closed form of the tangent space projector employed in this work. To this end, it is first necessary to introduce the mixed-canonical form of MPSs. MPSs are unique up to unitary transformations of the site tensors, $\tilde{A}_i^{\sigma_i} = G_{i-1}^{-1} A_i^{\sigma_i} G_i$. This allows one to define a *gauge* with a center of orthogonality at a given site j, i.e., all

tensors to the left and right of site j contract with their complex conjugate to the identity matrix I of dimension $\chi_{i-1} \times \chi_{i-1}$ or $\chi_i \times \chi_i$:

$$|\Psi\rangle = \sum_{\{\sigma_i\}} L_1^{\sigma_1} \dots L_{j-1}^{\sigma_{j-1}} A_j^{\sigma_j} R_{j+1}^{\sigma_{j+1}} \dots R_N^{\sigma_N} |\sigma_1 \sigma_2 \dots \sigma_N\rangle, \tag{4.6}$$

with $\sum_{\sigma_i} L_i^{\sigma_i \dagger} L_i^{\sigma_i} = I$ and $\sum_{\sigma_i} R_i^{\sigma_i} R_i^{\sigma_i \dagger} = I$, respectively. In the following, we will use the shorthand notation

$$|L_j\rangle = \sum_{\{\sigma_i\}|i<j} L_1^{\sigma_1} \dots L_{j-1}^{\sigma_{j-1}} |\sigma_1 \dots \sigma_{j-1}\rangle \tag{4.7}$$

and

$$|R_j\rangle = \sum_{\{\sigma_i\}|i>j} R_{j+1}^{\sigma_{j+1}} \dots R_N^{\sigma_N} |\sigma_{j+1} \dots \sigma_N\rangle. \tag{4.8}$$

$|L_j\rangle$ ($|R_j\rangle$) can be thought of as representing a truncated orthonormal basis in an MPS format for the physical degrees of freedom to the left (right) of site j, i.e., $\langle L_j|L_j| =\rangle I$ ($\langle R_j|R_j| =\rangle I$). Defining $|A_j\rangle = \sum_{\sigma_j} A_j^{\sigma_j} |\sigma_j\rangle$, the wavefunction can now be written compactly as $|\Psi\rangle = |L_j\rangle |A_j\rangle |R_j\rangle$, for which the center of orthogonality is located at site j. Alternatively, we can write $|\Psi\rangle = |L_{j+1}\rangle C_j^{\sigma_j} |R_j\rangle$ with the center of orthogonality between sites j and $j+1$, where C_j is a matrix. For future reference, we also define the third-order tensor A_j, a slice of which along the physical index σ_j is given by $A_j^{\sigma_j}$, and its equivalents in left or right orthonormal gauge, L_j and R_j. For multi-set MPSs, a superscript α is introduced to denote the MPS associated with electronic state $|\alpha\rangle$. The tangent space projector for the multi-set MPS ansatz can be decomposed into orthogonal contributions:

$$\hat{\mathcal{P}}_\mathcal{M}[|\Psi\rangle] = \sum_{j=1}^{N-1} \left(\hat{\mathcal{P}}_j^+ - \hat{\mathcal{P}}_j^- \right) + \hat{\mathcal{P}}_N^+, \tag{4.9}$$

where

$$\hat{\mathcal{P}}_j^+ = \sum_\alpha \hat{\mathcal{P}}_j^{+,\alpha} = \sum_\alpha \left| L_j^\alpha \right\rangle \left\langle L_j^\alpha \right| \otimes \hat{I}_j \otimes \left| R_j^\alpha \right\rangle \left\langle R_j^\alpha \right| \otimes \left| \alpha \right\rangle \left\langle \alpha \right|, \tag{4.10}$$

with $\hat{I}_j = \sum_{\sigma_j} \left| \sigma_j \right\rangle \left\langle \sigma_j \right|$ being the identity operator for the physical degree of freedom at site j, and

$$\hat{\mathcal{P}}_j^- = \sum_\alpha \hat{\mathcal{P}}_j^{-,\alpha} = \sum_\alpha \left| L_{j+1}^\alpha \right\rangle \left\langle L_{j+1}^\alpha \right| \otimes \left| R_j^\alpha \right\rangle \left\langle R_j^\alpha \right| \otimes \left| \alpha \right\rangle \left\langle \alpha \right|. \tag{4.11}$$

4.6 Equations of motion

Each of the tangent space projectors generates one of the equations of motion to be solved. For example, for $\hat{\mathcal{P}}_j^{+,\alpha}$ we obtain

$$\hat{\mathcal{P}}_j^{+,\alpha} \hat{H} \left| \Psi \right\rangle = \left| L_j^\alpha \right\rangle \left(\left\langle R_j^\alpha \right| \left\langle L_j^\alpha \right| \sum_\beta \hat{H}^{\alpha\beta} \left| L_j^\beta \right\rangle \left| A_j^\beta \right\rangle \left| R_j^\beta \right\rangle \right) \left| R_j^\alpha \right\rangle \left| \alpha \right\rangle, \tag{4.12}$$

where $\hat{H}^{\alpha\beta} = \left\langle \alpha \right| \hat{H} \left| \beta \right\rangle$. Thus, the right-hand side of Eq. 4.12 takes the form $\left| L_j^\alpha \right\rangle \left(i \left| \dot{A}_j^\alpha(t) \right\rangle \right) \left| R_j^\alpha \right\rangle \left| \alpha \right\rangle$, consistent with the time variations in parts of the wavefunction other than $\left| A_j^\alpha(t) \right\rangle$ being projected out by the tangent space projector, with $i \left| \dot{A}_j^\alpha(t) \right\rangle$ given by

$$i \left| \dot{A}_j^\alpha(t) \right\rangle = \left\langle R_j^\alpha \right| \left\langle L_j^\alpha \right| \sum_\beta \hat{H}^{\alpha\beta} \left| L_j^\beta \right\rangle \left| A_j^\beta(t) \right\rangle \left| R_j^\beta \right\rangle. \tag{4.13}$$

Similarly, $i\dot{C}_j^\alpha(t)$ is generated by $\hat{\mathcal{P}}_j^{-,\alpha}$,

$$i\dot{C}_j^\alpha(t) = \left\langle R_j^\alpha \right| \left\langle L_{j+1}^\alpha \right| \sum_\beta \hat{H}^{\alpha\beta} \left| L_{j+1}^\beta \right\rangle C_j^\beta(t) \left| R_j^\beta \right\rangle. \tag{4.14}$$

These equations of motion are identical to those given in Ref. 22, except for the appearance of the label for the electronic state α and summations thereover. Consequently, we apply the same linearization of Eq. 4.5 along the physical sites j as in Ref. 22. Note that for a given site j the equations of motion for tensors of different electronic states α are coupled. We thus choose to simultaneously solve the equations of motion for all electronic states at site j, i.e., as one large uncoupled linear differential equation. The resulting scheme outlined in Algorithm 4.1 updates A_j^α and C_j^α alternately, sweeping forward and backward through the lattice, and using matrix decompositions, specifically the QR decomposition, and multiplications to move the center of orthogonality accordingly. For an introduction to the application of matrix decompositions and multiplications to the third-order tensors, which is obtained via 'unfolding' or reshaping the tensor into a matrix, we refer to Refs. 22 and 119.

Algorithm 4.1 Symmetric second-order integrator for the time-dependent variational principle applied to multi-set matrix product states. Each line is executed for each electronic state ($\forall \alpha$), with the exception of the **for** loops.

Input: $|\Psi^\alpha(t)\rangle$ in right-orthogonal form $\forall \alpha$

1: $\bar{A}_1^\alpha \leftarrow R_1^\alpha = A_1^\alpha$
2: **for** $j = 1 \ldots N-1$ **do**
3: $\quad \bar{\bar{A}}_j^\alpha \leftarrow$ solve Eq. 4.13 from $t \to t + \frac{\Delta t}{2}$ with $A_j^\alpha(t) = \bar{A}_j^\alpha$
4: $\quad$ obtain $L_j^\alpha(t + \frac{\Delta t}{2})$ and $\bar{C}_j^\alpha$ from QR decomposition of $\bar{\bar{A}}_j^\alpha$ unfolded along its right virtual index
5: $\quad \bar{\bar{C}}_j^\alpha \leftarrow$ solve Eq. 4.14 from $t + \frac{\Delta t}{2} \to t$ with $C_j^\alpha(t + \frac{\Delta t}{2}) = \bar{C}_j^\alpha$
6: $\quad \bar{A}_{j+1}^\alpha = \bar{\bar{C}}_j^\alpha R_{j+1}^\alpha(t)$
7: **end for**
8: $\bar{\bar{A}}_N^\alpha \leftarrow$ solve Eq. 4.13 from $t \to t + \Delta t$ with $A_N^\alpha(t) = \bar{A}_N^\alpha$
9: **for** $j = N-1 \ldots 1$ **do**
10: $\quad$ obtain $\bar{C}_j^\alpha$ and $R_{j+1}^\alpha(t + \Delta t)$ from QR decomposition of $\bar{\bar{A}}_{j+1}^\alpha$ unfolded along its left virtual index
11: $\quad \bar{\bar{C}}_j^\alpha \leftarrow$ solve Eq. 4.14 from $t + \Delta t \to t + \frac{\Delta t}{2}$ with $C_j^\alpha(t + \Delta t) = \bar{C}_j^\alpha$
12: $\quad \bar{A}_j^\alpha = L_j^\alpha(t + \frac{\Delta t}{2})\bar{\bar{C}}_j^\alpha$
13: $\quad \bar{\bar{A}}_j^\alpha \leftarrow$ solve Eq. 4.13 from $t + \frac{\Delta t}{2} \to t + \Delta t$ with $A_j^\alpha(t + \frac{\Delta t}{2}) = \bar{A}_j^\alpha$
14: **end for**

Output: $|\Psi^\alpha(t + \Delta t)\rangle$ in right-orthogonal form $\forall \alpha$

4.7 Convergence

Below we provide proof of convergence and exactness of the multi-set MPS approach. Furthermore, we compare the convergence behavior of the multi-set MPS method with that of the more conventional approach of using an MPS for the Jordan-Wigner transformed Holstein model, henceforth referred to as standard MPS. The comparison with exact diagonalization in Fig. 4.5 establishes both exactness of the method at short times and at exact bond dimension, as well as the appropriateness of the chosen timestep for a 5-site Holstein model. For the system sizes presented in the main text, such a comparison is not feasible and we instead report in Fig. 4.6 the maximum relative deviation of the root mean square dis-
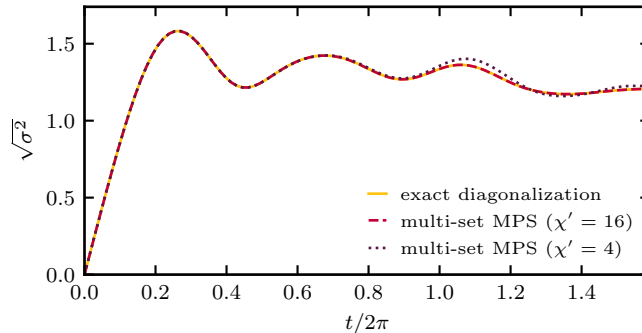
Figure 4.5: Root mean square displacement of the electronic wavepacket as a function of time, computed with exact diagonalization (solid yellow line) and multi-set MPS at exact (red dashed line) and approximate (black dotted line) bond dimensions for a 5-site Holstein model. $g = 1.0$, $\nu_{\max} = 4$, $dt = 0.1$.

placement (RMSD) with respect to a reference calculation with twice as large a local Hilbert space dimension, $\nu_{\max}$, or bond dimension, χ'. In all cases, only the numerical parameter with respect to which the deviation is evaluated is varied, while other parameters are kept fixed at the values reported in Table I in the main text. To explore the relative performance of the multi-set MPS approach compared to a standard MPS approach (the local Hilbert space corresponding to a direct product of electronic and vibrational local Hilbert spaces), we plot the relative deviation of the RMSD obtained at various bond dimensions with respect to a reference calculation in Fig. 4.7. The results for the standard MPS are obtained with tenpy [120], using the time-dependent variational principle in its two-site formulation [22] and making use of conserved quantities (the number of electronic particles). Timings for these calculations are reported in Table 4.2. The two-site algorithm for the standard MPS, used for technical reasons, results in a somewhat worse scaling with the local Hilbert space dimension than the single-site algorithm used in our multi-set approach. Thus, the timings should only be considered as rough estimates of the computational effort and not as a thorough performance comparison between the two methods.
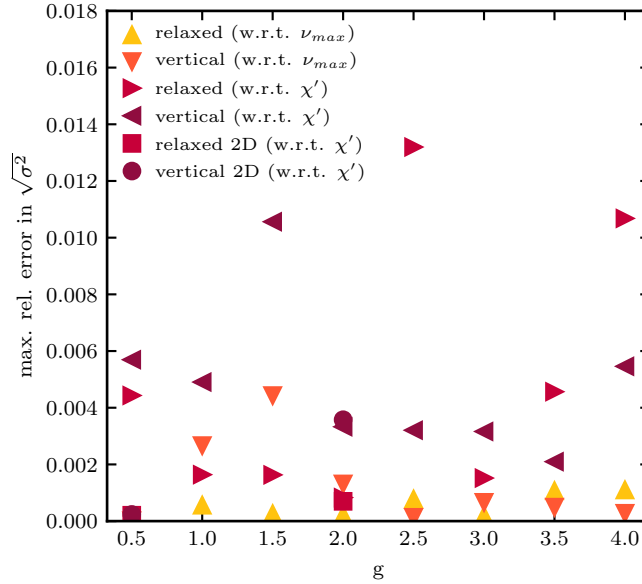
Figure 4.6: Maximum relative deviation of the root mean square displacement with respect to a doubling of different numerical parameters at various vibronic coupling strengths, g. Note that for $g = 3.5$ and $g = 4.0$, the deviation with respect to $\nu_{\max}$ is obtained at $\chi' = 16$.
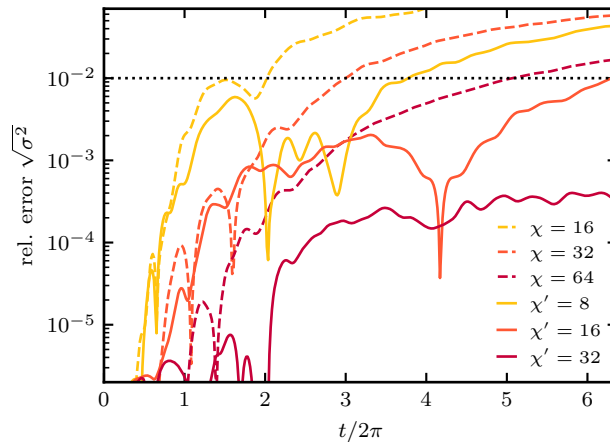
Figure 4.7: Maximum relative deviation of the root mean square displacement with respect to a doubling of the bond dimension for a vertical excitation at $g = 1.5$ in the multi-set MPS approach (solid lines; reference calculation with $\chi' = 64$) and in the standard MPS approach (dashed lines; reference calculation with $\chi = 128$). The convergence threshold of 1% is indicated by the black dotted line. All other model and numerical parameters are the same as in the caption of Table 4.2.

4.8 Computational effort

The multi-set MPS algorithm scales quadratically with the system size and linearly with the local Hilbert space dimension in both computation and storage. To leading order, the scaling of computation and storage with bond dimension is cubic and quadratic, respectively. It thus has the same formal scaling as other MPS-based time evolution approaches, with the exception of the quadratic scaling with system size. The latter is inherent in the multi-set nature of the approach, and can be remedied by parallelization up to a factor of the system size, such that the walltime and memory requirement per core or CPU again scales linearly with system size. To provide an estimate of the computational effort of the method, Table 4.3 shows execution times and memory requirements for a select number of calculations on which the data in the main text is based. A lower bound of the required memory can be calculated straightforwardly from the number of variational parameters in the multi-set MPS wavefunction, which are complex numbers in double precision, up to a prefactor of $\mathcal{O}(1)$ for storing partial contractions of the Hamiltonian and other implementation-dependent memory overhead.

MPS format	$\chi^{(\prime)}$	$t_{\max}$	#processes (proc.)	walltime [h]
multi-set	8	50	1	12.0
	16	50	1	17.1
	16	50	15	3.3
	32	50	1	54.3
	32	50	15	11.7
standard	16	50	1	16.4
	32	50	1	26.5
	64	50	1	44.3
	128	50	1	149.9

Table 4.2: Code execution times for simulations up to time $t_{\max}$ on a local cluster with two Xeon E5-2690 v3 @ 2.60GHz with Hyperthreading per node. Calculation parameters are $g = 1.5$, $N = 75$, $\nu_{\max} = 16$, $dt = 0.1$, and a discarded weight of $\epsilon = 10^{-8}$ for the standard MPS approach. As shown in Fig. 4.7, the standard approach with a bond-dimension of $\chi = 64$ achieves a comparable accuracy to the multi-set approach with a bond-dimension of $\chi' = 16$.

g	N	χ'	$\nu_{\max}$	dt	$t_{\max}$	#proc.	walltime [h]	mem. / proc.	mem. for Ψ
4.0	25	32	128	0.1	40	1	156.0	4.3 GB	1.2 GB
0.5	301	32	8	0.1	50	43	38.4	1.1 GB	11.7 GB

Table 4.3: Code execution times and memory requirements for simulations up to time $t_{\max}$ on a local cluster with two Xeon E5-2690 v3 @ 2.60GHz with Hyperthreading per node. The memory requirements are given in the second-to-last and last column as the memory per process required by the calculation and the memory required to store a single copy of the wavefunction, respectively.

Chapter 5

Time-dependent variational principle in matrix-product state manifolds: pitfalls and potential

This chapter was published as: B. Kloss et al., Phys. Rev. B **97**, 024307 (2018)

5.1   Introduction

The numerically exact simulation of the dynamics of strongly interacting quantum systems is a grand challenge in condensed matter science. For ground states of gapped one-dimensional systems with short-range interactions, the density matrix renormalization group (DMRG) proves to be a powerful and efficient approach [13, 14]. Its success is linked to the fact that the ground states of these systems are optimally representable by matrix product states (MPS), with a moderate number of variational parameters, normally referred to as the bond dimension. While DMRG has been extended into the time-domain, the timescales that may

be reached are usually quite short as a consequence of correlations that develop within the propagated wavefunction [13, 14]. Time evolution tends to quickly displace states from the space efficiently representable by MPS, leading to a rapid (typically exponential) growth of the bond dimension. If the bond dimension of the wavefunction is not dynamically adjusted to accommodate the growing correlations in the wavefunction the dynamics quickly becomes approximate and nonunitary. It is possible to construct a unitary time-propagation scheme on the manifold of MPS with a fixed bond dimension using the Dirac-Frenkel time-dependent variational principle (TDVP) [21, 22, 55, 56]. This principle, which is rather generic, projects an infinitesimal time evolution under the Hamiltonian to a variational manifold which the resulting wavefunction is restricted to occupy. An advantage over conventional DMRG techniques is that the TDVP can be applied to a more general class of states, such as tree tensor network states, thus potentially opening the door to efficiently simulating higher dimensional systems as well as systems with long-ranged interactions.

The description of transport properties requires the investigation of large system sizes and long times, a limit which is sometimes referred to as the hydrodynamic limit. While this limit appears to be out of reach for numerically exact methods, an approximate coarse-grained treatment might be sufficient to obtain accurate macroscopic observables like transport coefficients, analogous to the success of classical hydrodynamics. In this respect the TDVP is particularly attractive, since it generates effectively chaotic classical dynamics in the space of variational parameters which obey a set of macroscopic conservation laws, such as those associated with the total number of particles and the total energy [121]. Indeed, a surprisingly fast convergence of the heat diffusion constant with respect to bond dimension has been very recently reported for a nonintegrable spin chain [60].

In this work, we examine the applicability of TDVP for the long time description of

quantum interacting systems. While the method cannot be expected to work for quantum integrable systems (c.f. generalization of hydrodynamic approaches to such systems [122]), by utilizing the exact solvability of such systems we show that the long time limit, which is necessary to obtain hydrodynamic observables, and the large bond-dimension limit, where the method becomes numerically exact, do *not* generically "commute." In particular, the apparent convergence of hydrodynamic observables with the bond dimension does *not* guarantee the accuracy of the result, which has to be established by other means. This problem persists also for nonintegrable systems, although for the case of a disordered *nonintegrable* quantum system that we consider, this problem appears to be ameliorated.

5.2   Theory

The Hilbert-space dimension of a quantum lattice systems scales exponentially with the size of the system. Any wavefunction in the Hilbert space can be written as a matrix product state (MPS),

$$|\Psi[A]\rangle = \sum_{\{s_n\}=1}^{d} A^{s_1}(1)A^{s_2}(2)\dots A^{s_N}(N)\,|s_1 s_2 \dots s_N\rangle \tag{5.1}$$

where d is the local Hilbert space dimension, $A^{s_i}(i) \in \mathbb{C}^{D_{i-1}\times D_i}$ are complex matrices and $D_0 = D_N = 1$, such that the product of matrices evaluates to a scalar coefficient for a given configuration $|s_1 s_2 \dots s_n\rangle$. To be an *exact* representation of the wavefunction the dimension of the matrices the bond dimension must scale exponentially with the systems size. Typically one approximates the wavefunction by truncating the dimension of the matrices to a predetermined dimension with computationally tractable number of parameters. Exact results are obtained when the approximate dynamics are converged with respect to the bond

dimension.

The time-dependent variational principle (TDVP) allows one to obtain a locally optimal (in time) evolution of the wavefunction on the manifold of MPS, $\mathcal{M}_{\mathbf{r}}$, with some fixed bond dimension $\mathbf{r}$. It amounts to solving a tangent-space projected Schrödinger equation [22]:

$$\frac{d\,|\Psi[A]\rangle}{dt} = -\mathrm{i}P_{\mathcal{M}}\hat{H}\,|\Psi[A]\rangle, \tag{5.2}$$

where $P_{\mathcal{M}}$ is the tangent space projector to the manifold $\mathcal{M}_{\mathbf{r}}$. Equation (6.5) is solved using a Trotter-Suzuki decomposition of the projector(see Ref. [22] for details).

The dynamics generated by the TDVP can be viewed as resulting from a classical, non-quadratic Lagrangian in the space of variational parameters [21, 60]. It can be shown that any conserved quantity of the Hamiltonian will be also conserved by TDVP if the corresponding symmetry group members of the associated quantity applied to a state in the manifold $\mathcal{M}_{\mathbf{r}}$ do not take it out of the manifold [121]. The nonlinearity of the equations of motion of TDVP disappears in the limit of infinite bond dimension, since in this limit the action of the Hamiltonian on the state keeps it on the manifold for all times.

5.3 Results

We study transport properties of the one-dimensional XXZ model,

$$\hat{H} = J_{xy}\sum_{i=1}^{N-1}\left(\hat{S}_i^x\hat{S}_{i+1}^x + \hat{S}_i^y\hat{S}_{i+1}^y\right) + \Delta\sum_i\hat{S}_i^z\hat{S}_{i+1}^z + \sum_{i=1}^{N}h_i\hat{S}_i^z, \tag{5.3}$$

where h_i is uniformly distributed in the interval $[-W, W]$ and $\hat{S}_i^{(x,y,z)}$ are the appropriate projections of the spin operators on site i. In the following, we use $J_{xy} = 1$, which sets

the time unit of the problem. Using the Jordan-Wigner transformation the XXZ model can be mapped to a model of spinless fermions [123]. For $\Delta = 0$, the corresponding model is noninteracting and can be solved exactly. In particular for $W \neq 0$ the system becomes Anderson localized [124]. For $\Delta \neq 0$ and at sufficiently high disorder the system becomes many-body localized and exhibits a dynamical phase transition [6, 7] which, for $\Delta = 1$, occurs at $W \approx 3.5$ [125, 126].

To study the dynamical properties of this model in its various limits we calculate the spreading of a spin-excitation as a function of time,

$$\sigma^2(t) = \sum_{i=1}^{L} (\frac{L}{2} - i)^2 \left\langle \hat{S}_i^z(t) \hat{S}_{L/2}^z(0) \right\rangle. \tag{5.4}$$

Here the expectation value is calculated at infinite temperature, namely $\left\langle \hat{O} \right\rangle = \text{Tr}\,\hat{O}/\mathcal{N}$ where $\mathcal{N}$ is the Hilbert space dimension. The spread of the excitation is analogous to the classical mean-square displacement (MSD). Transport is characterized by assuming a power law scaling of the MSD, $\sigma^2(t) \sim t^\alpha$. For example, a dynamical exponent of $\alpha = 2$ ($\alpha = 1$) indicates ballistic (diffusive) transport. A dynamical exponent $0 < \alpha < 1$ corresponds to subdiffusive transport, and $\alpha = 0$ for localized systems. We also define a time-dependent diffusion constant $D(t)$ as the time-derivative of $\sigma^2(t)$ [127–130]. Throughout this work the hydrodynamic variable that we will consider will be the asymptotic spin diffusion coefficient, $\lim_{t \to \infty} D(t) \to D$.

To calculate the MSD we numerically evaluate the correlation function starting from a random configuration of up and down spins and also a random configuration of the disordered field, when appropriate. By sampling simultaneously both spin configurations and disorder configurations we obtain the required infinite temperature initial conditions and disorder

average. The size of the system is chosen to be $L = 100 - 200$, such that all finite size effects are negligible on the simulated time scales, and the averages are obtained using at least 100 realizations.

The integration time-step is chosen such that no qualitative influence on the MSD is observed. For the models studied in this work time-steps of $0.05 - 0.2$ were found to satisfy this criterion. Because of the nonlinearity introduced in Eq. (6.5) due to $P_{\mathcal{M}}$, chaos emerges on a time-scale, dubbed the Lyapunov time, which depends both on the bond-dimension, the realization studied, and the parameters of the system. Beyond this time, it becomes exponentially expensive (in time) to obtain convergence of the results on the level of *individual* configurations. We note in passing, that the Lyapunov time becomes longer for larger bond dimension [60].

To assess the convergence of the method, for each configuration determined by the initial configuration of the spins and the disorder configuration, we calculate the convergence time, $t_*(\omega)$ (here ω designates the configuration). For times $t < t_*(\omega)$ the dynamics generated starting from a given configuration is converged within a required accuracy (2%) by increasing the bond dimension. For the infinite temperature initial condition we use in this work, the convergence time, t_*, is calculated by averaging $t_*(\omega)$. It is crucial to consider *individual* configurations to assess the numerical convergence of the method since averaging over realizations introduces a fortuitous cancellation of errors, thus while t_* demarcates a strict, well-defined convergence metric, apparent convergence of either transport coefficients or dynamics may occur *after* this time. The averaged convergence times for which TDVP is numerically exact are comparable to convergence times of conventional DMRG or MPS techniques.

We first demonstrate that the long time limit essential for the study of hydrodynam-
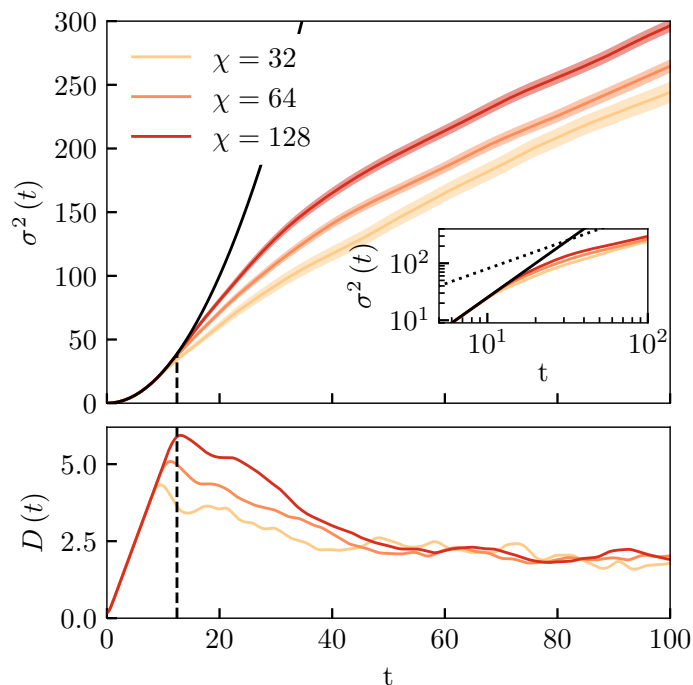
Figure 5.1: Clean XX model ($\Delta = 0$, $W = 0$). Upper panel: MSD as a function of time for various bond dimensions (32, 64, 128) averaged over 200-500 realizations of initial spin configurations and disorder. More intense shades represent larger bond dimensions and shaded areas indicate the standard-deviation of the observables obtained using a bootstrap procedure. The black solid line is an exact solution, obtained numerically. The inset shows the log-log scale of the main panel with the black dotted corresponding to diffusion. Lower panel: Time-dependent diffusion constant $D(t)$. The dashed black line on both plots represents the convergence time, t_*.
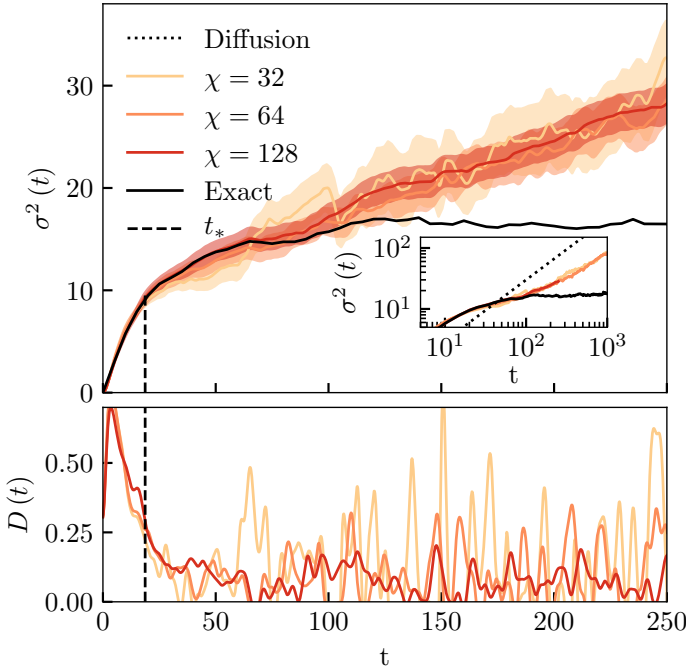
Figure 5.2: Same as Fig. (5.1) but for the disordered XX model ($\Delta = 0$, $W = 1$) for 100 realizations of initial spin configurations and disorder.
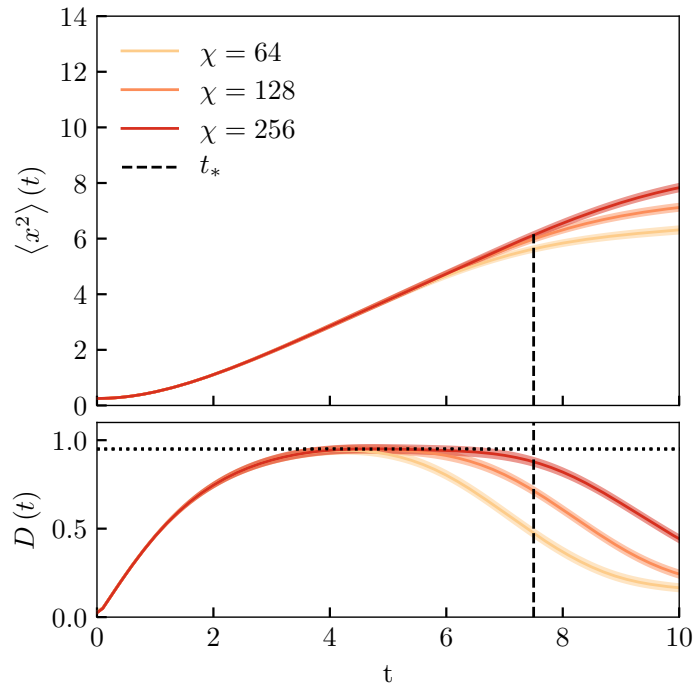
Figure 5.3: Same as Fig. (5.1) but for clean XX ladder of length $L = 50$ with isotropic coupling between the rungs. The results were obtained by averaging 100 realizations of initial spin configurations. The black dotted line in the bottom panel represents the previously reported diffusion constant [131].
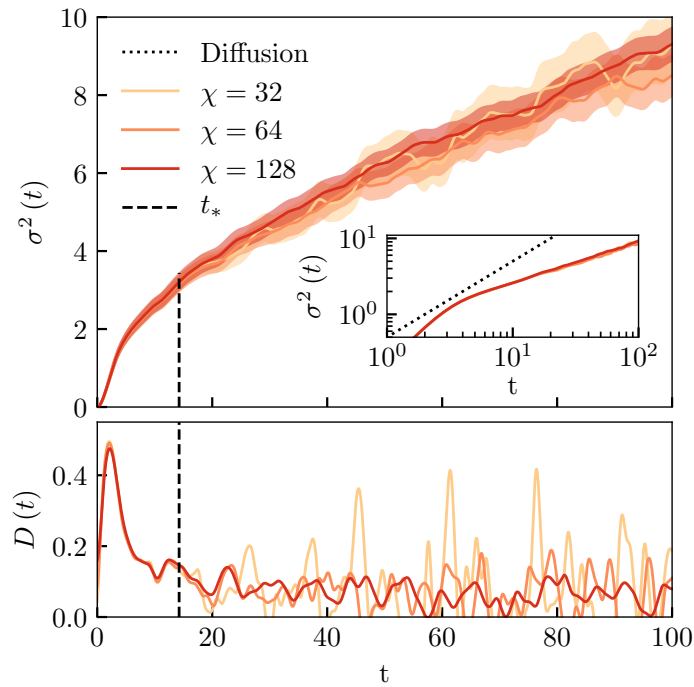
Figure 5.4: Same as Fig. (5.1) but for disordered XXZ model in the subdiffusive regime ($\Delta = 1$, $W = 1.5$) for 200 realizations of initial spin configurations and disorder.

ics properties and the large bond-dimension limit, when the method becomes exact, do not "commute," in the sense that spurious, apparently converged long time behavior may emerge. For this purpose we will first consider two integrable models with a known dynamical behavior. We stress that true hydrodynamic behavior (at least in the usual sense) is *not* expected for such models.

Ballistic regime ($\Delta = 0$, $W = 0$, $L = 200$). The expected ballistic transport is accurately reproduced only up to $t_* \simeq 12$ for the largest bond-dimension employed (see Fig. 5.1). While this system corresponds to free fermions, the entanglement still grows limiting the accessible times. Beyond the convergence time transport appears to be diffusive with a diffusion constant of approximately 2.0. There is little variation of this value across the different bond-dimensions.

Anderson localized regime ($\Delta = 0$, $W = 1$, $L = 150$). This system is also effectively noninteracting with a MSD which saturates in time, indicating localization. TDVP fails to reproduce the plateau for all studied bond dimensions and displays growth of the MSD with time although the diffusion coefficient is rather small (see Fig. 5.2). Results obtained using the largest bond-dimension (128) follow the exact result closely up to about $t = 70$, while those of smaller bond-dimensions deviate significantly earlier, resulting in $t_* = 19$.

Since asymptotically the nonlinear equations of TDVP are expected to result in diffusion, the striking failure of the method for the two integrable systems above is not surprising.

Diffusive XX-ladder ($\Delta = 0$, $L = 50$). This model is a generalization of (5.3) to a two leg ladder. It is nonintegrable and shows convincing diffusion with a diffusion coefficient of about $D \sim 0.95$ [131, 132]. As expected for short times the calculations based on the TDVP

reproduce this numerically exact results (see Fig. 5.3) However, for times longer than the convergence time, $t > t_* = 8$, a crossover to yet another diffusive regime with much lower diffusion constant appears ($D \sim 0.2$). Moreover this diffusion coefficient does not appear to strongly depend on the bond-dimension.

The above examples illustrate that the seemingly converged transport coefficients and long time dynamics within the TDVP framework can be highly misleading. After demonstrating the pitfalls in determining the long-time properties using TDVP, we examine its potential as a hydrodynamic method for a disordered nonintegrable system.

Subdiffusive regime ($\Delta = 1.0$, $W = 1.5$, $L = 100$).   For moderate disorder $0 < W < 3.7$ the system is nonintegrable [130]. While the convergence time here is about $t_* = 18$, semi-quantatively similar subdiffusive transport appears also at much longer times (see inset in Fig. 5.4). Interestingly, the exponent extracted from the long-time behavior, $\alpha = 0.54$, is in excellent agreement with previously reported value, extracted from the short time dynamics of the same system using exact diagonalization [130, 133–135]. This indicates that for such a system, true asymptotic dynamical behavior may indeed be uncovered using moderate numerical costs (small bond-dimensions).

5.4   Discussion

In this work we have examined how well TDVP captures the *long time* behavior of quantum interacting systems. For any *finite* time the method is formally numerically exact, since it can be converged with respect to the bond dimension and other numerical parameters. For longer times convergence cannot be guaranteed generically, but one hopes that *on average* the method will still produce the correct result, due to ergodicity of the TDVP trajectories

on the MPS manifold. This assumes that the MPS ansatz captures all the relevant local correlations that produce long time behavior.

By examining integrable and nonintegrable models for which the asymptotic dynamics in known, we have shown that the apparent convergence of long time observables, such as the diffusion coefficient, obtained using TDVP is *not* indicative of the accuracy of the method and may be very misleading. While the dramatic failure of TDVP to reproduce ballistic and localized dynamics is expected, it is quite unfortunate that the method appears to fail also for a nonintegrable diffusive model.

Interestingly, the most promising results are obtained for the nonintegrable *disordered* XXZ model in the ergodic subdiffusive phase [130], which is the only presented example where the short time and long time behavior appear to agree very well, although the same caveats concerning convergence apply. This is quite surprising, in light of the expectation of asymptotic diffusion in TDVP generated dynamics due to the underlying nonlinearity of the equations of motion. Nevertheless, we find that the MSD calculated by TDVP is strongly sublinear, although we cannot rule out a slow approach of the dynamical exponent to its diffusive value. We would like to point out a possible connection between the nonlinearity introduced by the tangent space projector into the TDVP equations of motion and the nonlinear dependence on the wave function in the self-consistent second Born approximation, [6, 136, 137] and the nonlinear Schrödinger equation (NLSE), both of which also show subdiffusive transport in the presence of disorder [138].

In summary, we have shown that great care must be exercised examining the apparent convergence of long time properties within the TDVP approach, which appears to generically produce either qualitatively or quantitatively incorrect results. Nevertheless, we have presented one nontrivial system were the short time (numerically exact) dynamics and the

long time dynamics agree, and therefore hint at the possibility of an accurate asymptotic description, obtained at a modest computational effort. It is of great importance to further investigate the origins of the apparent success of the method in this case as well as to extend this study to other nonintegrable systems in one and two-dimensions.

Chapter 6

Spin transport in long-range interacting spin chain

This chapter was published as: B. Kloss and Y. Bar Lev, Phys. Rev. A **99**, 032114 (2019)

6.1 Introduction

Be it gravity, electromagnetic force or dipole-dipole interactions, power-law interactions are ubiquitous. While sufficiently dense mobile charges are able to screen the interaction and effectively truncate its range, in many cases long-range interactions are important. A few of the notable examples in conventional condensed matter systems are nuclear spins [140], dipole-dipole interactions of vibrational modes [141–143], Frenkel excitons [144], nitrogen vacancy centers in diamond [145–149] and polarons [150]. Long range interactions are also common in atomic and molecular systems, where interaction can be dipolar [151–156], van der Waals like [151, 157], or even of variable range [158–161].

It was rigorously established by Lieb and Robinson that generic correlations in quantum

system with *short-range* interactions propagate within a linear "light-cone", $t/v = x$, with a finite velocity [162]. Outside this "light-cone" correlations are exponentially suppressed [162]. Specifically this implies that transport in local quantum systems cannot be faster than ballistic.

For systems with long-range interactions the result of Lieb and Robinson doesn't hold, but was later generalized by Hastings and Koma, who showed that for $\alpha > 1$, the causal region in such systems becomes at most logarithmic, $t \sim \log x$ [163]. This result was subsequently improved to an algebraic "light-cone", $t \sim r^\delta$ for $\alpha > 2$ and $0 < \delta < 1$ [164]. A Hastings-Koma type bound was also obtained for $\alpha < 1$ after a proper rescaling of time [165]. While the spreading of generic correlations was numerically studied in a number of studies [58, 166–173], much less is known about transport in long-range interacting systems. Some information can be gained from quadratic fermionic models with long-range hopping [174, 175], however these systems are integrable and can thus show nongeneric features. The results of Ref. [164] suggest that transport in long-range systems is *at most* superdiffusive for $\alpha > 2$, but leaves a number of important questions open: (a) Is there an α above which diffusion is recovered, similarly to the situation for classical Lévy flights? [176] (b) Is there an α, below which mean-field like dynamical behavior takes place?

In this work we address these questions by studying spin-transport using the time-dependent variational principle in the manifold of matrix product states (TDVP-MPS) [21, 22, 121, 177]. The main outcome of our study can be read from the cartoon in Fig. 6.1.

TDVP-MPS belongs to the family of matrix product states (MPS) methods [13], and thus allows to study long spin chains (chains up to $L = 1201$ were considered here), way beyond what is accessible using exact diagonalization. The main advantage of this method over the conventional time-evolving block decimation (TEBD) or time-dependent density
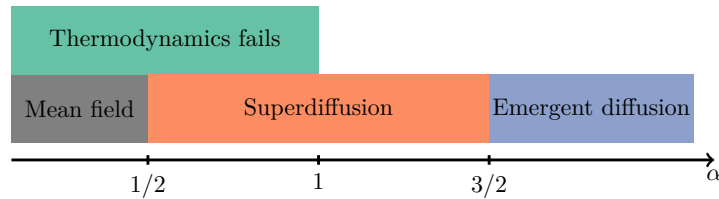
Figure 6.1: A cartoon describing the nature of transport in one-dimensional interacting systems, with an interaction decreasing as $r^{-\alpha}$ with the distance. For $0 < \alpha < 1$ the energy of the system is superextensive, resulting in the failure of conventional thermodynamics. For $0 < \alpha < 1/2$, dynamics corresponds to dynamics of the infinite-range ($\alpha \to 0$) mean-field model in the limit of $L \to \infty$. For $\alpha > 1/2$ transport combines diffusive and superdiffusive features, with a finite diffusion coefficient for $\alpha > 3/2$ and $\langle x^{2q} \rangle (t) \sim t^q$ for $q < \alpha - 1/2$.

matrix renormalization group (tDMRG) approaches for time-evolution [20, 178, 179] is that the evolution is unitary by construction, and the method explicitly conserves a number of macroscopic quantities, such as the total energy, total magnetization and total number of particles [21, 22, 121, 177]. Moreover unlike TEBD and tDMRG the method can be directly applied for long-range interacting systems. While the method is numerically exact in the limit of large bond dimension (which sets the number of variational parameters), it is limited by the growth of entanglement entropy with time [13]. For a fixed bond dimension, the equations of motion of TDVP-MPS can be derived from a classical nonquadratic Lagrangian in the space of variational parameters [21, 60]. These equations are typically chaotic and yield diffusive transport. Based on this observation as well as the conservation properties of TDVP-MPS it was argued that the method could potentially recover correct hydrodynamic behavior also for a relatively small bond dimension [60], a result which was challenged in Ref. [61]. We note in passing that this line of thought is not applicable for long-range systems, where diffusive transport is not expected *a-priori*, and the entire hydrodynamic approach is questionable. Therefore here we strictly use TDVP-MPS as a numerically exact method.

6.2 Model

We study a one-dimensional spin-chain of length L, given by the Hamiltonian $\hat{H} = \hat{H}_{\text{loc}} + \hat{H}_{\text{lr}}$ where

$$\hat{H}_{\text{loc}} = \sum_{i=1}^{L-1} \left(\hat{S}_i^x \hat{S}_{i+1}^x + \hat{S}_i^y \hat{S}_{i+1}^y \right) + \sum_{i=1}^{L-2} \left(\hat{S}_i^x \hat{S}_{i+2}^x + \hat{S}_i^y \hat{S}_{i+2}^y \right), \qquad (6.1)$$

is the local part and,

$$\hat{H}_{\text{lr}} = \sum_{i=1}^{L-1} \sum_{j>i+1}^{L} \frac{1}{(j-i-1)^\alpha} \left(\hat{S}_i^x \hat{S}_j^x + \hat{S}_i^y \hat{S}_j^y \right), \quad (6.2)$$

includes power-law decaying long-range interactions and $\hat{S}_i^x$ and $\hat{S}_i^y$ are spin-$1/2$ operators. The Hamiltonian conserves the total magnetization, and thus supports energy and spin transport. We introduce a next-nearest neighbor term in order to break integrability in the limit of $\alpha \to \infty$. In this limit the Hamiltonian reduces to the XX ladder, which has diffusive spin transport [61, 131, 180, 181].

6.3 Method

To assess spin transport in the system we numerically compute the two-point spin-spin correlation function at infinite temperature,

$$C_x(t) = \frac{4}{2^L} \text{Tr} \left(\hat{S}_{L/2+x}^z(t) \hat{S}_{L/2}^z(0) \right), \qquad (6.3)$$

which corresponds to the time-dependent profile of a local excitation at the center of the chain performed at $t = 0$. We choose to work at infinite temperature, since such a state corresponds to a typical initial state [182], which increases the generality of our results. The excitation
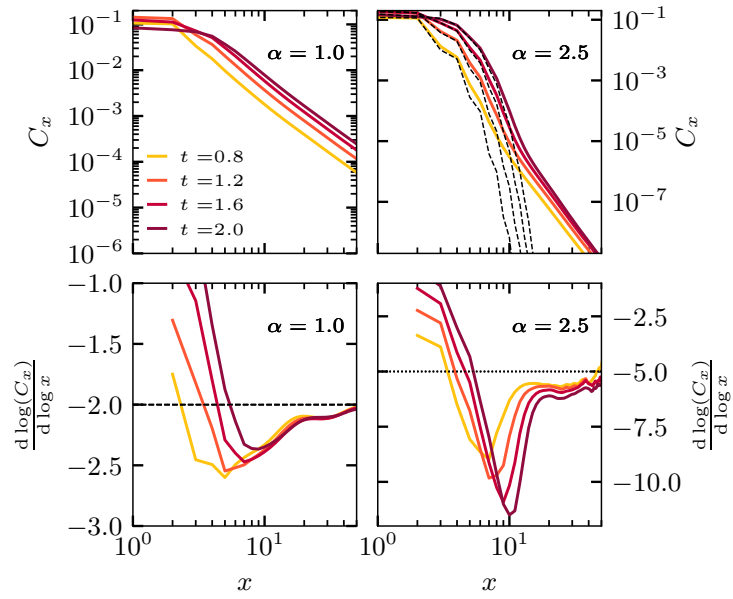
Figure 6.2: *Upper panels.* Spin excitation profiles as a function of time for two representative α. The dashed black lines correspond to results obtained in the $\alpha \to \infty$. Darker tones represent longer times. *Lower panels.* Logarithmic derivative of the spin excitation profiles. The dashed black lines are guides to the eye for 2α. $L = 201$, $\chi = 256$.

profile is obtained by propagating the operators, $\hat{S}_i^z(t)$, under the Heisenberg evolution and accessible timescales are limited by the growth of entanglement entropy. Using the cyclic property of the trace $C_x(t)$ can be written as,

$$C_x(t) = \frac{4}{2^L} \mathrm{Tr}\left(\hat{S}_{L/2+x}^z\left(-\frac{t}{2}\right)\hat{S}_{L/2}^z\left(\frac{t}{2}\right)\right),\qquad(6.4)$$

which allows us to reach twice as large times [183]. Since we work with an approximately translationally invariant system (we use open boundary conditions), in practice, we propagate only *one* operator at the center of the lattice, because operators which are far enough from the boundaries of the chain can be obtained approximately by a simple translation (see Appendix 6.7). To mitigate the boundary effects introduced by this approximation we show $C_x(t)$ only for the central $L/2$ sites of the chain. If not stated otherwise, we use spin-chains of length $L = 201$, which is sufficient to have finite size effects under control for most ranges of the interaction.

To propagate the operators we use the time-dependent variational principle (TDVP), which yields a locally optimal (in time) evolution of the wavefunction on some variational manifold. It amounts to solving a tangent-space projected Schrödinger equation [22],

$$\frac{d}{dt}\left|\hat{O}(t)\right\rangle = -\mathrm{i}P_{\mathcal{M}}\hat{H}\left|\hat{O}(t)\right\rangle,\qquad(6.5)$$

where $P_{\mathcal{M}}$ is the tangent space projector to the variational manifold $\mathcal{M}$ and $\left|\hat{O}(t)\right\rangle$ is a vectorization of a general operator $\hat{O}(t)$. We use the matrix product operator (MPO)

representation of the operator,

$$\hat{O}(\boldsymbol{A}) = \sum_{\{\sigma_i\},\{\sigma_i'\}} A_1^{\sigma_1\sigma_1'} \dots A_N^{\sigma_N\sigma_N'} |\sigma_1 \dots \sigma_n\rangle \langle \sigma_1' \dots \sigma_n'| , \tag{6.6}$$

where $\sigma_i = \pm 1/2$ correspond to the states of a spin at site i and $A_i^{\sigma_i\sigma_i'} \in \mathbb{C}^{\chi_{i-1} \times \chi_i}$ are complex matrices where χ_i is the bond-dimension of the matrix ($\chi_0 = \chi_N = 1$) [13]. An exact representation of a general operator requires the bond dimension to grow exponentially with system size L. Therefore truncating the maximal bond-dimension to a fixed value introduces an approximation, but allows to keep the MPO representation tractable. We use a family of fixed finite bond-dimension MPOs to parameterize the variational manifold, $\mathcal{M}$. Numerically exact results are achieved by convergence with respect to the bond-dimension (in this work we used bond-dimension of up to 512, see Appendix 6.6). The evolution of (6.5) is performed using a second-order Trotter decomposition with time-steps from 0.005 to 0.1. The Hamiltonian is approximated as a sum of exponentials and a short-ranged correction, which can be efficiently represented as an MPO. The number of exponentials is chosen such that the resulting couplings do not differ by more than 2% from the exact couplings for any pair of sites [32]. We note in passing that since the evolution is unitary in the *enlarged* vector space of the vectorized operators, the method explicitly conserves the norm of the operator, $\langle \hat{O}(t) | \hat{O}(t) \rangle \equiv \mathrm{Tr}\, \hat{O}^\dagger(t) \hat{O}(t) = \mathrm{Tr}\, \hat{O}^\dagger \hat{O}$, but *not* its trace, $\mathrm{Tr}\, \hat{O}(t)$.

6.4   Results

Figure 6.2 shows the spin excitation profile, $C_x(t)$, for short times and two values of $\alpha = 1$ and 2.5. Since the excitation profile is symmetric with respect to the center of the lattice in
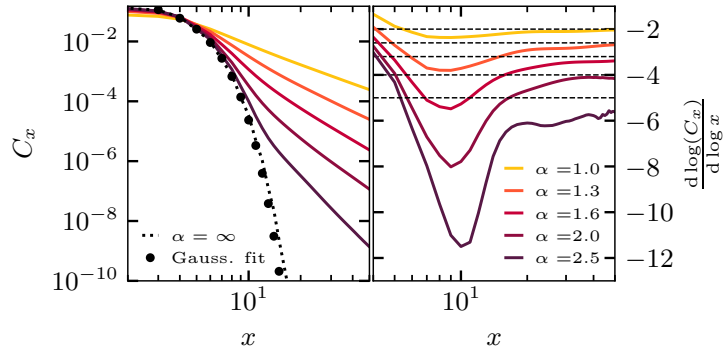
Figure 6.3: *Left panel.* Spin excitation profiles at $t = 2.0$ and various α. Darker tones represent larger α-s. The black dots represent a Gaussian fit. *Right panel.* Logarithmic derivative of the spin excitation profiles. The dashed black lines are guides to the eye for 2α. $L = 201$, $\chi = 256$.

the following figures we only show its right side ($x > 0$). For $\alpha = 2.5$, and small distances from the initial excitation, the profile resembles a Gaussian and superimposes well with the $\alpha \to \infty$ profile calculated at same time points. For larger distances there is a crossover from a Gaussian form to a power-law form, $x^{-\gamma}$. For smaller α, the crossover is less pronounced and there is no apparent region of Gaussian behavior (although it might develop at later times). Since the accessible times in this work are short ($t \leq 4$) due to fast growth of entanglement entropy, it is pertinent to question what our results imply on bulk transport? From Fig. 6.2 it is apparent that the power-law tail appears already at very short times, and its exponent γ seems to be independent of time, as can be judged from convergence of the logarithmic derivative, $\mathrm{d}\log C_x(t)/\mathrm{d}\log\mathrm{x}$, to the same value of γ (see bottom panels of Fig. 6.2). This leads us to argue that the long-range nature of the interactions speeds up the approach to asymptotic transport and allows us to observe at least some of its features.

In Fig. 6.3 we show the spin excitation profile at $t = 2$ for all analyzed α. The power-law regime, $x^{-\gamma}$, is visible for all α and the exponent $\gamma(\alpha)$ is α dependent. To assess this dependence we calculate the corresponding logarithmic derivative (see right panel of Fig. 6.3),
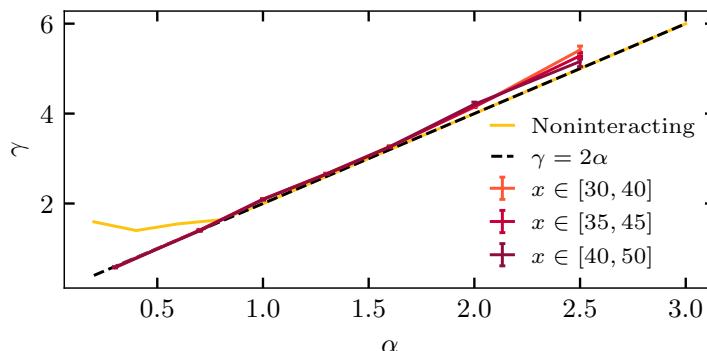
Figure 6.4: The power-law exponent, γ, of the power-law tail in the spin excitation profiles obtained by averaging over the logarithmic derivative in Fig. 6.3 in different spatial regions. The yellow (light) line is the exponent γ computed for the noninteracting model in Eq. (6.7). The dashed black line corresponds to $\gamma = 2\alpha$.

which converges to its asymptotic value, γ, at large distances. The logarithmic derivative becomes increasingly noisy at large distances, x, (where $C_x(t) < 10^{-8}$), due to decreasing signal-to-noise ratio, which prohibits us to obtain an even better convergence.

To assess the convergence of the results we have extracted γ by averaging the logarithmic derivative on various spatial intervals, and we note that γ converges to the $\gamma = 2\alpha$ line. To further substantiate the power-law tail of $C_x(t)$ we compare our results to a noninteracting long-range hopping model,

$$\hat{H}_{\text{nonint}} = \sum_{i=1}^{L} \sum_{x=1}^{L-1} \frac{1}{x^\alpha} \hat{c}_i^\dagger \hat{c}_{i+x}, \tag{6.7}$$

where $\hat{c}_i^\dagger$ creates a spinless fermion at site i (for analytical results at the groundstate, see Refs. [174, 184, 185]). The probability of a particle to hop for site i to site $i+x$ is $P(x, \Delta t) = \left| \left\langle i+x \left| \exp\left(-i\hat{h}\Delta t \right) \right| i \right\rangle \right|^2$, where $\hat{h}$ is the single-particle Hamiltonian, yielding for small Δt, $P(x) \approx h_{i+x,i}^2 \Delta t^2 \sim |x|^{-2\alpha}$. This suggests $\gamma = 2\alpha$, which we indeed observe numerically for $\alpha \geq 1$, see Fig. 6.4. Interestingly, the two models differ for $\alpha < 1$, where the interacting model continues to follow the $\gamma = 2\alpha$ line.

Many-times transport is characterized by considering the time-dependence of the moments of the spin excitation profile,

$$\left\langle x^{2q} \right\rangle (t) = \frac{1}{2} \sum_{x=0}^{L} x^{2q} C_x (t). \tag{6.8}$$

Specifically, the first nonvanishing moment ($q = 1$), also known as the mean-square displacement (MSD), is directly related to the the time-dependent diffusion coefficient , $D(t) = \mathrm{d} \left\langle x^2 \right\rangle / \mathrm{d}t$, which converges to the linear response diffusion coefficient for $t \to \infty$ (see Appendix of Ref. [130]). Since we obtain that asymptotically $C_x (t) \sim x^{-2\alpha}$, all moments with $q > \alpha - 1/2$ diverge in the limit $L \to \infty$. In the left panels of Fig. 6.5 we demonstrate this behavior for $q = 1$. While $\alpha = 1.3$ shows a divergence of $D(t)$ with system size, for $\alpha = 3$ the time-dependent diffusion coefficient does *not* depend on the system size, and approaches a plateau as a function of time, indicative of diffusive transport, $\left\langle x^2 \right\rangle \sim Dt$. This is consistent with our observation that the central part of the excitation profile is well described by the dynamics of a local system ($\alpha \to \infty$), which is diffusive [61, 131, 180, 181].

We note that $\alpha = 1/2$ plays a special role, since for $\alpha < 1/2$, $C_x (t) \sim x^{-2\alpha}$ becomes nonintegrable. This is in a contradiction to the fact that $\sum_x C_x (t) = \sum_x C_x (0) = 1$, which follows from the conservation of total magnetization. The resolution of this apparent paradox follows from the dependence of $C_x (t)$ on the system size for $\alpha < 1/2$, which makes the entire excitation profile (for any finite time) vanish in the limit $L \to \infty$ [186–189]. The dependence of the excitation profile on the system size for $\alpha < 1/2$ can be eliminated by a proper rescaling of time, $t \to t f(L)$, where $f(L)$ is some increasing function of L. We have empirically found that taking $f(L) = \sqrt{2 H_{L/2}^{(2\alpha)}} \equiv \left(2 \sum_{x=1}^{L/2} x^{-2\alpha} \right)^{1/2}$ (namely the ℓ^2-norm of the long-range part) gives a perfect scaling collapse (see right panels of Fig. 6.5) for $\alpha < 1$[1].

---

[1]For $1/2 < \alpha$ such a rescaling is not required for sufficiently large system sizes. For small system sizes
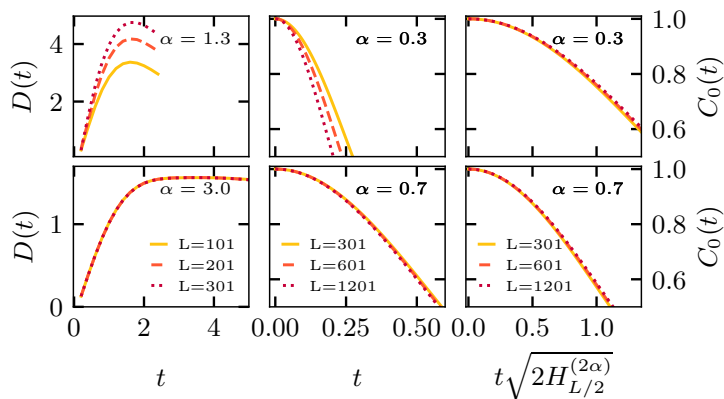
Figure 6.5: *Left panels.* Time-dependent diffusion constant $D\left(t\right)$ for $\alpha = 1.3$ and 3 and three different system sizes, $L = 101$ ($\chi = 512$), 201 and 301 ($\chi = 256$). *Middle and right panels.* Short-time relaxation of the central spin, $C_0\left(t\right)$ for $\alpha = 0.3$ and 0.7 versus time (middle) and rescaled time (right) using the square root of the generalized harmonic numbers, $\sqrt{H_{L/2}^{(2\alpha)}}$ (see text) for $L = 301, 601$ and $1, 201$ and $\chi = 128$.

In the limit of large system sizes and for $\alpha < 1/2$, this rescaling corresponds to $\tau \sim tL^{1/2-\alpha}$ and is consistent with the analytically obtained rescaling for a classical model [186, 189].

6.5 Discussion

Using a numerically exact method (TDVP-MPS) we study infinite temperature spin transport in a nonintegrable one-dimensional spin chain, with interactions which decay as $x^{-\alpha}$ with the distance. While the method allows us to address chains far beyond what is accessible using exact diagonalization, it is inherently limited to short times due to fast growth of entanglement entropy. Nevertheless, we show that the long-range of the interactions allows to access some of the asymptotic features of transport in our simulations.

We find two pronounced regimes in the dynamics of a spin excitation. For $\alpha < 1/2$, we

---

a notable residual dependence on the system size might exist, especially for α close to 1/2, due to slow convergence of $H_L^{(2\alpha)}$. The same rescaling of time as we use for $\alpha < 1/2$ eliminates this residual dependence.

find that the decay of the excitation depends on the system size, such that the relaxation time $t_0 \propto (\sum_k J_{0k}^2)^{-1/2} \sim L^{\alpha-1/2}$ (where $J_{ij} \sim |i-j|^{-\alpha}$ is the long-range part of the Hamiltonian), and goes to zero in the limit of $L \to \infty$. For *finite* system sizes the spatial decay of the excitation profile is $C_x(t) \sim x^{-2\alpha}$.

For $\alpha > 1/2$, there is a residual dependence of the excitation profiles on the system size, which vanishes in the $L \to \infty$ limit. For short distances the spatial excitation profiles are well described by the corresponding profiles of a local system, which for generic systems are Gaussian, corresponding to diffusive transport. For longer distances the Gaussian form crosses-over to a power-law behavior with an exponent, which approaches, $C_x(t) \sim x^{-2\alpha}$. The crossover is much more apparent for larger α, and is barely visible for the smaller α. Our data is inconclusive with respect to the existence of a critical $\alpha_c > 1/2$ below which the crossover vanishes, since it is possible that longer times are needed to observe the crossover for the smaller α. The crossover point drifts to longer distances for larger α and longer times, but we were not able to determine its precise functional dependence.

Due to the asymptotic power-law dependence of the excitation profile, only moments $\langle x^{2q} \rangle (t)$ with $q < \alpha - 1/2$ exist (see Eq. 6.8). We find that for $\alpha > 3/2$ the MSD, which corresponds to $q = 1$, exists and is *not* system-size dependent. Moreover it appears to increase linearly with time, which we demonstrated by calculating its derivative. While this behavior corresponds to diffusion, the dynamics is *not* truly diffusive for any α, due to the divergence of higher moments. This is in stark contrast to *classical* superdiffusive systems, such as Lévy flights, where a critical α exists, above which diffusion is restored. The nice agreement of the "core" of the excitation profile with a Gaussian form, corresponding to diffusion, leads us to speculate that *all* the existing moments have a diffusive time-dependence, namely, $\langle x^{2q} \rangle (t) \sim t^q$, for $q < \alpha - 1/2$. While the functional dependence

of $\langle x^{2q} \rangle$ that we observe, could still be not asymptotic due to the limited times of our numerical simulations, the divergence of moments for $q > \alpha - 1/2$ follows solely from the power-law dependence of the tail of $C_x(t)$, which develops already at very early times and was motivated both analytically and numerically by considering a related noninteracting model. It is thus very likely that the power-law tails exist also at asymptotic times.

In this work we consider one model, which is nonintegrable for all α. While groundstate properties where shown to be model dependent [168], such microscopic sensitivity is *not* expected for sufficiently high temperatures, where the system is sufficiently far from any ordered quantum phase, and is not well described using quasiparticles. We therefore expect our results, obtained in the limit of infinite temperature, to hold for a broad family of nonintegrable long-range models and any typical initial state. It would be interesting to extend our results to higher dimensions.

6.6 Convergence Tests

Numerical exactness of the dynamics generated by TDVP-MPS is obtained by converging with respect to the bond-dimension, χ. In Figures 6.6 and 6.7, we provide comparisons of calculations with bond-dimensions up to $\chi = 512$ for quantities of interest in this study. Evaluating the spatial spin excitation profile in the tails becomes sensitive to numerical noise for small values of C_x (smaller than 10^{-8}) and is limited by a complex interplay of time-step errors and accumulation of numerical round-off errors. Therefore, obtaining accurate tails of C_x is harder for the large α, where C_x decreases faster with the distance. $\alpha = 2.5$ is the shortest-ranged system for which it is possible to calculate a meaningful tail of C_x. In contrast, the mean square displacement is robust to the numerical noise in the far tails
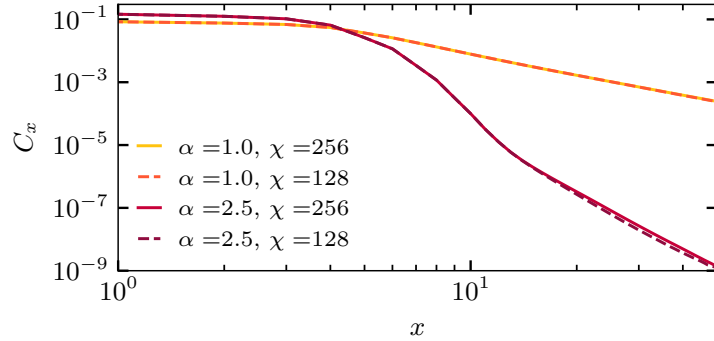
Figure 6.6: Convergence of the spin excitation profile with respect to bond-dimension, χ, at $t = 2.0$, $L = 201$ and $dt = 0.005$.
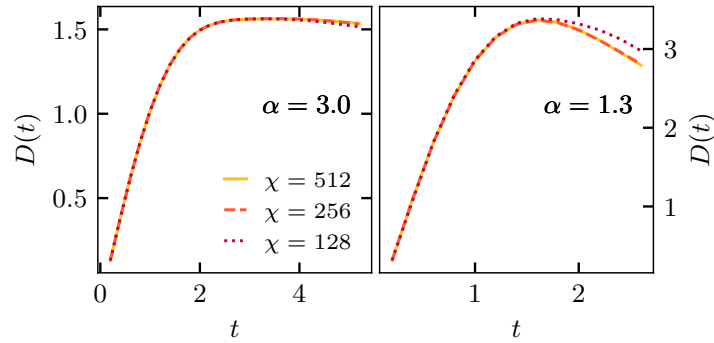
Figure 6.7: Convergence of the time-dependent diffusion constant $D(t)$ with respect to bond-dimension for $\alpha = 1.3$ and $\alpha = 3$ for $L = 101$ and $dt = 0.1$.

for the system sizes and times considered here, and longer times are accessible for larger α. The relaxation of the central spin, $C_0(t)$, at short times is converged with a moderate bond-dimension $\chi = 64$, see Fig. 6.8.

Figure 6.8: Convergence of the relaxation of the central spin $C_0(t)$ with respect to bond-dimension for $\alpha = 0.3$ and $\alpha = 0.7$ ($L = 1201$).

6.7 Approximate evaluation of $C_x(t)$

Obtaining the correlation function,

$$C_x(t) = \frac{1}{2^L} \text{Tr}\, \hat{S}^z_{L/2}\left(-\frac{t}{2}\right) \hat{S}^z_{L/2+x}\left(\frac{t}{2}\right),\qquad(6.9)$$

of a spin-chain of length L scales as $\mathcal{O}(L^2)$, since for each operator, a separate calculation has to be performed. However, the scaling can be reduced to $\mathcal{O}(N)$ by making use of the approximate translational invariance of the $\hat{S}^z_i(t)$. In the limit of large system and for sites i close to the center, the correlation function can be evaluated approximately using only $\hat{S}^z_{L/2}(t)$,

$$C_x(t) \approx \frac{1}{2^L} \text{Tr}\, \hat{S}^z_{L/2}\left(-\frac{t}{2}\right) \boldsymbol{T}_x \hat{S}^z_{L/2}\left(\frac{t}{2}\right),\qquad(6.10)$$

where the action of the translation operator $\boldsymbol{T}_x$ is illustrated in Fig. 6.9. It can be understood as relabeling of the lattice sites i in a cyclically translated manner: $\forall i \in [1, L] : i \to (i + x)$ mod L. The trace in Eq. (6.10) can be performed if the matrix product operator (MPO) is expanded at both ends with virtual sites connected containing identity operators and
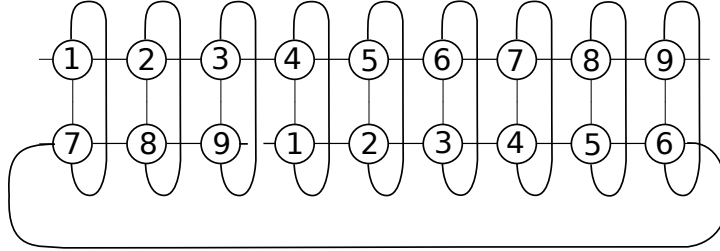
Figure 6.9: Tensor network diagram for Eq. (6.10). Each tensor in the network is labeled with the physical site it represents. The upper MPO corresponds to the untranslated operator $\hat{S}^z_{L/2}\left(-\frac{t}{2}\right)$ while the lower MPO is its translated version $\boldsymbol{T}_3\hat{S}^z_{L/2}\left(\frac{t}{2}\right)$.

connected with a bond-dimension of 1. There is no need to evaluate $\hat{S}^z_{L/2}\left(-\frac{t}{2}\right)$, since it is just the complex conjugate of $\hat{S}^z_{L/2}\left(\frac{t}{2}\right)$. In a vectorized notation the calculation of $C_x\left(t\right)$ therefore amounts to the calculation of $\left\langle \hat{S}^z_{L/2}\left(\frac{t}{2}\right) | \boldsymbol{T}_x | \hat{S}^z_{L/2}\left(\frac{t}{2}\right) \right\rangle$.

The deviation between $C_x(t)$ obtained from the explicit propagation of all $\hat{S}^z_x$ and $C_x(t)$ calculated within this approximation is negligible for the chain lengths we use in this study, see Fig. 6.10. We have verified that the large errors after site 40 are not related to a breakdown of the approximate scheme, but occur due to the small signal-to-noise ratio for very small $C_x(t)$. For lattice sites close to the end of the chain, the approximation is expected to cause significant errors.
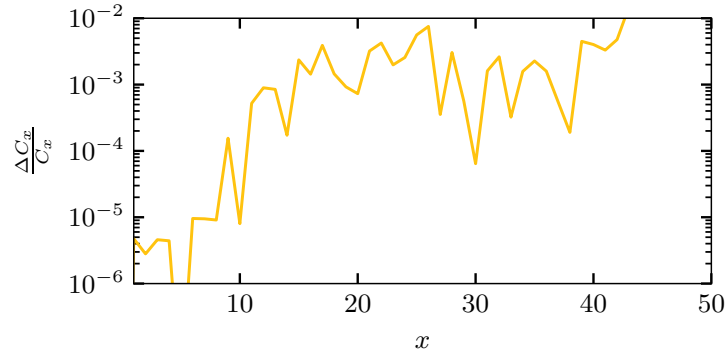
Figure 6.10: Relative deviation between the spin excitation profiles obtained with and without the approximation described in the text. Data shown is for $t = 2.0$, $\alpha = 2.0$, $dt = 0.1$, $\chi = 128$, $L = 201$.

Chapter 7

Spin transport in disordered long-range interacting spin chain

This chapter was published as: B. Kloss and Y. Bar Lev,

7.1   Introduction

Many-body localization (MBL) extends the notion of Anderson localization to interacting systems [124]. For local interactions, its existence is well established theoretically [6, 191] and experimentally in one-dimensional systems [192–194] (see [7] for a recent review), but there is evidence of localization also in two-dimensional systems [137, 195–199]. For long-range interactions the fate of MBL is less clear. Some studies suggest that the many-body localization is stable for $\alpha > 2d$ [200–203], with d the spatial dimension, some suggest it is stable for $\alpha > d/2$ [204], and some claim it is unstable for any finite α in the thermodynamic limit [205–207]. Understanding the dynamics of disordered systems with long-range inter- actions is of great importance to a number of physical systems, such as nuclear spins [140],

dipole-dipole interactions of vibrational modes [141–143], Frenkel excitons [144], nitrogen vacancy centers in diamond [145–149] and polarons [150]. Long range interactions are also common in atomic and molecular systems, where interactions can be dipolar [151–156], van der Waals like [151, 157], or even of variable range [158–161]. Some aspects of the dynamics in such systems were studied numerically in Ref. [203, 208, 209], analytically in Ref. [210] and experimentally in Ref. [211], however spin transport in such systems was not considered.

The delocalized phase of disordered one-dimensional systems with local interactions shows subdiffusive transport [133–136, 212], accompanied by sublinear growth of the entanglement entropy [213–215] and intermediate statistics of eigenvalue spacing [216]. Anomalous transport is commonly explained by rare insulating regions, which effectively suppress transport in one-dimensional systems. This mechanism is known as the Griffith's picture [134, 217, 218] (see Ref. [219] for a recent review and also Ref. [220] were rare regions were introduced externally). In dimensions higher than one the Griffiths picture predicts diffusion, since rare regions can be circumvented [218], however *approximate* numerical studies [137] as also recent experiments [196, 197] suggest that at least for short to intermediate times the relaxation and transport appears to be anomalous. It is crucial to understand if this discrepancy follows from incompleteness of the Griffiths picture or the approximation of the method. While there are no efficient *numerically exact* methods to study the *dynamics* of two-dimensional interacting systems, some progress can be obtained for one-dimensional long-range interacting systems. The Griffiths picture was not generalized to this setting, but in analogy to the reasoning of higher dimensions [218], normal diffusive behavior is expected.

In a previous work we have shown that for *clean* systems with long-range interactions the local part of the Hamiltonian dictates the spreading of the *bulk* of a local spin excitation, while the long-range part of the Hamiltonian only introduces a weak *perturbative* effect, in

the face of power-law tails of the excitation profile, with an exponent proportional to α [139]. The tails yield a superdiffusive signature of transport for all α, if a sufficiently high moment of the excitation profile is considered, and for $\alpha < 3/2$ the diffusion constant diverges with system size [139]. A natural question which arises is whether the effect of long-range interactions in disordered systems goes beyond a perturbative correction as it happens for their clean counterparts. Moreover, if localization is destabilized by long-range interactions, *what is the resulting nature of spin transport?*

In this work we consider and answer these questions using a numerically exact matrix product state (MPS) method. The study of long-ranged interacting systems naturally requires large system sizes. In fact, in Section 7.7 we show that for $\alpha = 1.75$, finite size effects are pronounced even for a chain of 51 spins, which is currently considered as the state-of-the-art limit of exact diagonalization based techniques [221]. MPS techniques are therefore indispensable to obtain numerically exact results for chains with long-range interaction, albeit only up to some finite time. This limitation arises since the required numerical effort scales exponentially with the entanglement entropy of the state, which for nonintegrable systems is known to grow linearly with time [222]. We stress that our aim here is *not* to address the question of stability of the MBL phase in the presence of long-range interactions, but to study the dynamics in the delocalized phase. Moreover, since it is technically hard to distinguish between very slow transport and absence of transport, especially in a limited time-interval, our method is not well suited for such purpose.

Time-evolution of long-ranged systems can be conveniently obtained by the time-dependent variational principle (TDVP) applied to the manifold of MPS [21, 22, 121]. It was successfully utilized to study the dynamics of spin chains with local interactions in disordered or quasiperiodic potentials [223, 224]. For low bond dimensions and very far from the numeri-

cally exact limit this method was proposed as an inexpensive candidate to achieve accurate hydrodynamic description of transport [60], however it was shown to be unreliable for generic systems [61]. In this study, we use TDVP as a *numerically exact* method, and study the nature of transport in long-range-interacting disordered one-dimensional spin chain. We focus on parameter regimes in which the interaction is sufficiently short-ranged such that the corresponding clean system shows asymptotic diffusive behavior, and disorder ranges for which the system is argued to be delocalized by all existing theories.

7.2 Model

We study transport properties of the one-dimensional long-ranged disordered Heisenberg model,

$$\hat{H} = J \sum_{i=1}^{L-1} \sum_{j>i}^{L} \frac{1}{(j-i)^{\alpha}} \left(\hat{S}_i^x \hat{S}_j^x + \hat{S}_i^y \hat{S}_j^y + \hat{S}_i^z \hat{S}_j^z \right) + \sum_{i=1}^{L} h_i \hat{S}_i^z, \tag{7.1}$$

where h_i is uniformly distributed in the interval $[-W, W]$ and $\hat{S}_i^{(x,y,z)}$ are the appropriate projections of the spin-1/2 operators on site i. In the following, we use $J = 1$, which sets the time unit of the problem. To study the dynamical properties of this model we start the system from a random product state, $|n\rangle$, in the eigenbasis of $\hat{S}_i^z$ and calculate the growth of the entanglement entropy $S(t)$ as also the spreading of a spin-excitation as a function of time, which is assessed from the two-point spin correlation function,

$$C_x^n(t) = \left\langle n \left| \hat{S}_{L/2+x}^z(t) \hat{S}_{L/2}^z(0) \right| n \right\rangle. \tag{7.2}$$

The entanglement entropy is directly available since we use the two-site TDVP method [22]. We then average both $S(t)$ and $C_x^n(t)$, by randomly sampling both the disorder and the

initial state of the system, such that any state has an equal probability to occur. This corresponds to an infinite temperature ensemble, $C_x(t) = \mathcal{N}^{-1} \sum C_x^n(t)$, where $\mathcal{N}$ is the Hilbert space dimension. It is convenient to characterize the spreading by the width of the averaged excitation profile,

$$\sigma^2(t) = \sum_{x=-L/2}^{L/2} x^2 C_x(t) \tag{7.3}$$

which is analogous to the classical mean-square displacement (MSD). Typically the MSD scales as, $\sigma^2(t) \sim t^\gamma$, with $\gamma = 2$ ($\gamma = 1$) for ballistic (diffusive) transport and $0 < \gamma < 1$ corresponding to subdiffusive transport. We use the log-derivate to define a time-dependent dynamical exponent $\gamma(t) = \mathrm{d} \ln \sigma^2(t) / \mathrm{d} \ln t$, which asymptotically converges to γ. We also compute the linear derivative of the MSD, $d\sigma^2/dt$, which corresponds to a time-dependent diffusion coefficient $D(t)$. In the limit of long times it converges to constant a constant for diffusion and zero for subdiffusion. Similarly, we define the time-dependent dynamical exponent $\delta(t) = \mathrm{d} \ln S(t) / \mathrm{d} \ln t$, to characterize the spread of the entanglement.

7.3 Method

The Hilbert-space dimension of a quantum lattice systems scales exponentially with the size of the system. Any wavefunction in the Hilbert space can be written as a matrix product state (MPS),

$$|\Psi[A]\rangle = \sum_{\{s_n\}=1}^{d} A^{s_1}(1) A^{s_2}(2) \dots A^{s_N}(L) |s_1 s_2 \dots s_L\rangle \tag{7.4}$$

where d is the local Hilbert space dimension, $A^{s_i}(i) \in \mathbb{C}^{D_{i-1} \times D_i}$ are complex matrices and $D_0 = D_L = 1$, such that the product of matrices evaluates to a scalar coefficient for a given

configuration $|s_1 s_2 \ldots s_L\rangle$. To be an *exact* representation of the wavefunction the dimension of the matrices, the bond dimension, must scale exponentially with the systems size. Typically one approximates the wavefunction by truncating the dimension of the matrices to a predetermined dimension with a computationally tractable number of parameters. Exact results are obtained when the approximate dynamics are converged with respect to the bond dimension.

The time-dependent variational principle (TDVP) allows one to obtain a locally optimal (in time) evolution of the wavefunction on the manifold of MPS, $\mathcal{M}_\chi$, with some fixed bond dimension χ. It amounts to solving a tangent-space projected Schrödinger equation [22]:

$$\frac{d\left|\Psi[A]\right\rangle}{dt} = -\mathrm{i}P_\mathcal{M}\hat{H}\left|\Psi[A]\right\rangle, \tag{7.5}$$

where $P_\mathcal{M}$ is the tangent space projector to the manifold $\mathcal{M}_\chi$. Equation (7.5) is solved using a second-order Trotter-Suzuki decomposition of the projector. The Hamiltonian is approximated as a sum of exponentials, which can be efficiently represented as an MPO [32]. The number of exponentials is chosen such that the resulting couplings do not differ by more than 2% from the exact couplings for any pair of sites. Through this work we have used a bond-dimension of up to $\chi = 1024$ and timestep of $dt = 0.1$ and verified that our results are convergent with respect to these numerical parameters (see Section 7.6). We average over initial conditions and disorder realizations at the same time and use 1000 realizations unless stated otherwise. All calculations are performed using the TenPy library using a two-site version of the TDVP for MPS and exploiting that the Hamiltonian conserves the total magnetization [120].
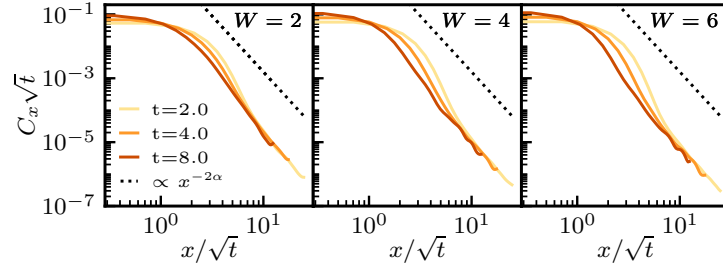
Figure 7.1: Rescaled magnetization profiles at different times on log-log scale for bond dimension $\chi = 512$, system size $L = 75$, and different disorder strengths ($W = 2.0, 4.0$ and 6.0 from left to right). The shaded area shows the standard deviation of the profile obtained from a bootstrapping procedure. Profiles are smoothed by a Gaussian filter with a standard deviation of 2.0. Black dotted line is a guide to the eye of a power-law, $x^{-2\alpha}$.

7.4 Results

For transport that is not purely diffusive, the MSD contains only *partial* information on transport, since in this case the asymptotic shape of the profile is *not* described by a Gaussian. To get a full picture of transport it is therefore pertinent to examine the evolution in time of the excitation profiles, which we do in Fig. 7.1. Similarly to the clean case in Refs. [139, 225], the tails of the excitation profile follow a power-law of -2α regardless of the disorder strength, which shows that the disorder cannot suppress long-range hops of the spin. These tails are responsible for the divergence of the MSD and the diffusion coefficient with system size for $\alpha < 3/2$. As is clear from Fig. 7.1, a rescaling of data, which is consistent with diffusion, fails (c.f. Fig. 7.5, where it works), indicating that transport is *not* diffusive.

To assess the influence of the disorder on the dynamics we focus on $\alpha = 1.75$ and compute the averaged bipartite entanglement and the MSD (6.8) for a number of disorder strengths $W \in [2, 12]$, which are predicted to be in the delocalized phase [206]. Figure 7.2 shows the MSD (6.8) and the entanglement entropy, $S(t)$, as a function of time for various disorder strengths together with the corresponding linear and logarithmic derivatives. All data is
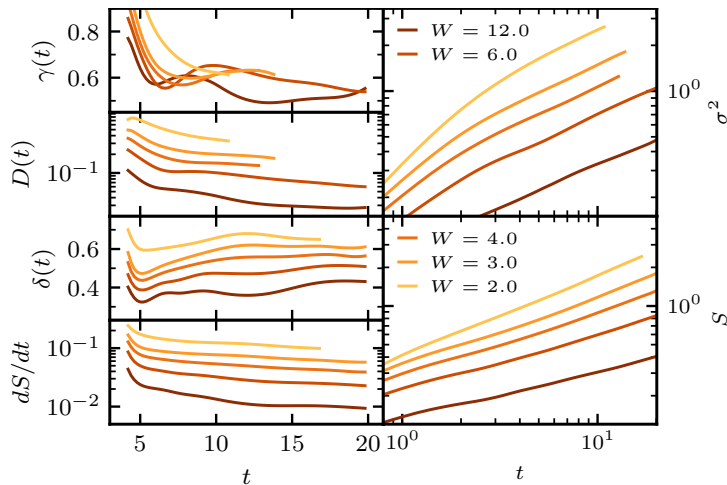
Figure 7.2: *Right column.* MSD (top panel) and entanglement entropy $S(t)$ (bottom panel) on log-log scale after numerical filtering (see main text) as a function of time for different disorder strengths ($W = 2 - 12$) and $\chi = 512$. *Left column.* $\gamma(t)$ and $D(t)$ computed from filtered MSD data, smoothed with a moving average of width $t = 4$ (two upper panels), and similarly $\delta(t)$ and dS/dt computed from filtered $S(t)$.

converged with respect to the system size ($L = 75$) except for the weakest disorder strength ($W = 2$) (see Section 7.7). At strong disorder, oscillatory features emerge, with a period of the order of the hopping rate. These oscillations are common in disordered systems, and typically correspond to oscillations between nearby localization centers. Such oscillations hinder the reliable extraction of dynamical exponents. In order to rectify this issue we filter-out the corresponding frequency in the Fourier domain (for raw data and a description of the procedure see Section 7.8). As can be seen from Fig. 7.2 the linear derivatives of MSD and $S(t)$ are monotonically decreasing with time, while their log-derivatives appear to converge to a constant value smaller than 1. This observation points towards a *sub-linear* dependence of MSD and $S(t)$, which is indicative of *subdiffusive* transport.

In Fig. 7.3 we examine the dependence of the dynamics on the range of the interaction by fixing the disorder strength ($W = 3.0$) and varying $2.0 \leq \alpha \leq 3.25$. The disorder is chosen,
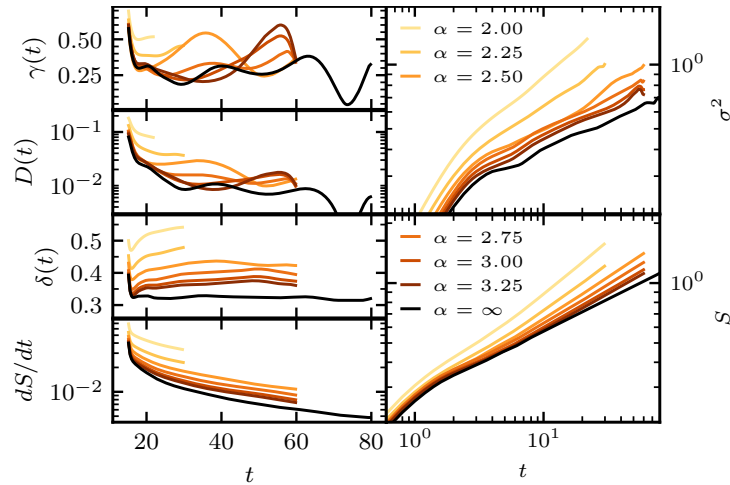
Figure 7.3: Similar to Fig. 6.8, but for $W = 3.0$ and $2.0 \leq \alpha \leq 3.25$. System sizes are $L = 75$ for $\alpha \leq 2.5$, $L = 51$ for $\alpha > 2.5$ and $L = 35$ for local interactions.

such that in the local limit, $\alpha \to \infty$ (black line in Fig. 7.3), the system is delocalized and subdiffusive [133]. Similarly to Fig. 7.2, the dynamical exponents γ and δ converge to a constant value smaller than 1 for all studied α's, which is monotonically decreasing with α. In Fig. 7.4 we plot the dynamical exponents as extracted from Figs. 7.2, 7.3 for different W's and α's. We use the relation between the exponents proposed in Refs. [226, 227] (see also Ref. [130]), $1/z = \gamma/2 = \delta/(1 + \delta)$. While the relation is not satisfied well, the overall dependence of the exponents appears similar, with both exponents monotonically decreasing with α and converging to the $\alpha \to \infty$ limit. The dynamical exponent $\delta(t)$ is reliable in the entire range of parameters, but the oscillations in the MSD result in large error bars in the extraction of $\gamma(t)$ for $\alpha > 2.5$.

Since the exact numerical study of long-range systems is rather limited in time, it is beneficial to find a phenomenological model which attempts to reproduce the relevant dynamical features, and at the same time suggests an effective mechanism. For disordered *local* systems the Griffiths picture serves this purpose [134, 217, 218]. We generalize the Griffiths picture
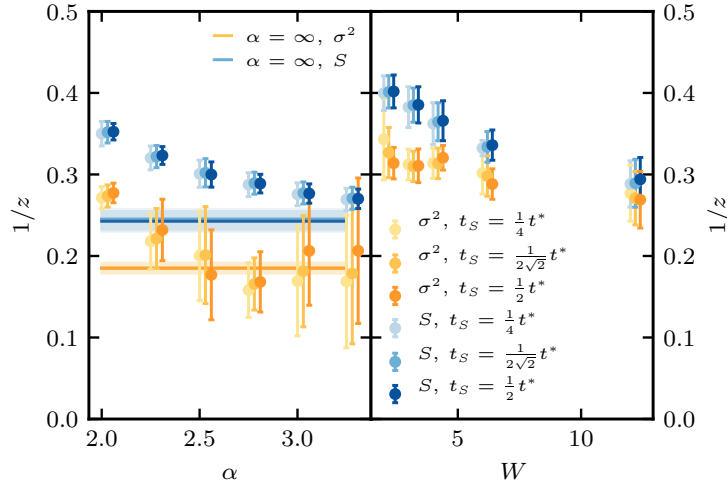
Figure 7.4: Dynamical exponent $1/z = \gamma/2$ for MSD (orange hues) and $S(t)$, $1/z = \delta/(1+\delta)$ (blue hues) as a function of α for $W = 3.0$ (left panel) and as a function of W for $\alpha = 1.75$ (right panel). The exponents and the error bars are obtained as average and standard deviation of the filtered data for the MSD and $S(t)$ over different windows $\left[t_S, 2^{-\frac{1}{4}}t^*\right]$ for left panel and $[t_S, t^*]$ for right panel, where t^* is the time up to which the averaged raw data for MSD and $S(t)$, respectively, is converged within 2% (see Section 7.6). The horizontal lines correspond to the limit $\alpha \to \infty$.

to long-range systems by introducing a finite probability for long jumps with a rate which decays as $x^{-2\alpha}$ in accord with the long-range part of the Hamiltonian [1]. This reduces to the following master equation,

$$\frac{\partial P_n}{\partial t} = \sum_i W_{in} P_i - \left(\sum_j W_{nj} \right) P_n \tag{7.6}$$

$$W_{ij} = \frac{e^{-h_{ij}}}{|i-j|^{2\alpha}} \qquad i \neq j$$

where h_{ij} is a symmetric matrix composed of independent random variables, which stand for the heights of the barriers. The precise shape of the distribution of the barrier heights is not important, as long as it is unbounded, guaranteeing the existence of very weak links. To be concrete, we take it to be $p(h) = h_0^{-1} \exp[-h/h_0]$. We note in passing, that while the form of the transition matrix is similar to the power-law random banded matrices used to study Anderson localization with power-law hopping [228], there are crucial differences: (a) we are applying it to a *classical* problem, (b) W_{ij} has many-elements close to zero, and must satisfy, $W_{ii} = -\sum_{i \neq j} W_{ij}$ to conserve probability. Since long-range hops effectively avoid weak links, such a model is expected to be diffusive, but it is important to see how it approaches diffusion as a function of time. To examine that, we numerically solve (7.6) for about 500 realizations of the transitions rate matrix, W_{ij}, with $h_0 = 8$ and a lattice size of $L = 1000$. At time $t = 0$ the walker is initiated at the origin, $P_n(t=0) = \delta_{n0}$. The probability to find a walker at site n for various times has a Gaussian form in the bulk, followed by a power-law tail, which can be better seen after the rescaling, $\sqrt{t} P_n(n/\sqrt{t})$ (see Fig. 7.5). Thus transport in this model is asymptotically diffusive. In Fig. 7.5 we show $D(t)$ and $\gamma(t)$ for this generalized Griffiths model as a function of time. We note that while

---

[1]The factor of 2 stems from the difference between amplitude and probability
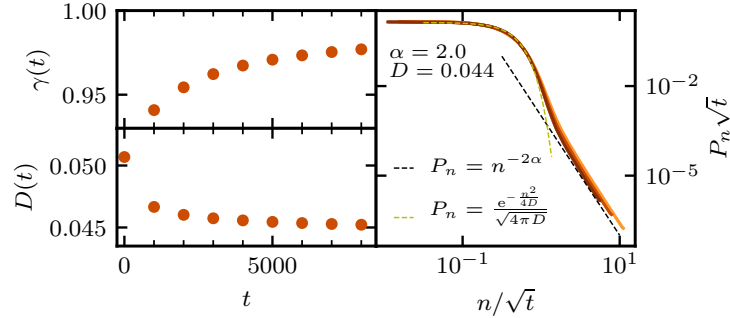
Figure 7.5: *Right panel.* A rescaled log-log plot of $P_n(t)$ for $\alpha = 2.0$, $h_0 = 8$ at various times t, computed from the solution of the generalized Griffiths model (7.6). *Left panels.* The corresponding dynamical exponent $\gamma(t)$ (top panel) and $D(t)$ (bottom panel).

$\gamma(t)$ converges to 1 and $D(t)$ converges to a constant, indicative of diffusive transport, the convergence is quite slow.

7.5   Discussion

Using a numerically exact method we performed an extensive study of transport of a disordered spin-chain with interactions between the spins decaying as $x^{-\alpha}$ with the distance. We have chosen α and W such that the system exhibits non-vanishing transport and therefore is in the ergodic phase. Because it is very hard to distinguish slow transport from localization using our method, we didn't attempt to locate the critical α or W or to demonstrate the absence thereof.

Over the full range of the studied parameters we observe a sublinear growth of the entanglement entropy and the MSD, which is consistent with subdiffusive spin-transport. Since long-range interactions introduce an effective channel to circumvent rare-blocking regions, our study puts in question the prevailing theoretical explanation of subdiffusive transport in disordered interacting systems, known as the Griffiths picture [218]. We generalized the

Griffiths picture to long-range systems and numerically solved the corresponding master equation (7.6), showing that within this picture, transport in long-range systems is asymptotically *diffusive*, though the convergence of the time-dependent diffusion coefficient to its asymptotic value is quite slow. The numerically exact results are therefore inconsistent with the rare-blocking regions mechanism, at least up to the studied times.

There could be at least two possible interpretations to our findings. First, it could be that diffusion is recovered for times which are inaccessible by numerically exact studies. While this scenario would make our results consistent with the Griffiths picture [218], one would have to understand the origin of the emerging time-scale at which a crossover to diffusion occurs. Second, if subdiffusion persists asymptotically, our findings add up to the mounting evidence against the importance of rare-blocking regions for subdiffusion, as was shown already in Refs. [137, 229] (cf. [230, 231], and see also the very recent [232]), suggesting that our understanding of the mechanism of anomalous transport in the vicinity of the MBL transition is far from being complete. It would be interesting to consider transport of other conserved quantities, such as the energy, which in principle can exhibit different dynamical behavior, and indeed was predicted to be diffusive in Ref. [210].

7.6 Convergence with respect to numerical parameters

Numerical exactness of the dynamics generated by TDVP-MPS is obtained by converging with respect to the bond-dimension, χ, as well as the time-step, dt. In Fig. 7.6 , we provide comparisons of the mean-square displacement (MSD) and the entanglement entropy $S(t)$ from calculations with bond-dimensions up to $\chi = 1024$. All results for the MSD and $S(t)$ reported in the main article are converged up to a deviation of 2 % between the two largest

Figure 7.6: Convergence of the MSD and $S(t)$ with respect to the bond dimension at $\alpha = 1.75$ for various disorder strengths W. *Upper panel*: MSD and $S(t)$ at reference bond dimensions $\chi = 1024$ ($W = 2$ and 3, solid) and $\chi = 512$ ($W = 4, 6$ and 12 solid) and half the reference bond dimension (dashed). *Lower panel*: Relative errors $\Delta\sigma^2$(left panel) and ΔS (right panel) between calculations at the reference and half the reference bond dimension. The system size for all panels is $L = 75$ and a time-step of $dt = 0.1$ was used.
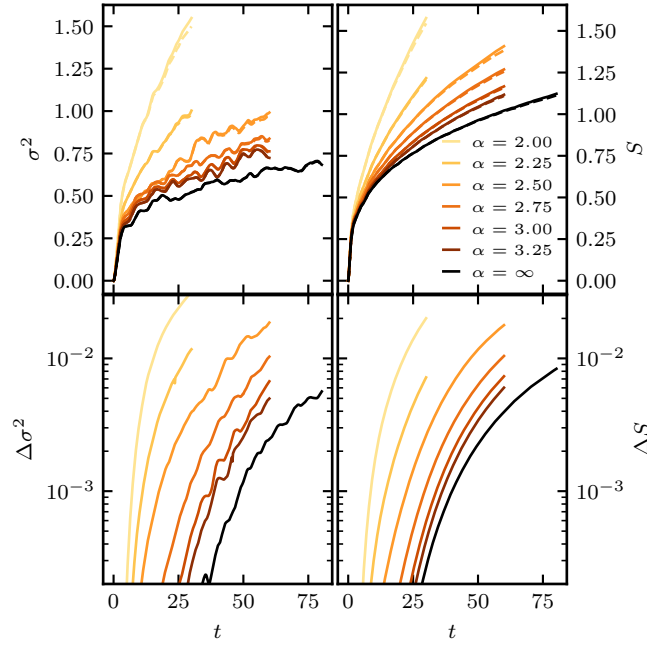
Figure 7.7: Convergence of the MSD and $S(t)$ with respect to bond dimension for various α and a disorder strength of $W = 3.0$. *Upper panel*: MSD and $S(t)$ at bond dimensions $\chi = 512$ (solid) and $\chi = 256$ (dashed). *Lower panel*: Relative deviation $\Delta\sigma^2$ (left panel) and ΔS (right panel) of calculations with $\chi = 256$ and $\chi = 512$.. The system sizes for all panels are $L = 75$ for $\alpha \leq 2.5$, $L = 51$ for $2.5 < \alpha \leq 3.25$ and $L = 35$ for $\alpha = \infty$. A time-step of $dt = 0.1$ was used.

Figure 7.8: Convergence of the MSD with respect to time-step. Relative error $\Delta\sigma^2$ compared to a reference calculation with time-step $dt = 0.005$ for $L = 51$, $\chi = 64$ at weak and strong disorder.

bond dimensions. In order to check for convergence with the time-step it is sufficient to use a smaller bond dimension, since time-step errors are usually more severe at smaller bond dimension. Fig. 7.8 shows the relative deviation of the MSD at several time-steps from a reference calculation at time-step $dt = 0.005$. The large relative error initially is caused by an approximately constant error in absolute terms and that becomes negligible in relative terms after times larger than a few units of the hopping. A time-step of $dt = 0.1$ is thus sufficient to obtain a converged MSD within the range of disorder strengths studied. Evaluating the spatial spin excitation profile in the tails at strong disorder becomes sensitive to numerical noise for small values of the correlation function, C_x, and is limited by a complex interplay of time-step errors and accumulation of numerical round-off errors. As shown in Fig. 7.9, the convergence of the tails of the spin excitation profile with respect to bond dimension is generally well controlled ($< 5\%$) up to times for which the MSD is converged as well.

Figure 7.9: Convergence of the spin excitation profiles with respect to bond dimension for $L = 51$ and $dt = 0.1$ at various disorder strengths and times. *Upper panels*: Relative error ΔC_x between calculations with $\chi = 512$ and $\chi = 256$. *Lower panels*: Tails of spin excitation profiles with $\chi = 512$ (solid lines) and $\chi = 256$ (black dotted lines).
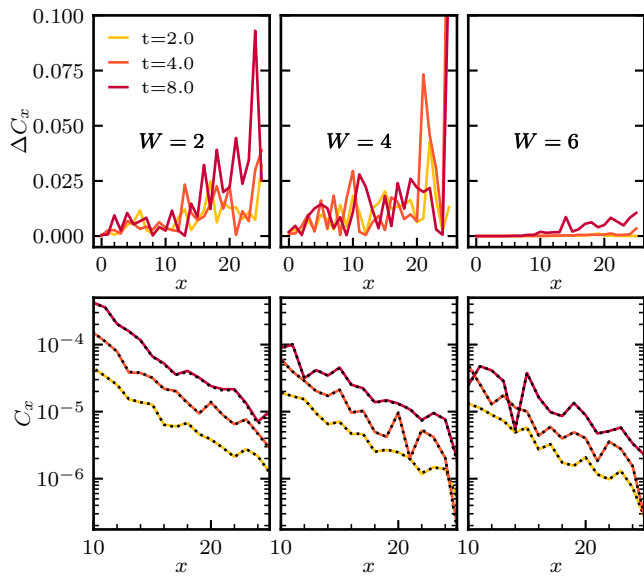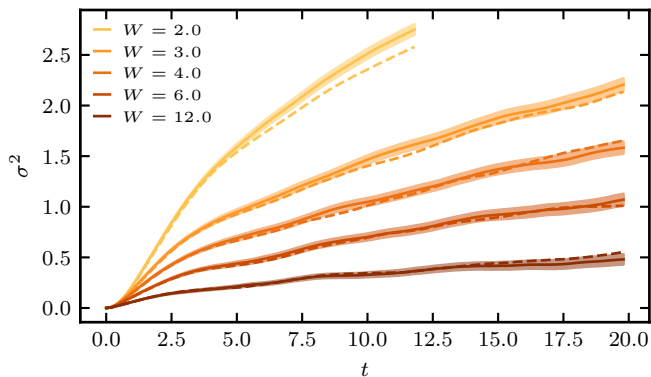
Figure 7.10: Comparison of the MSD for various disorder strengths at $\alpha = 1.75$ for system sizes $L = 75$ (solid lines) and $L = 51$ (dashed lines). The shaded area indicates the standard deviation for $L = 75$ obtained from bootstrap sampling.

7.7 Finite size effects

In Fig. 7.10 we provide evidence that the MSD is converged with respect to system size for $L = 75$ for the data presented in the main article at $\alpha = 1.75$ for all but the smallest disorder strengths $W = 2.0$.

7.8 Filtering out high-frequency oscillations

The presence of strong disorder leads to high frequency oscillations which average only slowly and are an obstacle in analyzing transport properties quantitatively. Hence, we smooth our data by removing the high frequency oscillations according to the following protocol. The linear time derivative of the data is Fourier transformed and a Gaussian broadening is applied in the Fourier domain before transforming back to the time domain, from which the filtered data is obtained by integration. We find that applying a weak broadening at low frequencies, and successively increasing the strength of the broadening at higher frequencies results in an efficient and unbiased removal of the high frequency oscillations. First a broadening of

width $w = 0.25$ is applied to the range of all nonzero frequencies, followed by a broadening of width $w = 0.75$ excluding the two lowest frequencies, and finally a broadening of width $w = 1.5$ applied to all but the 4 lowest frequencies. We note that the result depends weakly on the exact values of these parameters. This processing does not result in a systematic bias compared to the raw data, as shown in Fig. 7.11. The smoothing becomes inefficient towards the boundaries of the support of the data in the time-domain. When available, the raw data has been used past its convergence time as an input for the filtering to circumvent this problem. In the main text, we report only the filtered data and only up to the convergence time determined from Figs. 7.6 and 7.7. While this can in principle introduce a bias for the filtering at late times, we verified that the filtered data is consistent with the raw data for all converged times.
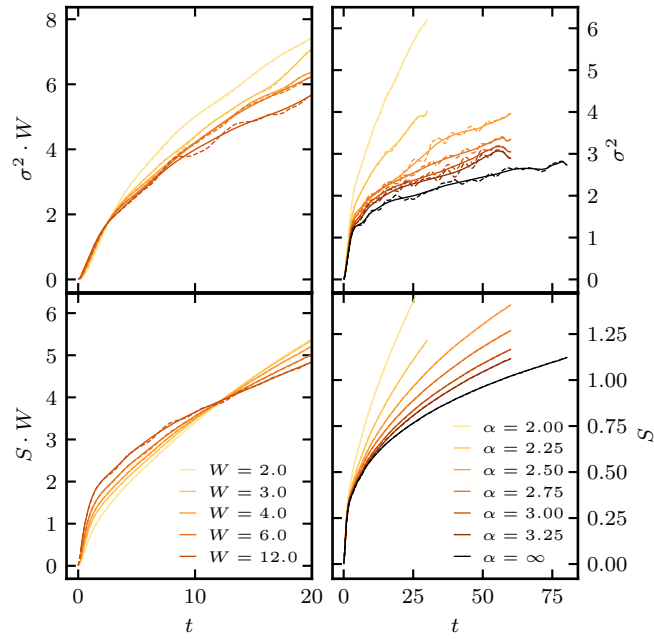
Figure 7.11: Comparison of filtered (solid lines) and unfiltered (dashed lines) MSD (upper panels) and entanglement entropy $S(t)$ (lower panels) for various disorder strengths at $\alpha = 1.75$ (left panels) and for various α with a disorder strength of $W = 3.0$ (right panels). For improved visibility, the data for $\alpha = 1.75$ (left panels) is rescaled with the disorder strength.

Bibliography

[1] Y.-C. Cheng and G. R. Fleming, Annu. Rev. Phys. Chem. **60**, 241–262 (2009).

[2] C. S. Ponseca, P. Chábera, J. Uhlig, P. Persson, and V. Sundström, Chem. Rev. **117**, 10940–11024 (2017).

[3] M. Thoss and F. Evers, J. Chem. Phys **148**, 030901 (2018).

[4] D. Basov, R. Averitt, and D Hsieh, Nat. Mater. **16**, 1077–1088 (2017).

[5] P. W. Anderson, Phys. Rev. **112**, 1900–1916 (1958).

[6] D. Basko, I. L. Aleiner, and B. L. Altshuler, Ann. Phys. (N. Y). **321**, 1126–1205 (2006).

[7] D. A. Abanin and Z. Papić, Ann. Phys. **529**, 1700169 (2017).

[8] I. Bloch, J. Dalibard, and S. Nascimbène, Nat. Phys. **8**, 267–276 (2012).

[9] E. Anderson, Z. Bai, C. Bischof, S. Blackford, J. Demmel, J. Dongarra, J. Du Croz, A. Greenbaum, S. Hammarling, A. McKenney, and D. Sorensen, *LAPACK users' guide*, Third (Society for Industrial and Applied Mathematics, Philadelphia, PA, 1999).

[10] R. Steinigeweg, F. Jin, H. De Raedt, K. Michielsen, and J. Gemmer, Phys. Rev. E **96**, 020105 (2017).

[11] M. B. Hastings, J. Stat. Mech. Theory Exp. **2007**, P08024–P08024 (2007).

[12] A. Anshu, I. Arad, and D. Gosset, *An area law for 2d frustration-free spin systems*, 2021, arXiv:2103.02492 [quant-ph].

[13] U. Schollwöck, Ann. Phys. (N. Y). **326**, 96–192 (2011).

[14] S. R. White, Phys. Rev. Lett. **69**, 2863–2866 (1992).

[15] F. Verstraete and J. I. Cirac, *Renormalization algorithms for quantum-many body systems in two and higher dimensions*, 2004, arXiv:cond-mat/0407066 [cond-mat.str-el].

[16] F. Verstraete, M. M. Wolf, D. Perez-Garcia, and J. I. Cirac, Phys. Rev. Lett. **96**, 220601 (2006).

[17] M. Lubasch, J. I. Cirac, and M.-C. Bañuls, New J. Phys. **16**, 033014 (2014).

[18] S.-J. Ran, E. Tirrito, C. Peng, X. Chen, L. Tagliacozzo, G. Su, and M. Lewenstein, *Tensor network contractions* (Springer International Publishing, 2020).

[19] P. Calabrese and J. Cardy, J. Stat. Mech. Theory Exp. **2005**, P04010 (2005).

[20] G. Vidal, Phys. Rev. Lett. **93**, 040502 (2004).

[21] J. Haegeman, J. I. Cirac, T. J. Osborne, I. Pižorn, H. Verschelde, and F. Verstraete, Phys. Rev. Lett. **107**, 070601 (2011).

[22] J. Haegeman, C. Lubich, I. Oseledets, B. Vandereycken, and F. Verstraete, Phys. Rev. B **94**, 165116 (2016).

[23] B. Kloss, D. R. Reichman, and Y. B. Lev, SciPost Phys. **9**, 70 (2020).

[24] G. D. Chiara, S. Montangero, P. Calabrese, and R. Fazio, J. Stat. Mech. Theory Exp. **2006**, P03001 (2006).

[25] V. Alba and P. Calabrese, Proc. Natl. Acad. Sci. U.S.A. **114**, 7947–7951 (2017).

[26] I. Bloch, J. Dalibard, and W. Zwerger, Rev. Mod. Phys. **80**, 885–964 (2008).

[27] B.-X. Zheng, C.-M. Chung, P. Corboz, G. Ehlers, M.-P. Qin, R. M. Noack, H. Shi, S. R. White, S. Zhang, and G. K.-L. Chan, Science **358**, 1155–1160 (2017).

[28] , L. Wang, and F. Verstraete, Phys. Rev. A **83**, 052321 (2011).

[29] A. Kshetrimayum, M. Goihl, and J. Eisert, Phys. Rev. B **102**, 235132 (2020).

[30] C. Hubig, A. Bohrdt, M. Knap, F. Grusdt, and J. I. Cirac, SciPost Phys. **8**, 21 (2020).

[31] M. P. Zaletel and F. Pollmann, Phys. Rev. Lett. **124**, 037201 (2020).

[32] G. M. Crosswhite, A. C. Doherty, and G. Vidal, Phys. Rev. B **78**, 035116 (2008).

[33] F. Fröwis, V. Nebendahl, and W. Dür, Phys. Rev. A **81**, 062337 (2010).

[34] E. Stoudenmire and S. R. White, Annu. Rev. Condens. Matter Phys. **3**, 111–128 (2012).

[35] M. P. Zaletel, R. S. K. Mong, C. Karrasch, J. E. Moore, and F. Pollmann, Phys. Rev. B **91**, 165112 (2015).

[36] S. Paeckel, T. Köhler, A. Swoboda, S. R. Manmana, U. Schollwöck, and C. Hubig, Ann. Phys. (N. Y.) **411**, 167998 (2019).

[37] E. V. H. Doggen, I. V. Gornyi, A. D. Mirlin, and D. G. Polyakov, Phys. Rev. Lett. **125**, 155701 (2020).

[38] G. Carleo and M. Troyer, Science **355**, 602–606 (2017).

[39] M. Schmitt and M. Heyl, Phys. Rev. Lett. **125**, 100503 (2020).

[40] I. López-Gutiérrez and C. B. Mendl, *Real time evolution with neural-network quantum states*, 2019, arXiv:1912.08831 [cond-mat.dis-nn].

[41] M Rizzi, S Montangero, P Silvi, V Giovannetti, and R. Fazio, New J. Phys. **12**, 075018 (2010).

[42] Z.-L. Tsai, P. Chen, and Y.-C. Lin, Eur. Phys. J. B **93**, 1–10 (2020).

[43] Y. Y. Shi, L. M. Duan, and G. Vidal, Phys. Rev. A. **74**, 1–4 (2006).

[44] L. Tagliacozzo, G. Evenbly, and G. Vidal, Phys. Rev. B. **80**, 1–17 (2009), arXiv:0903.5017.

[45] W. Li, J. von Delft, and T. Xiang, Phys. Rev. B **86**, 195137 (2012).

[46] V. Murg, F. Verstraete, O. Legeza, and R. M. Noack, Phys. Rev. B **82**, 205105 (2010).

[47] M. Gerster, P. Silvi, M. Rizzi, R. Fazio, T. Calarco, and S. Montangero, Phys. Rev. B. **90**, 1–10 (2014), arXiv:1406.2666.

[48] E. Macaluso, T. Comparin, M. Gerster, S. Montangero, M. Rizzi, and I. Carusotto, Phys. Rev. Research **2**, 013145 (2020).

[49] N. Nakatani and G. K. L. Chan, J. Chem. Phys **138**, 013145 (2013), arXiv:1302.2298.

[50] V. Murg, F. Verstraete, R. Schneider, P. R. Nagy, and Legeza, J. Chem. Theory Comput. **11**, 1027–1036 (2015).

[51] K. Gunst, F. Verstraete, S. Wouters, O. Legeza, and D. Van Neck, J. Chem. Theory Comput. **14**, 2026–2033 (2018).

[52] H. D. Meyer, U. Manthe, and L. S. Cederbaum, Chem. Phys. Lett. **165**, 73–78 (1990).

[53] M. H. Beck, A. Jäckle, G. A. Worth, and H.-D. Meyer, Physics reports **324**, 1–105 (2000).

[54] H. Wang and M. Thoss, The J. Chem. Phys **119**, 1289–1299 (2003).

[55] P. A. M. Dirac, Mathematical Proceedings of the Cambridge Philosophical Society **26**, 376–385 (1930).

[56] J. I. Frenkel, *Wave mechanics: Advanced general theory*, Vol. 2 (Clarendon Press, Oxford, 1934), 013145.

[57] T. Koffel, M Lewenstein, and L. Tagliacozzo, Phys. Rev. Lett. **109**, 267203 (2012).

[58] P. Hauke and L. Tagliacozzo, Phys. Rev. Lett. **111**, 207202 (2013).

[59] C. Lubich, I. V. Oseledets, and B. Vandereycken, SIAM Journal on Numerical Analysis **53**, 917–941 (2015), eprint: https://doi.org/10.1137/140976546.

[60] E. Leviatan, F. Pollmann, J. H. Bardarson, D. A. Huse, and E. Altman, *Quantum thermalization dynamics with matrix-product states*, 2017, arXiv:1702.08894 [cond-mat.stat-mech].

[61] B. Kloss, Y. Bar Lev, and D. Reichman, Phys. Rev. B **97**, 024307 (2018).

[62] C. Krumnow, L. Veis, O. Legeza, and J. Eisert, Phys. Rev. Lett. **117**, 210402 (2016).

[63] C. Krumnow, J. Eisert, and O. Legeza, *Towards overcoming the entanglement barrier when simulating long-time evolution*, 2019, arXiv:1904.11999 [cond-mat.stat-mech].

[64] C. D. White, M. Zaletel, R. S. K. Mong, and G. Refael, Phys. Rev. B **97**, 035127 (2018).

[65] J. Hauschild, E. Leviatan, J. H. Bardarson, E. Altman, M. P. Zaletel, and F. Pollmann, Phys. Rev. B **98**, 235163 (2018).

[66] J. Surace, M. Piani, and L. Tagliacozzo, Phys. Rev. B **99**, 235115 (2019).

[67] M. M. Rams and M. Zwolak, Phys. Rev. Lett. **124**, 137701 (2020).

[68] T. Rakovszky, C. W. von Keyserlingk, and F. Pollmann, *Dissipation-assisted operator evolution method for capturing hydrodynamic transport*, 2020, arXiv:2004.05177 [cond-mat.str-el].

[69] C. Lubich, Applied Mathematics Research eXpress **2015**, 311–328 (2014).

[70] A. J. Ferris, Phys. Rev. B **87**, 125139 (2013).

[71] F. A. Schröder, D. H. Turban, A. J. Musser, N. D. Hine, and A. W. Chin, Nat. Commun. **10**, 1062 (2019).

[72] D. Bauernfeind and M. Aichhorn, SciPost Phys. **8**, 24 (2020).

[73] G. Ceruti, C. Lubich, and H. Walach, SIAM Journal on Numerical Analysis **59**, 289–313 (2021), eprint: `https://doi.org/10.1137/20M1321838`.

[74] D. Nagaj, E. Farhi, J. Goldstone, P. Shor, and I. Sylvester, Phys. Rev. B **77**, 214431 (2008).

[75] A. Uschmajew and B. Vandereycken, Linear Algebra and its Applications **439**, 133–166 (2013).

[76] C. Lubich, T. Rohwedder, R. Schneider, and B. Vandereycken, SIAM Journal on Matrix Analysis and Applications **34**, 470–494 (2013).

[77] B. Kloss, I. Burghardt, and C. Lubich, J. Chem. Phys **146**, 174107 (2017).

[78] M. Yang and S. R. White, Phys. Rev. B **102**, 094315 (2020).

[79] C. M. Hinz, S Bauch, and M Bonitz, Journal of Physics: Conference Series **696**, 012009 (2016).

[80] U. Manthe, J. Chem. Phys **142**, 244109 (2015).

[81] H. Wang and M. Thoss, New J. Phys. **10**, 115005 (2008).

[82] E. Y. Wilner, H. Wang, G. Cohen, M. Thoss, and E. Rabani, Phys. Rev. B. **88**, 045137 (2013).

[83] R. Binder, D. Lauvergnat, and I. Burghardt, Phys. Rev. Lett. **120**, 227401 (2018).

117

[84] G. Vidal, Phys. Rev. Lett. **99**, 220405 (2007).

[85] M. Aguado and G. Vidal, Phys. Rev. Lett. **100**, 070404 (2008).

[86] B. Kloss, D. R. Reichman, and R. Tempelaar, Phys. Rev. Lett. **123**, 126601 (2019).

[87] F. C. Spano, Acc. Chem. Res. **43**, 429–439 (2010).

[88] J. M. Womick and A. M. Moran, J. Phys. Chem. B **115**, 1347–1356 (2011).

[89] F. D. Fuller, J. Pan, A. Gelzinis, V. Butkus, S. S. Senlik, D. E. Wilcox, C. F. Yocum, L. Valkunas, D. Abramavicius, and J. P. Ogilvie, Nat. Chem. **6**, 706– (2014).

[90] P. Nalbach, C. A. Mujica-Martinez, and M. Thorwart, Phys. Rev. E **91**, 022706 (2015).

[91] A. A. Bakulin, S. E. Morgan, T. B. Kehoe, M. W. B. Wilson, A. W. Chin, D. Zigmantas, D. Egorova, and A. Rao, Nat. Chem. **8**, 16– (2015).

[92] R. Tempelaar and D. R. Reichman, J. Chem. Phys. **146**, 174703 (2017).

[93] Y. Fujihashi, L. Chen, A. Ishizaki, J. Wang, and Y. Zhao, J. Chem. Phys. **146**, 044101 (2017).

[94] A. F. Morrison and J. M. Herbert, J. Phys. Chem. Lett. **8**, 1442–1448 (2017).

[95] R. Tempelaar and D. R. Reichman, J. Chem. Phys. **148**, 244701 (2018).

[96] A. Migdal, Sov. Phys. JETP **7**, 996–1001 (1958).

[97] T Holstein, Ann. Phys. **8**, 325 –342 (1959).

[98] T. Holstein, Ann. Phys. **8**, 343 –389 (1959).

[99] I. G. Lang and Y. A. Firsov, Zh. Eksp. Teor. Fiz. **43**, 1843 (1962).

[100] D. Feinberg, S. Ciuchi, and F. de Pasquale, Int. J. Mod. Phys. B **4**, 1317–1367 (1990).

[101] Y. Tanimura and R. Kubo, J. Phys. Soc. Jpn. **58**, 101–114 (1989).

[102] N. Makri and D. E. Makarov, J. Chem. Phys. **102**, 4600–4610 (1995).

[103] L. Diósi and W. T. Strunz, Phys. Lett. A **235**, 569 –573 (1997).

[104] L. Chen, Y. Zhao, and Y. Tanimura, J. Phys. Chem. Lett. **6**, 3110–3115 (2015).

[105] M. R. Philpott, J. Chem. Phys. **55**, 2039–2054 (1971).

[106] M. Hoffmann and Z. G. Soos, Phys. Rev. B **66**, 024305 (2002).

[107] M. Fannes, B. Nachtergaele, and R. F. Werner, Comm. Math. Phys. **144**, 443–490 (1992).

[108] E. Jeckelmann and S. R. White, Phys. Rev. B **57**, 6376–6385 (1998).

[109] G. A. Worth, H. Meyer, and L. S. Cederbaum, J. Chem. Phys **105**, 4412–4426 (1996).

[110] J. Prior, A. W. Chin, S. F. Huelga, and M. B. Plenio, Phys. Rev. Lett. **105**, 050404 (2010).

[111] C. Brockt, F. Dorfner, L. Vidmar, F. Heidrich-Meisner, and E. Jeckelmann, Phys. Rev. B **92**, 241106 (2015).

[112] J. Ren, Z. Shuai, and G. Kin-Lic Chan, J. Chem. Theory Comput. **14**, 5027–5039 (2018).

[113] Y. Kurashige, J. Chem. Phys **149**, 194114 (2018).

[114] J. H. Bardarson, F. Pollmann, and J. E. Moore, Phys. Rev. Lett. **109**, 017202 (2012).

[115] D. J. Luitz, Phys. Rev. B **93**, 134201 (2016).

[116] J. Fang and H. Guo, J. Chem. Phys. **101**, 5831–5840 (1994).

[117] N. J. Hestand, R. Tempelaar, J. Knoester, T. L. C. Jansen, and F. C. Spano, Phys. Rev. B **91**, 195315 (2015).

[118] F. Dorfner, L. Vidmar, C. Brockt, E. Jeckelmann, and F. Heidrich-Meisner, Phys. Rev. B **91**, 104302 (2015).

[119] T. G. Kolda and B. W. Bader, SIAM Review **51**, 455–500 (2008).

[120] J. Hauschild and F. Pollmann, SciPost Phys. Lect. Notes **2**, 5 (2018).

[121] J. Haegeman, T. J. Osborne, and F. Verstraete, Phys. Rev. B **88**, 075133 (2013).

[122] B. Bertini, M. Collura, J. De Nardis, and M. Fagotti, Phys. Rev. Lett. **117**, 207201 (2016).

[123] P. Jordan and E. Wigner, Zeitschrift für Phys. **47**, 631–651 (1928).

[124] P. W. Anderson, Phys. Rev. **109**, 1492–1505 (1958).

[125] T. C. Berkelbach and D. R. Reichman, Phys. Rev. B **81**, 224429 (2010).

[126] D. J. Luitz, N. Laflorencie, and F. Alet, Phys. Rev. B **91**, 081103 (2015).

[127] R Steinigeweg, H Wichterich, and J Gemmer, EPL (Europhysics Lett. **88**, 10004 (2009).

[128] Y. Yan, F. Jiang, and H. Zhao, Eur. Phys. J. B **88**, 11 (2015).

[129] R. Steinigeweg, F. Jin, D. Schmidtke, H. De Raedt, K. Michielsen, and J. Gemmer, Phys. Rev. B **95**, 035155 (2017).

[130] D. J. Luitz and Y. Bar Lev, Ann. Phys. **529**, 1600350 (2016).

[131] R. Steinigeweg, F. Heidrich-Meisner, J. Gemmer, K. Michielsen, and H. De Raedt, Phys. Rev. B **90**, 094417 (2014).

[132] C. Karrasch, D. M. Kennes, and F. Heidrich-Meisner, Phys. Rev. B **91**, 115130 (2015).

[133] Y. Bar Lev, G. Cohen, and D. R. Reichman, Phys. Rev. Lett. **114**, 100601 (2015).

[134] K. Agarwal, S. Gopalakrishnan, M. Knap, M. Müller, and E. Demler, Phys. Rev. Lett. **114**, 160401 (2015).

[135] D. J. Luitz, N. Laflorencie, and F. Alet, Phys. Rev. B **93**, 060201 (2016).

[136] Y. Bar Lev and D. R. Reichman, Phys. Rev. B **89**, 220201 (2014).

[137] Y. Bar Lev and D. R. Reichman, EPL (Europhysics Lett. **113**, 46001 (2016).

[138] S. Fishman, Y. Krivolapov, and A. Soffer, Nonlinearity **25**, R53–R72 (2012).

[139] B. Kloss and Y. Bar Lev, Phys. Rev. A **99**, 032114 (2019).

[140] G. A. Alvarez, D. Suter, and R. Kaiser, Science (80-.). **349**, 846–848 (2015).

[141] L. S Levitov, Europhys. Lett. **9**, 83–86 (1989).

[142] L. S. Levitov, Phys. Rev. Lett. **64**, 547–550 (1990).

[143] I. L. Aleiner, B. L. Altshuler, and K. B. Efetov, Phys. Rev. Lett. **107**, 076401 (2011).

[144] V. Agranovich, *Excitations in Organic Solids*, Vol. 2 (Oxford University Press, 2008), 013145.

[145] L. Childress, M. V. Gurudev Dutt, J. M. Taylor, A. S. Zibrov, F. Jelezko, J. Wrachtrup, P. R. Hemmer, and M. D. Lukin, Science (80-.). **314**, 281–285 (2006).

[146] G. Balasubramanian, P. Neumann, D. Twitchen, M. Markham, R. Kolesov, N. Mizuochi, J. Isoya, J. Achard, J. Beck, J. Tissler, V. Jacques, P. R. Hemmer, F. Jelezko, and J. Wrachtrup, Nat. Mater. **8**, 383–387 (2009).

[147] P. Neumann, R. Kolesov, B. Naydenov, J. Beck, F. Rempp, M. Steiner, V. Jacques, G. Balasubramanian, M. L. Markham, D. J. Twitchen, S. Pezzagna, J. Meijer, J. Twamley, F. Jelezko, and J. Wrachtrup, Nat. Phys. **6**, 249–253 (2010).

[148] J. R. Weber, W. F. Koehl, J. B. Varley, A. Janotti, B. B. Buckley, C. G. Van de Walle, and D. D. Awschalom, Proc. Natl. Acad. Sci. **107**, 8513–8518 (2010).

[149] F. Dolde, I. Jakobi, B. Naydenov, N. Zhao, S. Pezzagna, C. Trautmann, J. Meijer, P. Neumann, F. Jelezko, and J. Wrachtrup, Nat. Phys. **9**, 139–143 (2013).

[150] A. S. Alexandrov and N. F. Mott, *Polarons and Bipolarons*, Vol. 2 (World Scientific, 1996), 013145.

[151] M. Saffman, T. G. Walker, and K. Mølmer, Rev. Mod. Phys. **82**, 2313–2363 (2010).

[152] K. Aikawa, A. Frisch, M. Mark, S. Baier, A. Rietzler, R. Grimm, and F. Ferlaino, Phys. Rev. Lett. **108**, 210401 (2012).

[153] M. Lu, N. Q. Burdick, and B. L. Lev, Phys. Rev. Lett. **108**, 215301 (2012).

[154] B. Yan, S. A. Moses, B. Gadway, J. P. Covey, K. R. A. Hazzard, A. M. Rey, D. S. Jin, and J. Ye, Nature **501**, 521–525 (2013).

[155] G. Gunter, H. Schempp, M. Robert-de Saint-Vincent, V. Gavryusev, S. Helmrich, C. S. Hofmann, S. Whitlock, and M. Weidemuller, Science (80-.). **342**, 954–956 (2013).

[156] A. de Paz, A. Sharma, A. Chotia, E. Maréchal, J. H. Huckans, P. Pedri, L. Santos, O. Gorceix, L. Vernac, and B. Laburthe-Tolra, Phys. Rev. Lett. **111**, 185305 (2013).

[157] P. Schauß, M. Cheneau, M. Endres, T. Fukuhara, S. Hild, A. Omran, T. Pohl, C. Gross, S. Kuhr, and I. Bloch, Nature **491**, 87–91 (2012).

[158] J. W. Britton, B. C. Sawyer, A. C. Keith, C.-C. J. Wang, J. K. Freericks, H. Uys, M. J. Biercuk, and J. J. Bollinger, Nature **484**, 489–492 (2012).

[159] R. Islam, C. Senko, W. C. Campbell, S. Korenblit, J. Smith, A. Lee, E. E. Edwards, C.-C. J. Wang, J. K. Freericks, and C. Monroe, Science (80-.). **340**, 583–587 (2013).

[160] P. Richerme, Z.-X. Gong, A. Lee, C. Senko, J. Smith, M. Foss-Feig, S. Michalakis, A. V. Gorshkov, and C. Monroe, Nature **511**, 198–201 (2014).

[161] P. Jurcevic, B. P. Lanyon, P. Hauke, C. Hempel, P. Zoller, R. Blatt, and C. F. Roos, Nature **511**, 202–205 (2014).

[162] E. H. Lieb and D. W. Robinson, Commun. Math. Phys. **28**, 251–257 (1972).

[163] M. B. Hastings and T. Koma, Commun. Math. Phys. **265**, 781–804 (2006).

[164] M. Foss-Feig, Z.-X. Gong, C. W. Clark, and A. V. Gorshkov, Phys. Rev. Lett. **114**, 157201 (2015).

[165] D.-M. Storch, M. van den Worm, and M. Kastner, New J. Phys. **17**, 063021 (2015).

[166] J. Eisert, M. van den Worm, S. R. Manmana, and M. Kastner, Phys. Rev. Lett. **111**, 260401 (2013).

[167] Z.-X. Gong, M. Foss-Feig, S. Michalakis, and A. V. Gorshkov, Phys. Rev. Lett. **113**, 030602 (2014).

[168] L. Cevolani, G. Carleo, and L. Sanchez-Palencia, Phys. Rev. A **92**, 041603 (2015).

[169] A. S. Buyskikh, M. Fagotti, J. Schachenmayer, F. Essler, and A. J. Daley, Phys. Rev. A **93**, 053620 (2016).

[170] L. Cevolani, G. Carleo, and L. Sanchez-Palencia, New J. Phys. **18**, 093002 (2016).

[171] M. Van Regemortel, D. Sels, and M. Wouters, Phys. Rev. A **93**, 032311 (2016).

[172] L. Cevolani, J. Despres, G. Carleo, L. Tagliacozzo, and L. Sanchez-Palencia, Phys. Rev. B **98**, 024302 (2018).

[173] D. J. Luitz and Y. Bar Lev, Phys. Rev. A **99**, 010105 (2019).

[174] M. F. Maghrebi, Z.-X. Gong, M. Foss-Feig, and A. V. Gorshkov, Phys. Rev. B **93**, 125128 (2016).

[175] L. Lepori, A. Trombettoni, and D. Vodola, J. Stat. Mech. Theory Exp. **2017**, 033102 (2017).

[176] R. Metzler and J. Klafter, Phys. Rep. **339**, 1–77 (2000).

[177] F. Verstraete, J. J. García-Ripoll, and J. I. Cirac, Phys. Rev. Lett. **93**, 207204 (2004).

[178] S. R. White and A. E. Feiguin, Phys. Rev. Lett. **93**, 076401 (2004).

[179] A. J. Daley, C Kollath, U Schollwöck, and G Vidal, J. Stat. Mech. Theory Exp. **2004**, P04005 (2004).

[180] M. Žnidarič, Phys. Rev. Lett. **110**, 070602 (2013).

[181] M. Žnidarič, Phys. Rev. B **88**, 205135 (2013).

[182] P. Lévy, Bull. la Société Mathématique Fr. **67**, 1–41 (1939).

[183] D. M. Kennes and C. Karrasch, Comput. Phys. Commun. **200**, 37–43 (2016).

[184] D. Vodola, L. Lepori, E. Ercolessi, A. V. Gorshkov, and G. Pupillo, Phys. Rev. Lett. **113**, 156402 (2014).

[185] D. Vodola, L. Lepori, E. Ercolessi, and G. Pupillo, New J. Phys. **18**, 015001 (2015).

[186] R. Bachelard and M. Kastner, Phys. Rev. Lett. **110**, 170603 (2013).

[187] M. Kastner, Phys. Rev. Lett. **106**, 130601 (2011).

[188] M. van den Worm, B. C. Sawyer, J. J. Bollinger, and M. Kastner, New J. Phys. **15**, 083007 (2013).

[189] M. Kastner, J. Stat. Mech. Theory Exp. **2017**, 014003 (2017).

[190] B. Kloss and Y. Bar Lev, Phys. Rev. B **102**, 060201 (2020).

[191] I. V. Gornyi, A. Mirlin, and D. Polyakov, Phys. Rev. Lett. **95**, 206603 (2005).

[192] M. Schreiber, S. S. Hodgman, P. Bordia, H. P. Luschen, M. H. Fischer, R. Vosk, E. Altman, U. Schneider, and I. Bloch, Science (80-.). **349**, 842–845 (2015).

[193] P. Bordia, H. P. Lüschen, S. S. Hodgman, M. Schreiber, I. Bloch, and U. Schneider, Phys. Rev. Lett. **116**, 140401 (2016).

[194] J. Smith, A. Lee, P. Richerme, B. Neyenhuis, P. W. Hess, P. Hauke, M. Heyl, D. A. Huse, and C. Monroe, Nat. Phys. **12**, 907–911 (2016).

[195] S. Inglis and L. Pollet, Phys. Rev. Lett. **117**, 120402 (2016).

[196] J.-Y. Choi, S. Hild, J. Zeiher, P. Schauss, A. Rubio-Abadal, T. Yefsah, V. Khemani, D. A. Huse, I. Bloch, and C. Gross, Science (80-.). **352**, 1547–1552 (2016).

[197] P. Bordia, H. Lüschen, S. Scherg, S. Gopalakrishnan, M. Knap, U. Schneider, and I. Bloch, Phys. Rev. X **7**, 041047 (2017).

[198] D. M. Kennes, "Many-Body Localization in Two Dimensions from Projected Entangled-Pair States", 2018, arXiv:1811.04126.

[199] A. Geißler and G. Pupillo, Phys. Rev. Research **2**, 042037 (2020).

[200] A. L. Burin, *Energy delocalization in strongly disordered systems induced by the long-range many-body interaction*, Nov. 2006, arXiv:cond-mat/0611387 [cond-mat.dis-nn].

[201] N. Y. Yao, C. R. Laumann, S. Gopalakrishnan, M. Knap, M. Müller, E. A. Demler, and M. D. Lukin, Phys. Rev. Lett. **113**, 243002 (2014).

[202] A. L. Burin, Phys. Rev. B **91**, 094202 (2015).

[203] S. Nag and A. Garg, Phys. Rev. B **99**, 224203 (2019).

[204] S. Roy and D. E. Logan, SciPost Phys. **7**, 042 (2019).

[205] W. De Roeck and F. Huveneers, Phys. Rev. B **95**, 155129 (2017).

[206] K. S. Tikhonov and A. D. Mirlin, Phys. Rev. B **97**, 214205 (2018).

[207] S. Gopalakrishnan and D. A. Huse, Phys. Rev. B **99**, 134305 (2019).

[208] A. Safavi-Naini, M. L. Wall, O. L. Acevedo, A. M. Rey, and R. M. Nandkishore, Phys. Rev. A **99**, 033610 (2019).

[209] S. J. Thomson and M. Schiró, Phys. Rev. Research **2**, 043368 (2020).

[210] D. B. Gutman, I. V. Protopopov, A. L. Burin, I. V. Gornyi, R. A. Santos, and A. D. Mirlin, Phys. Rev. B **93**, 245427 (2016).

[211] J. Choi, H. Zhou, S. Choi, R. Landig, W. W. Ho, J. Isoya, F. Jelezko, S. Onoda, H. Sumiya, D. A. Abanin, and M. D. Lukin, Phys. Rev. Lett. **122**, 043603 (2019).

[212] M. Žnidarič, A. Scardicchio, and V. K. Varma, Phys. Rev. Lett. **117**, 040601 (2016).

[213] D. J. Luitz and Y. Bar Lev, Phys. Rev. B **96**, 020406 (2017).

[214] T. L. M. Lezama, S. Bera, and J. H. Bardarson, Phys. Rev. B **99**, 161106 (2019).

[215] T. L. M. Lezama and D. J. Luitz, Phys. Rev. Research **1**, 033067 (2019).

[216] M. Serbyn and J. E. Moore, Phys. Rev. B **93**, 041424 (2016).

[217] S. Gopalakrishnan, M. Müller, V. Khemani, M. Knap, E. A. Demler, and D. A. Huse, Phys. Rev. B **92**, 104202 (2015).

[218] S. Gopalakrishnan, K. Agarwal, E. A. Demler, D. A. Huse, and M. Knap, Phys. Rev. B **93**, 134206 (2016).

[219] K. Agarwal, E. Altman, E. Demler, S. Gopalakrishnan, D. A. Huse, and M. Knap, Ann. Phys. **529**, 1600326 (2017).

[220] W. De Roeck, F. Huveneers, and S. Olla, J. Stat. Phys. **180**, 678–698 (2020).

[221] A. Wietek and A. M. Läuchli, Phys. Rev. E **98**, 033309 (2018).

[222] H. Kim and D. A. Huse, Phys. Rev. Lett. **111**, 127205 (2013).

[223] E. V. H. Doggen, F. Schindler, K. S. Tikhonov, A. D. Mirlin, T. Neupert, D. G. Polyakov, and I. V. Gornyi, Phys. Rev. B **98**, 174202 (2018).

[224] E. V. H. Doggen and A. D. Mirlin, Phys. Rev. B **100**, 104203 (2019).

[225] A. Schuckert, I. Lovas, and M. Knap, Phys. Rev. B **101**, 020416 (2020).

[226] R. Vosk, D. A. Huse, and E. Altman, Phys. Rev. X **5**, 031032 (2015).

[227] A. C. Potter, R. Vasseur, and S. A. Parameswaran, Phys. Rev. X **5**, 031033 (2015).

[228] A. D. Mirlin, Y. V. Fyodorov, F.-M. Dittes, J. Quezada, and T. H. Seligman, Phys. Rev. E **54**, 3221–3230 (1996).

[229] Y. Bar Lev, D. M. Kennes, C. Klöckner, D. R. Reichman, and C. Karrasch, EPL (Europhysics Lett. **119**, 37003 (2017).

[230] M. Žnidarič and M. Ljubotina, Proc. Natl. Acad. Sci. **115**, 4595–4600 (2018).

[231] V. K. Varma, Phys. Rev. B **100**, 085105 (2019).

[232] M Schulz, S. R. Taylor, A Scardicchio, and M Žnidarič, J. Stat. Mech. Theory Exp. **2020**, 023107 (2020).